Programmable Sphere – Tubule Frameworks Through Supramolecular and Supracolloidal Assembly Pathways

Ph.D. Course in Mathematical Models for Engineering, Electromagnetics and Nanosciences

XXXI Cycle

Academic year 2017-2018

SAPIENZA
UNIVERSITÀ DI ROMA

Candidate
Jacopo Cautela

Supervisor
Prof. Luciano Galantini

Abstract

The dissertation focuses on the study of a series of new supracolloidal frameworks which can be specifically programmed by the use of tailored supramolecular bile salt derivatives (BSDs) anisotropic structures in combination with isotropic polymeric particles, without resorting to auxiliary functionalization of none the two species. With their high tunability and high repetibility these programmable frameworks could be seen as an innovative pathway for mere nanomaterial preparation and for a deeper understanding of supracolloidal interaction mechanisms among different colloidal units. Three important features can be remarked:

1. The innovative use of anisotropic supramolecular building blocks working as versatile tools for supracolloidal assemblies preparation: the introduction of these mixed systems, based on elementary units composed from isotropic and anisotropic particles, allows to bypass the state of the art constrain given, among the other things, by the need to induce the anisotropy of interaction with satellite chemical functionalizations on the particle surface, particularly influencing the range of geometries accessible and the preparation complexity.
2. The possibility to program the specific framework desired, choosing among a wide range of BSDs with an achieved and solid know-how of their self-assembly behavior and structural characteristics.
3. The possibility to have as outcome intriguing systems in a wide range of configurations possible: from core-corona assemblies to chirally (or non-chirally) decorated supramolecular tubules, from highly ordered frameworks with lattice properties to well-defined crystalline domains in a gel matrix.

Thesis Overlook

The first chapter is intended to start with a very general introduction (Section 1.1) while the following sections increase stepwise the focus on the central theme of the work, reporting the state of the art in the field of supracolloidal assemblies (Section 1.2) and highlighting the most important aspects and implications of the whole study (Section 1.3). After the introduction, the main body of the work is structured in 4 Chapters. In Chapter 2 will be reported the preparation of supracolloidal frameworks based on the use of polymeric fluorescently labeled homogeneous or core-shell microgels and catanionic mixtures of the bile salt derivative NatButPhC. In Chapter 3 will be reported all the details about supracolloidal frameworks based on the use of the same microgel particles with supramolecular tubules of the bile salt derivative HNaphC. The last section of Chapter 3 is dedicated to fluorescent supracolloidal framework: a completely fluorescent variation of the above mentioned system, thanks to the use of a labeled derivative of cholic acid (NBD-ChA). Chapter 4 presents instead how NatButPhC in different supramolecular aggregation conditions, when mixed with polymeric microgels, can lead to the formation of colloidal crystals dispersed in a gel matrix. In the last chapter, Chapter 5, will be briefly presented some theoretical models together with calculations to give some information on interaction mechanisms between the colloids used. The "Atomium" building in Brussels, designed by the Architect André Waterkeyn was a source of inspiration for the whole project perfectly fitting with the idea of an interconnected perfect shape, concentrated in an elementary cell, arising from the connection of identical spheres and tubules.

Figure 1.1. Atomium building in Brussels, Belgium.

Table of Contents

List Of Abbreviations

BSs	Bile Salts
BSDs	Bile Salt Derivatives
BAs	Bile Acids
CA	Cholic acid
PhCs	Photonic Crystals
PBG	Photonic Band Gap
CSLM	Confocal Laser Scanning Microscopy
PSF	Point Spread Function
NA	Numerical Aperture
TEM	Transmission Electron Microscopy
TCSPC	Time Correlated Single Photon Counting
AuNPs	Gold nanoparticles
DLS	Dynamic Light Scattering
TCF	Time Correlation Function
$\vec{q}$	Scattering vector
D_0	Diffusion coefficient at infinite dilution
D_S	Self-diffusion coefficient
ACD	Anionic Cholate Derivative (NatButPhC)
CCD	Cationic Cholate Derivative
X_{ACD}	Anionic Cholate Derivative molar ratio
SAXS	Small Angle X-ray Scattering
μ	Electrophoretic mobility
TRITC	Tetramethylrhodamine
FITC	Fluoresceine isothyocyanate
PNIPAM	poly(N-isopropylacylamide)
PNIPMAM	poly(N-isopropylmethacrylamide)
PS	polystyrene
M-	Homogeneous anionic microgels
M+	Homogeneous cationic microgels
CSM+	Core-shell cationic microgels
CSM-	Core-shell anionic microgels
NBD	4-chloro-7-nitro-1,2,3-benzoxadiazole
NBD-ChA	NBD-derivative of CA
HNaphC	naphtoyl-amino- derivative of CA
NatButPhC	tertbutylbenzoyl-amino- derivative of CA
$c_{\mu gel}$	Microgel concentration
c_{tub}	Tubule concentration
ε	Molar extinction coefficient
$[\theta]$	Molar elipticity
k_B	Boltzmann constant

T	Temperature
d_{ctc}	Center-to-center distance
SAFIN	Self-assembled fibrillar network
FCC	Face centered cubic
HCP	Hexagonal close packing
R_H	Hydrodynamic radius
κ^{-1}	Debye length
l_B	Bjerrum length
φ	Volume fraction

1 Chapter 1: Introduction

1.1 Hierarchical Self-Organizing Frameworks: how Nature builds up itself

Since time witnessed the big bang as unmatched igniting spark of creation and bearer of demiurgic cataclysms, self-organization of matter started from the very first moments of its history. Despite the infinite ways through which Nature can shape itself, from solar systems to unicellular living beings, a deep glance at its forms can reveal how the arrangement of small subunits in bigger frameworks constitutes one of Nature's most intimate and primordial characteristics. With apparently no regards to the specific kind of force put on the line, subunits are spontaneously pushed to gather in harmony, and their existence becomes at the same time independent but coordinated, individual but nevertheless functional to the mechanism of the whole system, respecting an unprecise but perfect self-organized hierarchy. This subtle and imperishable process of aggregation and completion was generally called σύνθεσις, "composition" (from "*suntìthemi*", "I put things together") from Democritus disciples, when, around 460 B.C. – 370 B.C., the greek philosopher (50 years before Plato and Aristoteles) took the mankind by hand and showed to it the concept of ατομος ("*atomos*", "that cannot be cut") as an indivisible entity, able to assemble spontaneously and counteract the dark void of the non-existence. This, more than 2000 years ago, enlightened the path towards a new way to conceive Nature and look at its mysteries, building the foundations of modern science. Besides, releasing time and space constraints and looking from a wide perspective at Nature utterances, including social and stochastic events or even going deeply in the intricate tangles of physical and chemical phenomena, it can be overwhelmingly easy to encounter examples of hierarchical self-organizations. For instance, among the rare unimaginably big cosmic events the self-assembly process bringing to galaxies formation represents one of the most fascinating subjects. Gravity, discovered by man only few centuries ago, acts ceaselessly like a craftsman without rest to assemble particles to dust, dust to planets, planets with stars and clusters of solar systems around massive black holes: a hierarchy where mass and its laws dictate priorities. An ordered and rigid hierarchy is what can be suddenly guessed in all archetypical social structures. Among them, the one belonging to the bees is one of the most ancient and studied examples of social framework. Different social layers separate the few male drones (generally a hundred times fewer than females) from the queen bee, the reproductive center of the hive and consequently the power fulcrum. The female workers, thousands, when carrying out their duties from feeding

to food retrieving, from nursing to defending the hive, self-assembling in swarms assuming aggressive behavior, resemble a single perfectly coordinated entity. Moving the focus on the colloidal scale, natural frameworks have been widely reported and studied in the past several years. *Cyanophrys remus* [1] is a butterfly native of south America which wings are covered with a crystalline framework of randomly oriented opal-type photonic crystals (PhCs) of 5-10 μm in size and characterized by both long-range and short-range three dimensional orders, respectively on the dorsal and ventral side of the wings. Such a complex system, reported to be a PhC-based reflector, is useful to these animals since light scarceness into forest vegetation forced this species to develop a specific sexual communication channel. However, something which is even more complex and indeed much more ubiquitous than the crystalline structure of a butterfly wing is maybe the most fascinating singular unit known, and the only one able to hold life: the cell. First complete expression of life on Earth, the cell is the perfect example of how different self-defined units are hierarchically organized. The *cytoskeleton,* fully discovered in 1976 [2], may be considered as the main scaffold of the cell, sustaining its structure through the *cytoplasm* where different *organelles* can perpetrate their functions. It not only interacts with *cytoplasm* and organelles but also with cellular membrane and extracellular molecules, involving all the dynamic changes in the cell infrastructure. For instance, the microfilaments, one of cytoskeleton fibrillar structures, are the outcome of a co-assembly process of basically three proteins: *the actin*, which its repetition forms the helicoid central skeleton of the filament *Tropomyosin*, another fibrillar protein generating a secondary helicoid fiber and, finally, *troponin*. Furthermore, inside the cellular nucleus, DNA strands, having each one a precise primary and secondary structures, primitive origin of all the unique and invaluable information related to life, hierarchically self-assemble and elegantly fold from single strands to chromosomes. The process, helped by auxiliary proteins like histones H2B, H2A, H3 and H4 allows the strands to gradually compact in nucleosomes like beads on a string [3], forming chromatin. The extended strings of chromatin, driven by hydrophobic effect and hydrogen bonding, and constrained by electrostatic repulsions are able to univocally fold in more compact structures until the metaphase chromosomal structure is achieved. Looking at all these intriguing aspects of Nature, is absolutely self-evident how the more the technology development pushes further the borders of mankind evolution, so that our sight is projected decades and centuries to the future, the more science demonstrates how Nature can be inspirational for this process and fundamental for this development to happen. One day, hopefully, man will not only inspire his technology to Nature but he will learn from it forming, as the basic units hierarchically organized in its temporary and material structure, a whole

harmonic hybrid intelligent machine, like a little bright spot in the dark void Universe, the same that more than 2000 years ago used to scare our far ancestors.

1.2 Reproducing the world across the scales: from supramolecular to supracolloidal

Since the core concept of supramolecular chemistry was introduced from J-M. Lehn[4,5] (Nobel Prize in 1987, with Pedersen and Cram) a lot of steps forward have been done regarding the comprehension and the applicative implications of such relatively new field. Mesoscopic scale, the so-called order of magnitude beyond the micron, has been classified as an intermediate integration step between the subatomic length scale and the big complex organized matter. [6,7] The chemical components, defined until 80's like mere chemical substances or complexes, able to interact chemically or physically, are now viewed like chemical modules which can give birth to diverse hierarchical motifs of organization, spanning different levels depending on the size and on complexity of the aggregated structure. What the contemporary colloidal science brought in the panorama is basically an expansion of these levels, breaking the limit dictated by the length scale, more and more imitating the self-assembly of natural hierarchical organized superstructures. From the mesoscale supramolecular chemistry, the new contemporary challenges in colloidal sciences are projected towards the supracolloidal level.[8] For the first time in 2003 *van Blaaderen* [9] and coworkers introduced the term "colloidal molecule" to define a supracolloidal structure, coming from the interaction among colloidal spherical units, and specifically resembling the colloidal analogues of a simple molecular valence shell electron pair repulsion (VSEPR) space-filling model structure. Although other type of colloidal molecules have been proposed in the last few years.[10,11,12]

After almost 15 years the role of supracolloids, in an always expanding field like "soft-matter", is gradually acquiring more importance as more realistic becomes the perspective of a high profile technological device which could be built stepwise in solution rather than 3D-printed or sculptured, with diverse instruments and materials (what in few words is called "top-down" approach in nanotechnology).[13] During the last years very effective pathways bringing to the formation of colloidal superstructures have been discovered in the light of new technological applications. Furthermore, from an applicative standpoint best efforts are pointing to three-dimensional colloidal lattices with high grade of order.[14,15,16,17] Nanophotonics, the result of a big knowledge expansion in the field of photonics, aims to use these colloidal crystal lattices to dig deeper in the behavior of ordered nanostructured materials when they are interacting with electromagnetic radiation[18,19] such as visible light, trying to copy what Nature easily achieves with highly complex self-assembled structures.[20] Enlightened by the relatively recent progress in the top-down preparation of systems capable of non-trivial interactions with electromagnetic radiation, colloidal assemblies of nanoparticles are gaining more attention as an alternative,

bottom-up[21,22] approach to build colloidal three-dimensional ordered assemblies.[23] It is well known that the use of isotropic colloidal particles, assembled through excluded volume effect,[24,25] allows in principle to build high ordered three dimensional structures, capable of emulating the atomic lattice of a crystal, on a colloidal scale. As a matter of fact, colloidal solutions represent one of the best options through which supracolloidal crystals can be obtained. Just to mention, electrostatics and depletion interaction are two of the most direct and prolific ways to get such assemblies,[26].Besides, is also true that isotropic particles self-assembled via electrostatic or in general non-specific interactions lack of directionality, limiting the variety of the final nanostructured material patterns. The advantage given by the anisotropy of the interaction instead allows to overcome this issue, typical of bottom-up processes, and to enable the co-assembly of structured and periodic materials with very highly variable hierarchy and strong control over it.[27] In this respect many anisotropic building blocks have been studied apart from the already mentioned "spheres with valency" - colloidal molecules; anisotropy can be imparted by branching,[28] patching,[29] patterning[30] and as this dissertation will demonstrate, by creating a mixed systems using particles with different features (Figure 1.2).

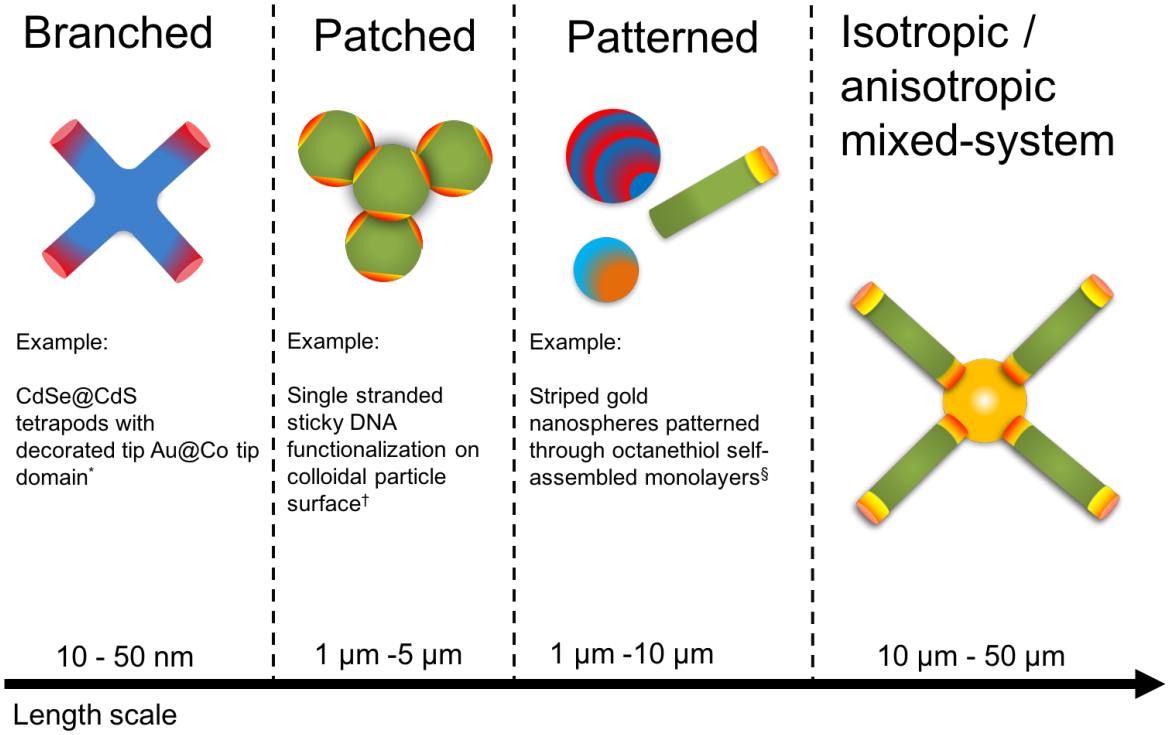

*Pavlopoulos, N. G., Dubose, J. T., Pinna, N., Willinger, M.-G., Char, K., and Pyun, J. *Angew. Chem. Int. Ed.* 55, 1787–179 (2016)..
†Wang, Yu., Wang, Y., Breed, Dana R., Manoharan, Vinothan N., Feng, Lang, Hollingsworth, Andrew D., Weck, Marcus, Pine, David J. *Nature*, **491**, 7422 (2012)
§Jackson, A. M., Hu, Y., Silva, P. J. & Stellacci, F.. *J. Am. Chem. Soc.* **128**, 11135–11149 (2006).

Figure 1.2. Representation of different types of supracolloidal building blocks based on different types of induced anisotropy.

Among the common pathways to get anisotropic interactions among nanoparticles, the use of colloidal patchy particles seems right now to be the most promising.[29] The group of *Gröschel et al.* [31] synthesized different patchy particles tuning the valence of the basic unit or, in other words, their patchiness. This tunability of the assembly behavior, and of course of the final structure obtainable, is given by the different chemico-physical properties of the polymer chains the particles are made of, playing with their theta conditions in the specific solvent used. In another study from *Mihut et al.* [32] the interaction is directed and based on an elegant lock-and-key mechanism between two complementary shaped nanoparticles.[33] Finally, has been demonstrated the very high reliability of using different force fields as external driving forces to direct the supracolloidal assembly (electric, magnetic or shear fields) among isotropic or anisotropic nanoparticles.[34] *Crassous et al.*[35] reported the formation of giant hollow fibers formation as outcome of the supracolloidal self-assembly of ellipsoidal dielectric particles triggered by the exposition to an external AC force field. As mentioned, the added value of these techniques relies on the possibility to direct the interaction potential on the single particle surface, expanding the limit of the hierarchical organization geometries. This issue, the directionality of interaction, is becoming nowadays particularly felt in nanoengineering because of the growing interest in nanophotonics applications. Despite the big variety among organic and inorganic materials such as metals, silica, polymers etc., these implications rise the bar of the difficulties the scientist are facing in the field. When speaking about colloidal crystals, one of the most requested feature a colloidal crystal should have, whose the study is aimed to the preparation of a hypothetical nanophotonic device, is the facile tunability of the band gap it produces when interacting with light.[1,36,37,38] This feature underlying the whole field of applicability of these lattices is strictly dependent on the difference between the refractive index of the dielectric material and the dispersant, on the distance among colloidal particles and on the type of lattice. So far, supracolloidal assemblies of isotropic colloidal units have been studied abundantly and their importance relies on their use as means to understand the colloidal lattices assembly mechanisms and properties. Although a lot of efforts still have to be done in order to get new types of lattices with new materials and to make inter-particle distances inside of them tunable. With respect to this, this study reports also the preparation of a mixed isotropic/anisotropic model system exploiting the introduction of anisotropic particles as spacers among adjacent spherical units. The programmability in terms of inter-particle spacing and the high specificity of interaction with isotropic spherical particles, imparted from the tubular anisotropic structures used, could represent a revolutionary pathway that in turn could enhance the progress in the entire field of research.

1.3 Bile Salts (BSs) and Bile Salts Derivatives (BSDs) as versatile building blocks for nanomaterials preparation

It is well known that surfactants play a leading role in modern scientific research.[39,40,41] They cover a wide spectrum of applications bringing together fields like nanochemistry[42], biomaterials science[43–45] and medicine,[46,47,48] representing in several aspects the cutting edge of nanotechnology. Common head-tail structured surfactants are widespread in literature: these molecules are very versatile instruments, able to work as nanoparticle stabilizers and ligands [49] or, in the aggregated form,[50] as templating surfaces[51] and encapsulating agents. More specifically, biological surfactants are starting to be even more diffused thanks to their bio-compatibility and bio-degradability features,[52,53] especially when the field of application is bio-oriented. However, within this wide panorama, bile acids and bile salts derivatives occupy a niche but important position, having some additional chemical features given by their unconventional amphiphilic structure. Found predominantly in the bile of mammals, they have some pivotal biological functions as emulsifiers and lipids solubilizers inside the human body.[54] BSs are a synthesis product coming from cholesterol metabolism and, consequently, are characterized by a cyclopentane-perhydrophenanthrenene steroidal skeleton. In addition to this, depending on their type and biological function, they can bear up to three hydroxyl groups on C_{12}, C_7 and C_3 with different stereochemistry and an aliphatic side-chain bearing a carboxylic or a sulfonic moiety[55] that can be found conjugated with amino acids such as taurine and glycine.[56] The basic structure and nomenclature is given in the following figure.

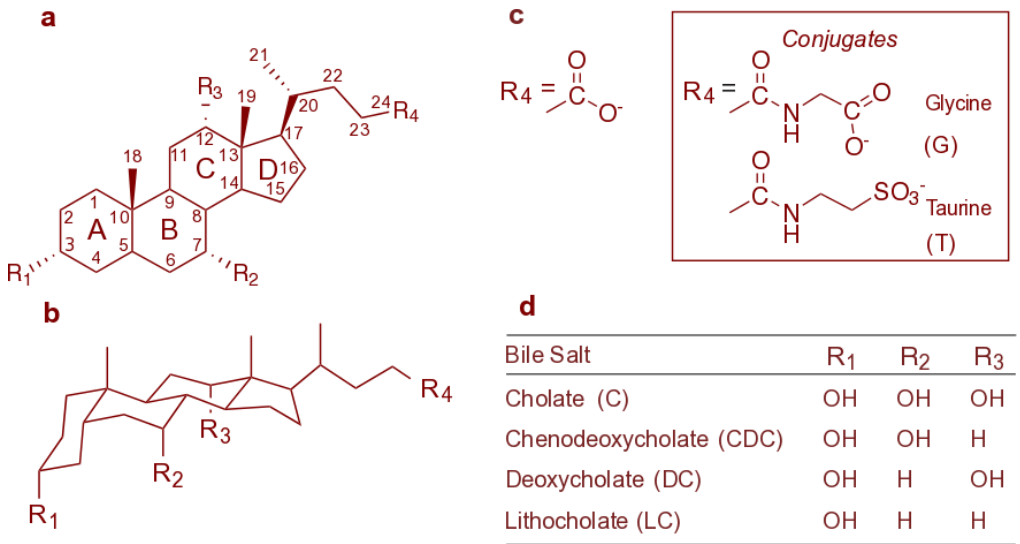

Bile Salt	R_1	R_2	R_3
Cholate (C)	OH	OH	OH
Chenodeoxycholate (CDC)	OH	OH	H
Deoxycholate (DC)	OH	H	OH
Lithocholate (LC)	OH	H	H

Figure 1.3. Representation of planar (a) and chair (b) molecular structure of a generic BS. Specification of R_4 conjugation with aminoacids is given in (c) and corresponding nomenclature based on R_1, R_2 and R_3 moieties is reported in the table (d).

Different kinetics studies[57–59] proved that bile acids and BSs have an intriguing self-assembly behavior when critical aggregation concentration (*cmc*) is exceeded: low aggregation number micelles, secondary micelles, bilayers and different kind of highly anisotropic structures can be formed. In each case, supramolecular arrangement is heavily influenced by the "facial" distribution of the hydrophobicity along the molecule (depending on –OH groups number and orientation) and by the rigidity of the steroidal group. Also hydrogen bonding has been suggested to have implications in their rich self-assembly behavior[60] which is the key point on which the research focused the most during the last decades. An accepted model for BSs self-assembly pathway is represented by the organization of the molecules back-to-back in order to direct the hydrophilic faces towards the water, this model seems to be the point in common among different models proposed for BSs micelles formation in aqueous solutions[61]. Above the *cmc,* a fundamental part of the self-assembly process is represented by primary and secundary micellizations, as suggested by several studies produced by different research groups.[62,63,64,65] Chirality plays an important role as well on the type of self-assembled structure. As many circular dichroism measurements have confirmed in previous studies, the rigid molecular packing follows helicoid patterns within the folded bilayers. This reflects on the complexity of the self-assembled structure that is most of the time able to form rod-like[66,67] and tubular structures.[68,69]

Interestingly, auto-aggregation behavior of these molecules can be expanded when chemical modifications are performed on the steroidal skeleton. The possibility to functionalize BSs, obtaining BSDs enhances the self-assembly behavior and expands the horizons of the applications of such compounds.[70] Many examples of BSDs have been synthetized with the aim to obtain supramolecular aggregates suitable for biotechnological applications. Amino acids[71,72] and sugars[73] have been chemically attached to the steroidal skeleton in different positions, usually on C-3 and C-12, while modifications on the C-24 of the lateral carbon chain have as well been achieved.[74–77]

BSDs self-assembly is often triggered by slight changes of internal parameters of the BSDs aqueous solution, like pH and ionic strength,[78] or even external parameters, like temperature and light exposure[79] and can be imparted both in pure or mixture solutions of different BSDs. One of the most important developments in this respect, is the possibility to prepare catanionic mixtures of two oppositely charged BSDs molecules modulating the electrostatic overall charge of the aggregate, without any implication for the molecular packing: approach already successfully attempted in two previous works.[80,81] This behavior can be justified taking into account that the molecular structure of the two derivatives is identical except for the charged

head. Interestingly, in this conditions the electrostatic interaction between oppositely charged heads favors auto-aggregation, reducing the concentration of free monomer in solution at a much lower concentration than the cmc of the pure derivatives.

This characteristics of BSDs catanionic mixtures make them particularly suitable building blocks for a controlled electrostatic interaction. Like in the case of tert-butylphenoyl-amino derivative of cholic acid[80] or of the adamantyl-amino derivative of the same bile acid,[81] tuning the ratio between positive and negative counterparts makes possible to control the shape of the aggregate influencing heavily the strength and position of the residual charge distribution on the particle surface, that could be eligible for electrostatic interaction with other charged colloids such as polymeric or metallic particles, allowing for the preparation of hybrid supracolloidal frameworks with a gradual and stepwise pathway, without resorting to additional functionalizations or organic/inorganic treatments like, for instance, polymer coating[82] and silanization.[83] As already mentioned, nanomaterial engineering cutting edge preparation techniques are basically exploiting patchiness to direct interaction among isotropic colloidal units binding sites, limiting enormously the hypothetical potential of these materials. State of the art preparation of colloidal molecules takes advantage of patchy particles synthesized by sintering, with DNA oligomers or polymer tethers able to strengthen and direct the interaction with the other colloidal units. Although these pathways are far away to be considered something else than mere "spheres with valencies". Among few works not undertaking this direction, *Mokari et al*. [84] reported CdSe quantum tetrapods formation having Au caps on the tips. These anisotropic metallic nanoparticles with controlled tips reactivity don't show interaction behavior unless functionalized with hexan dithiol bifunctional linker, adding another step of preparation and increasing the preparation pathway complexity. In this respect BDSs can be decisive: in some types of BSDs self-assembled tubular structures, tips specificity comes naturally as an intrinsic feature of the aggregate. When mixed with colloidal spherical units, not reporting any patchiness, they spontaneously form core-corona assemblies where the final geometry of the unit can be roughly controlled tuning the ratio between the radius of the tubule and the one of the spherical particle. Using a tubular linker among spherical colloidal particles might, in principle, bring not only to new types of colloidal molecules, where the bonds are actually represented by elongated tubular structures but also, exploiting their binding site features, to new low density materials with interesting rheological or even mechanical properties, characterized by full spanning network formation with different connectivity, density and framework pattern.

1.4 Experimental Techniques

1.4.1 Confocal Laser Scanning Microscopy (CSLM)

Colloidal science investigates on materials characterized by sizes in the order of magnitude of both nano- and micro- scale. The increasing interest towards the mesoscale, together with the recent advances in optics, made of optical microscopy a pivotal tool used in a wide spectrum of research fields like, for instance, surface studies, directed self-assembly characterization, photonics and drug delivery, filling the gap left by the electronic and probe microscopies. More specifically, Confocal Laser Scanning Microscopes (CSLM) have gained much more attention over the past years with respect to their close parents, the epifluorescence microscopes, thanks to their better applicability and adaptability to the specific specimens under the focus of nanomaterial related applications. In a typical CSLM, a point-like illumination source (*i.e.* monochromatic laser) is used to lit the sample, providing a discrete band of wavelengths with high intensity, already an essential advantage for standard fluorescence investigation. Photomultipliers (PMTs) are employed as detection system to collect the intensity coming from the specimen providing high dynamic range and high refresh rate allowing for data collection at nanoseconds level. A part from these very general instrumental features the key factor of the CSLM is the use of a set of pinholes placed near the objective and near the detector to select the desired beam intensity and to block away all the wavelengths coming from upper and lower focal planes. This implies several implemented aspects: the elimination of interferences coming from lateral stray light, the void of superimposed out-of-focal plane signals, the possibility to scan only optically selected slices of the specimen with a thickness depending on instrumental *z*-resolution, and an improved "lateral" *xy*-resolution due to better wave-optical performance. This mentioned aspects in turn have as a results higher contrast, lower blurring effects, sharper images and fine depth discrimination. A basic scheme of a CSLM is given in Figure 1.4. Since length scale of colloidal objects may be very demanding in term of resolution, Point Spread Functions (PSFs) have to be reduced in order to respect the Rayleigh criterion (or the Full Width of Half Maximum -FWHM- criterion). The diffraction limit imposed by the lenses to the resolution of the microscope comes from the well-known Abbe equation (eq 1.1):

$$r = \frac{\lambda}{2NA} \qquad (1.1)$$

Where λ is the radiation wavelength and *NA* is the numerical aperture of the microscope. CSLM noticeably allows to reach resolutions below the diffraction limit thanks to the possibility to manually or automatically change the pinhole size influencing the size of the diffraction pattern, called Airy Disk, described quantitatively by Airy Units (AU). Consequently, the increase of both lateral and *z*-axis resolution is obtained when Airy Disk is reduced (Figure 1.4, right panel). On the other hand, since pinhole cuts a relatively high amount of wavelengths, the intensity reaching the PMT is weak, meaning that when the Airy Disk is below 1 AU and approaches, or even goes below, 0.25 AU the resolution advantage is completely covered by the increased signal-to-noise ratio (SNR) given from the low intensity and basically caused by the strong reduction of the detecting volume. The experiments commented in the following dissertation were all performed at 1 AU, which seemed the right agreement between intensity signal, SNR and required resolution. For the instrument used in this work, considering the emissions employed ($\lambda_{He\text{-}Ne}$ = 568 nm, λ_{Argon} = 476 nm) the pinhole size (1 AU), the objective (oil imm. 100x 1.4NA), the resolution of the microscope was around 150 nm.

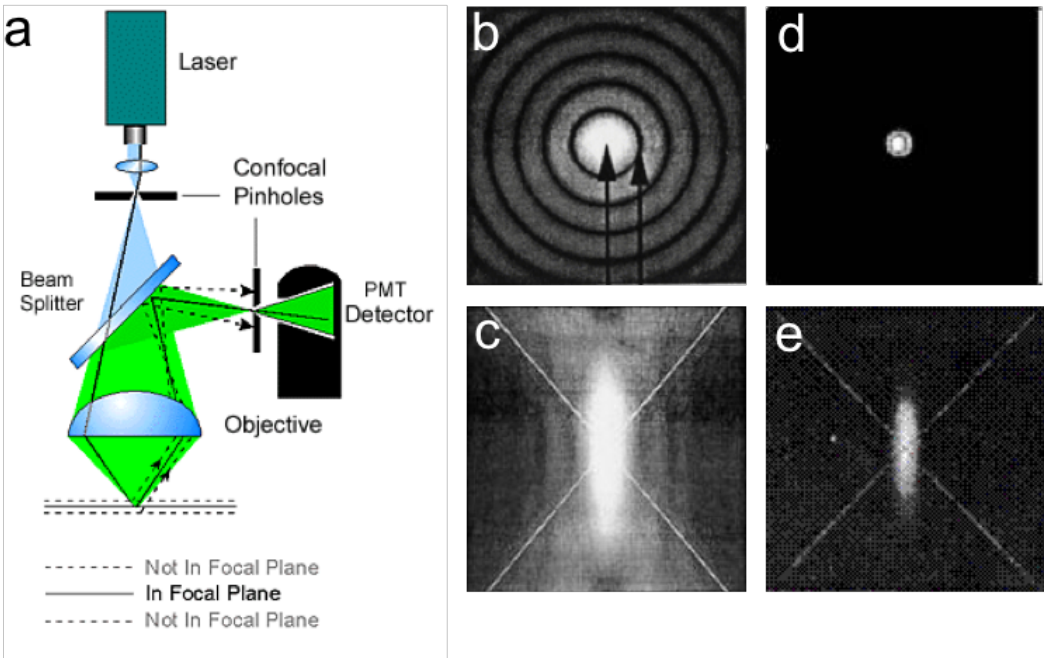

Figure 1.4. Basic scheme of CSLM optics (a). Effect on the PSF before (b and c) and after (d and e) the use of the pinhole, respectively on the *xy*-plane (b and d) and on the *zx*-plane (c and e).

CSLM still is a fluorescence microscope. Fluorescence excitation is one of the most used mechanisms in nanomaterial studies. CSLM is able to fit particularly when is requested to catch fluorescence emission from thick samples, exactly where a common fluorescence microscope would fail. Severe background suppression is an essential feature for the proper imaging of thin detection volumes within thick samples, making possible the accurate analyses of nanoscale

and mesoscale phenomena occurring at colloidal level. Moreover, multi-channel detection can be performed simultaneously setting different PMTs dedicated to different emission channels focused on the emitting probes within the specimen in analysis. In this study, a maximum number of two PMTs was used. In dispersed systems like those reported in this work microscopy does not fulfill the need to a general overlook to the sample properties as the images taken might be representative of only a small portion of sample. This issue is overcome easily with complementary techniques such as light and X-rays scattering, rheology and spectroscopies. However is possible to enlarge CSLM analysis perspective through 3D-reconstruction of acquired *z*-stack images. Single optical sections of the transmission and all the corresponding fluorescent emission channels selected, acquired singularly, can be stacked to form 3D reconstructions representing the sample on a more reliable length scale. In this work, 3D-reconstructions are reported as orthogonal color coded *z*-projections with colors from deep blue to intense red depending on the relative *z*-coordinate. The *z*-resolution, which is a fundamental parameter for CSLM as the lateral resolution, is controlled as well by the pinhole size and its value is approximatively two times the lateral resolution, approximately 325 nm (as reported on Leica SP2 LAS AF software).

Confocal micrographs were recorded on a Leica SP5 confocal laser scanning microscope operating in the inverted mode (D6000I), using a 100X/1.4 NA immersion objective. The microscope was mounted in a thermostated enclosure which provides a temperature stability of ±0.2°C. The samples were maintained between two cover glasses separated by a 120 mm spacer (Grace Bio-Labs SecureSeal imaging spacer).

1.4.2 Electron Microscopy

Electron microscopy[85,86] was used to carry out complementary imaging analyses on the sample studied in this work since optical microscopy does not provide a resolution sufficient to appreciate features in the order of tenth of nanometers. This issue is related to different factors: the first is the wavelength of the incident beam of the radiation illuminating the sample: as fundamental principle, higher resolutions can be reached only with radiations having shorter wavelengths. Moreover, the technologic improvement of optical systems, and in particular of the lenses as primary optical components, struggles against the impossibility to increase *ad*

infinitum, the *NA* because of the equation $NA = n\sin\mu$, where n is the refractive index of the medium and μ the angle described by the inverted cone of light reaching the objective.
Finally, optical aberrations increase exponentially with the increase of size and convexity of the optical lenses. Electron microscopy allows then to bypass the diffraction limit through the use of an accelerated electron beam. The beam can be produced via thermionic effect by the tip of a field emission gun (FEG) instead of the UV-vis radiation produced from either a laser or a lamp sources typical of the optical systems, reaching a resolution ideal for specimens having sizes between the angstrom and the nanometer. This can be explained taking into account the equation 1.4 that, starting from the famous De Broglie equation (1924), relates the acceleration voltage of the instrument with the electron wavelength and in turn its resolution:

$$\lambda = \frac{h}{p} \qquad (1.2) \qquad eV = \frac{m_0 v^2}{2} \qquad (1.3)$$

$$\lambda = \frac{h}{(2\, m_0 eV)^{1/2}} \qquad (1.4)$$

Where λ is the wavelength, h is the Planck's constant, p the momentum, m_0 the electron mass, v the velocity, eV the kinetic energy. Of course at energies greater than 100keV, because of the velocity of the electrons (half of that of the speed of light), relativistic implications cannot be neglected, then equation 1.4 becomes:

$$\lambda = \frac{h}{[2\, m_0 eV(1+\frac{eV}{2m_0 c^2})]^{1/2}} \qquad (1.5)$$

Where c is the speed of light.
Imaging of electron microscopy is based on the interaction of such emitted electrons with the atoms of the specimen. When these particles (accelerated by a series of anodes) up to 200 keV hit the sample a series of phenomena is triggered: from Auger emission, to both elastic and inelastic scattering of electrons, to X-rays emission. Image is produced either in Bright field contrast (BF) or in Dark field contrast (DF) mode, respectively collecting the transmitted or the scattered electrons. In this work Transmission Electron Microscopy (TEM) was used as Electron Microscopy method of investigation which is mainly based on the information carried by elastic electron scattering constituting the major source of contrast in TEM[87]. A general schematic representation for a TEM is given in Figure 1.5. Each instrument has the source

positioned over the top of a columnar chamber kept under high or ultra-high vacuum, respectively in the order of 10^{-5}, 10^{-9} Pa. A two stage condenser lens provides variations of the illumination aperture and consists in a series of tetra-poles or hexa-poles. The beam hits the sample contained in the sample holder. The objective lens is placed below the sample.

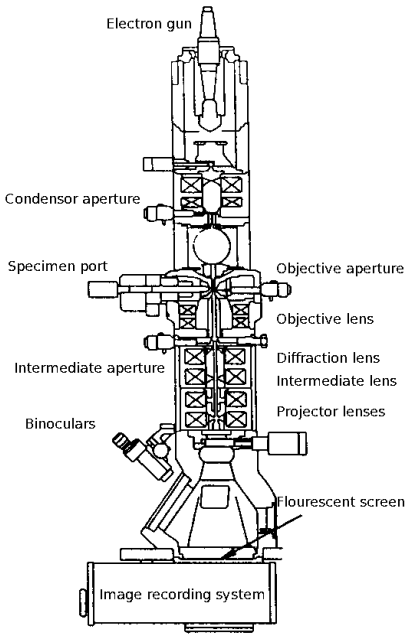

Figure 1.5. Scheme of a transmission electron microscope.

After the objective, a series of projector lenses magnifies the image or the diffraction pattern then collected by the detection system. A specific cryogenic TEM (cryo-TEM) was employed to perform the measurement as the sample could not be imaged properly in dry conditions. With cryo-TEM is possible to work in cryogenic conditions, *i.e.* below 150°C, allowing for the study of soft matter materials when the preservation of spontaneous microenvironment has the priority, like for instance in the case of surfactant based self-assembled system. The sample is vetrified plunging the grid, where the sample has been previously deposited, in liquid ethane after a blotting procedure for the elimination of the exceeding amount of liquid from the copper grid. The vetrification is performed to avoid crystallization of water that produces diffraction of the electron beam and consequently blocks the primary beam causing signal deterioration.

The microgel samples for TEM imaging were prepared dropcatsing a 1wt% particle solution on a carbon-coated copper grid with a 300 mesh, placed on a paper filter at room temperature. The micrographs were acquired through a TEM-CM100 (Philips) operating at 80 kV and a JEM-2200FS transmission electron microscope, operating at 200 kV and with a FEG source.

Cryogenic electron micrographs on bile salt derivative aggregates were acquired with cryogenic electron microscopes FEI Tecnai 12 G2 and JEM-2200FS operating at an acceleration voltage of 120 kV and 200 kV, respectively. The samples were vitrified with a humidity controlling[88] automated system using a Cu TEM grid, coated with a holey carbon film at 25°C. The sample were prepared depositing a drop on the grid and blotting from behind to remove excess fluid. Vitrification was performed through rapid plunging into liquid ethane at its freezing point. The samples were then imaged at -178°C.

TEM images of bile salt mixture tubular aggregates were recorded by TEM at room temperature using a JEOL JEM-1011, operating at 80 kV, equipped with a MegaView III camera. A drop of the samples was deposited on a carbon-coated copper grid, leaving the specimen for 10 minutes to allow the sample to permeate the grid. Drop excess were then removed through blotting.

1.4.3 Dynamic Light Scattering (DLS)

Scattering techniques represent a powerful tool to characterize colloidal sized samples.[89] Although scattering techniques have a wide range of instrumental setups and applications, they have the same basic principle. An incident beam coming from a point-like source (like for instance a laser or an X-ray source depending on the aim of such analysis) lits the specimen held inside a cuvette, generating scattering of the beam. As a general concept, when an electromagnetic radiation interact with matter part of it is transmitted, part is absorbed, but frequently, if the sample contains colloidal particles in the medium, part of it can also be scattered in all directions, through the so called Tyndall effect. The scattering is produced by both elastic and inelastic phenomena. The source of the most reliable information is contained inside the elastically scattered radiation, meaning that the λ of the scattered beam is the same of that of the incident beam, then no energy loss took place during the interaction. The scattered intensity is not homogenously distributed around a scattering sample, but grows in anisotropy as the scattering particles gets bigger. The scattered intensity is detected at a chosen angle ϑ defined as the angle between the wave vectors of the incident $\overrightarrow{k_i}$ and the scattered $\overrightarrow{k_s}$ beams. Scattering vector $\vec{q}$ is the most important factor to take into account in scattering phenomena, it is the result of the subtraction between $\overrightarrow{k_s}$ and $\overrightarrow{k_i}$ and has an intensity equal to

$$q = \frac{4\pi sin\left(\frac{\theta}{2}\right)}{\lambda} \qquad (1.6)$$

where λ is the wavelength of the incident beam. Particles dispersed in a medium, able to diffuse in Brownian regime, imply concentration fluctuations in the medium volume elements which in turn have as a result fluctuation of the scattered intensity. Differently from static light scattering (SLS) where the detector collects intensity fluctuation over time and averages the signal, in DLS the mere discrete fluctuations are considered as the decay of an intensity autocorrelation function $g_2(t)$ and an electric field autocorrelation function $g_1(t)$. Let's consider a generic property of the system, *A* at the equilibrium which can be interpreted as an average of that property over time:[90]

$$< A(t) > = \frac{1}{t} \int_0^{t0+t} A(t)dt \qquad (1.7)$$

Where t_0 is the time at which measurement starts and *t* is the measuring time. The measuring time definitely should be longer of the time taken by a single fluctuation. Moreover, independently from the starting time selected, the value of *A(t)* should be identical at each measurement performed during the whole time span, to make the ergodic hypothesis valid. Las equation can be rewritten as:

$$< A(t) > = \lim_{t\to\infty} \frac{1}{t} \int_0^t A(t)dt \qquad (1.8)$$

This relationship brings with itself an important property which imply that when *A* is detected on a time increment δt, small enough with respect to *t*, then *A* $(t + \delta t)$ will be close to *A(t)*. Increasing the measuring time, *A(t)* and *A* $(t + \delta t)$ become more and more non correlated. An autocorrelation function of the generic property *A(t)* can be at this point defined as:

$$< A(0)A(t) > = \lim_{t\to\infty} \frac{1}{t} \int_0^t A(t)A(t + \tau)dt \qquad (1.9)$$

This autocorrelation function decays from its original initial value in a time span indicated as relaxation time, characteristic of *A*. In typical DLS experiment the properties investigated are the fluctuations of the electric field and of scattered intensity, related to the Brownian motion of the suspended particle inside the specimen. These fluctuations allow to extract precise

information about translational diffusion of the particles, making possible to know their size with a rather high agreement with the microscopy techniques. The time correlation functions (TCFs) of scattered intensity and of the electric field can be written as:

$$g^{(2)}(q,t) = \frac{\langle I_{(q,0)} I_{(q,t)} \rangle}{\langle I_{(q)} \rangle^2} \qquad (1.9)\ ; \qquad g^{(1)}(q,t) = 1 + \beta \left[g^1{}_{(q,t)} \right]^2 \qquad (1.10)$$

Which are related by Siegert relation[91]. I (q,0) and I (q,t) represent the scattered intensity at time 0 and after a time t, while β is a parameter related to deviation from ideal correlation and is strongly dependent from the geometry adopted. For spherical particles the TCF can be fitted by a single exponential decay function:

$$g_1(t) = \exp(-Dq^2 t) \qquad (1.11)$$

Where D is the mutual translational diffusion coefficient which is defined as $D = \lim_{q \to 0} (\Gamma / q^2)$ and Γ is the relaxation rate. Stokes-Einstein equation relates the diffusion coefficient at the infinite dilute concentration (D_0) to hydrodynamic radius of the particles:

$$R_H = \frac{kT}{6\pi\eta_0 D_0} \qquad (1.12)$$

Where k_B is the Boltzmann constant, T the absolute temperature in K and η_0 is the solvent viscosity. Since D is introduced in the equation and not D_0, this technique provides an apparent hydrodynamic radius $R_{H,app}$ which includes inter-particle interactions.

For kinetic studies on BSD/Microgels mixtures an ALV/DLS goniometer system from ALV-GmbH, Langen, Germany was used. The light source was a He-Ne laser with a wavelelngth of 632.8 nm, with an intensity automatically controlled by an attenuator. A laser Glan polarizer prism allows for vertical polarization. Experiments were run at 20°C, at variable angles.

For the experiments on colloidal crystals in a BSD gel matrix, a 3D-DLS goniometer from LS instrument incorporating a cross correlation technology for multiple scattering contributions suppression was used.[92,93] The instrument is equipped with a 35mW He-Ne laser with a

wavelength of 632.8 nm. Cells are immersed in refractive index matching liquid and thermostated by a Julabo temperature controlling unit (±0.1°C). Scattered light is detected by two Avalanche Photo Diodes and processed by a Flex correlator when 3D cross correlation mode is activated. For all the DLS measurements the specimens were analyzed in borosilicate glass cells immersed in a VAT unit filled with refractive index liquid matched with the cuvette glass (decahydronaphtalen, cis-trans mixture). The temperature was controlled by a Julabo heating circulator (±0.1°C).

1.5 Complementary Techniques

1.5.1 UVvis Spectroscopy and Circular Dichroism

The UVvis spectra of BSDs and BSD mixtures were recorded on a Cary/1E and a Varian Cary 50 spectrophotometer in the range of wavelengths (λ) 600 - 250 nm and reported in molar extinction coefficient ε (UV). Typical data interval of 0.5 nm and an average time 0.1 ns, were used. CD spectra were recorded on a JASCO model 715 and reported in molar ellipticity [θ] (CD). The spectra were recorded in the range of wavelength (λ) 200–350 nm and the temperature was controlled by a Peltier unit, with an accuracy of 0.02 °C. Quartz cuvettes with path lengths ranging from 0.1 to 1 mm were employed. The reported spectra are results of four scans and solvent baseline correction.
UVvis spectra of the pure BSD solutions were recorded with, with a data interval of 0.5 nm and an average time 0.1 ns.

1.5.2 Zeta Potential and Eletrophoretic mobility

A Malvern ZetaSizer Nano-Z equipped with a He-Ne laser with automatic laser attenuator was used for electrophoretic mobility measurements. Disposable folded capillary cells were used as sample cells. The measured electrophoretic mobility of the microgels suspension (0.1 wt%) is stated as the average of 20 consecutive measurements at 20°C.

1.5.3 Fluorescence Spectroscopy and Time Correlated Single Photon Counting (TCSPC)

A Fluoromax 2 instrument (Horiba-Jobin Yvon) was used to perform the steady state fluorescence measurements. The instrument was equipped with a LUMA 40 / JY1 Peltier sample holder (Quantum Northwest) controlled with a TC1 unit (Quantum Northwest). Temperature measurements were allowed by the use of a QNW-1 (± 0.01°C) probe thermistor plunged in the sample.

For the Time Correlated Single Photon Counting (TCSPC) was used a local designed fluorimeter equipped with an excitation source represented by a PicoQuant GMBH LDH-375 laser diode with emission at λ_{exc} = 378 nm (resolution: 44 ps, v_0: 40 MHz; 85 pJ / pulse).[94] The instrument is equipped with a Spectral Product CM110 monocromator and a Hamamatsu R3809U-50 detector. The photon counting was performed through an acquisition card with the corresponding acquisition software (PicoQuant TimeHarp 200 and TimeHarp 6.1, respectively). TCSPC analyses were performed with PicoQuant FLUOFit 4.4.

1.6 Building blocks

1.6.1 Tert-butylbenzoyl- and naphtoyl- amine- derivatives of Cholic Acid

1.6.1.1 Tert-butylbenzoyl amine- derivatives of Cholic Acid supramolecular aggregates

An anionic derivative of cholic acid (ACD) was prepared as a result of a derivatization on C-3 belonging to cholic acid steroidal skeleton where a tert-butyl-phenyl pendant was attached through an amide bond to grant a hydrophobicity distribution enhancement along the bile salt molecule.[79,95,96] With the aim to prepare catanionic mixtures, a positive analogue of ACD (CCD) was synthesized, bearing a positively charged quaternary ammonium salt instead of the carboxylic moiety. Supramolecular BSDs tubules were formed either from a mixture solution of the two oppositely charged cholate derivatives. The molecular structures are reported in Figure 1.6.

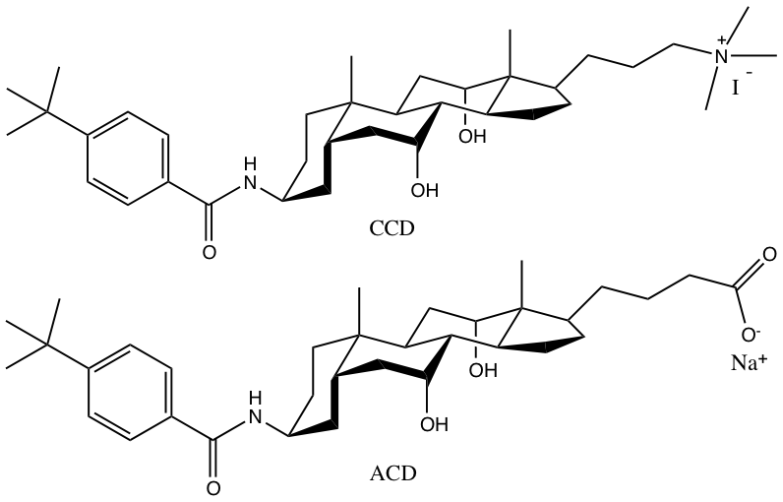

Figure 1.6. Molecular structure of the two bile salts derivatives of cholic acid named respectively CCD (top) and ACD (bottom).

Adjusting the surfactant composition in term of ACD/CCD ratio in aqueous solution, it was possible to tune the overall charge of the aggregate with rather high precision. In a previous work[80] were already reported electrophoretic measurements demonstrating how the ACD/CCD composition of the tubules was dependent on the mixture solution composition. The general trend of the electrophoretic mobility varying the CCD fraction inside the catanionic mixture is reported in Figure 1.7. Besides, was possible to exploit this feature in order to tune the charge of the tubular aggregates reasoning, more conveniently, in terms of the anionic derivative molar fraction $X_{ACD} = n_{ACD}/n_{tot}$ in solution (where n_{ACD} and n_{tot} are the number of moles of *ACD* and of the total surfactant, respectively), obtaining a series of aggregates having charge

spanning from highly negative (corresponding to ACD-rich aggregates) to high anionic derivative molar fractions ($X_{ACD} > 0.6$), to slightly positive (aggregates slightly richer in CCD) at low anionic derivative molar fraction ($X_{ACD} < 0.2$).

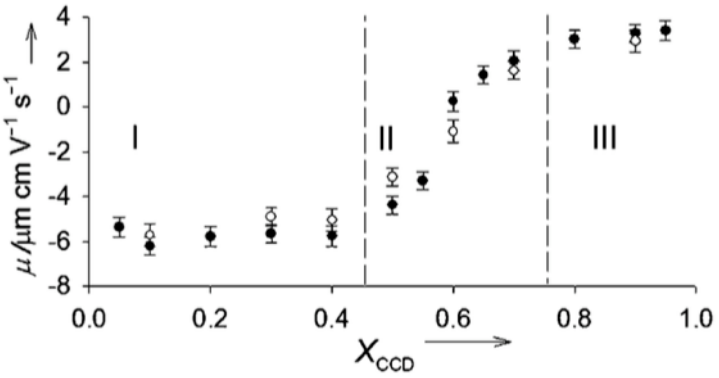

Figure 1.7. Electrophoretic mobility measurements for the complete ACD/CCD catanionic mixtures series.

The type of charge, the electrophoretic mobility and the dimensions of the corresponding tubular structures are summarized in **Table 1.1**.

X_{ACD}	**1**	**0.7**	**0.4**	**0.2**
Charge	Negative	Negative	Neutral	Positive
μ [10^{-8}m/Vs]	-4.87	-2.28	-0.34	+2.54
Length[1] [μm]	3-10	10-50	10-50	10-50
Width[2] [nm]	450	250	300	350

[1] Estimated by bright field microscopy and TEM
[2] Estimated by TEM

Table 1.1. Reported values for the electrophoretic mobility and size of the aggregates.

The peculiar tubular structure of the supramolecular aggregates for the pure ACD and for each ACD/CCD mixture composition was characterized in a previous study through different microscopy techniques.[80] In each case rolled supramolecular sheets were observed to form scrolls of superimposed layers as shown in Figure 1.8. Typically, the sheets can be triangularly shaped and rolled around an axis parallel to one of their sides. In this specific case, an oppositely handed helical marker was observed on the outer surface of these tubules (Figure 1.8, I). More seldom, molecular sheets with stair-shaped edges form the scrolls that thus present a seemingly telescopic structure, where the layer edges overlapping in well-defined rings, mark thick discontinuities on the outer surface (Figure 1.8, II). Cross section diameters as measured and

statistically averaged from the same micrographs change remarkably across the different mixture composition ratios from values near to 250 nm for the X_{ACD} = 0.2 to 350 nm for the X_{ACD} = 0.7. Apparently could not be performed any control over tubular length since the measurements revealed low monodispersity of lengths ranging from 10 to 50 μm, regardless the mixture composition.

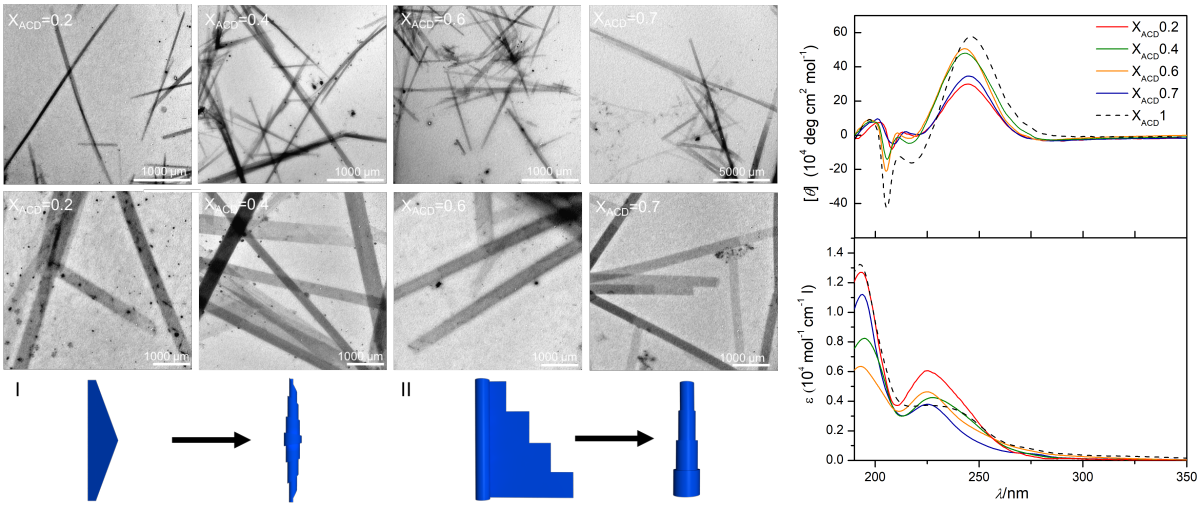

Figure 1.8. Cryo-TEM micrographs of supramolecular tubules with different X_{ACD} ratio (a). Corresponding CD and UVvis spectra (b). Adapted with permission from Ref 98. Copyright 2018 Wiley-VCH.

For each mixture, circular dichroism was performed and hence reported in Fig. 1.8 along with the corresponding UVvis spectra. Surprisingly, CD signals were found to be fairly similar when the ACD fraction was varied, implying that the molecular packing wasn't changing radically while the charge of the aggregate was efficiently being tuned. Moreover, X_{ACD} = 0.2 and 0.7 have common signals different in intensity with respect to fractions X_{ACD} = 0.4 and 0.6 signals. This is in agreement from what observed on TEM micrographs. When the X_{ACD} is far from equimolar ratio (1:1) the electrostatic driving force of aggregation suffers because of the presence of an excess of BSD in the monomeric form, which tends to aggregate as charged amorphous material, visible through TEM as black spots adhering to the outer surface discontinuities of the tubules. Single-walled and multi-walled structures, reasonably related to a scroll-like architecture sometimes shown in cryo-TEM micrographs (Figure 1.9) have been reported for the pure ACD solutions as well, depending on the preparation and aging. The aggregates, visibly smaller than those deriving from catanionic mixtures, have cross sectional diameters around 450 nm and a length ranging from 3 to 10 μm depending on the preparation procedure, and are characterized by a spacing among the walls of 13 nm as proven from previous small angle X-ray scattering characterization.[96] In each preparation, the aggregates

exhibit a low degree of polydispersity for both sizes. As demonstrated further, ACD is able to build up solutions with a rheological response typical of the gels, given by the entanglement of very long fibrils (Figure 1.10) at room temperature and in $Na_2CO_3/NaHCO_3$ buffer. The gel, when a well precise temperature transition is imposed within a well-defined buffer concentration-dependent range of temperature (34-50°C for the 30 mM buffer used in this study) further turns into a dispersion of negatively charged tubules. The transition was observed through both microscopy and circular dichroism where could be possible to appreciate the remarkable change in CD profile as the transition temperature was crossed.

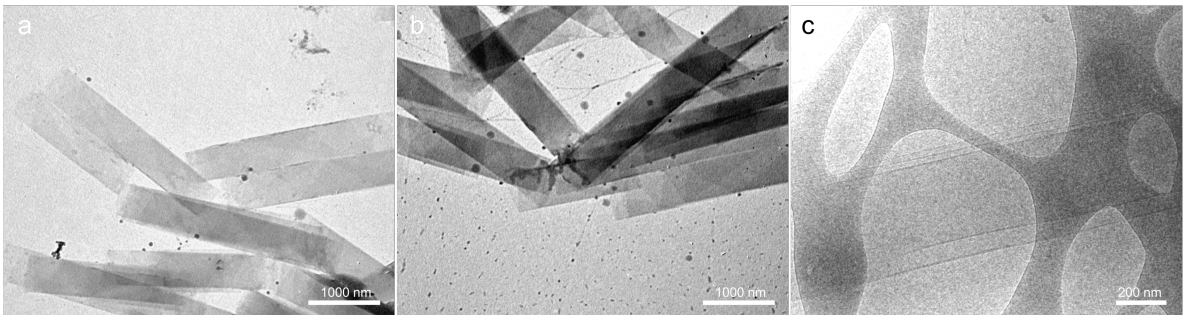

Figure 1.9. TEM micrographs of pure ACD supramolecular tubules. Adapted with permission from Ref. 98. Copyright 2018 Wiley-VCH.

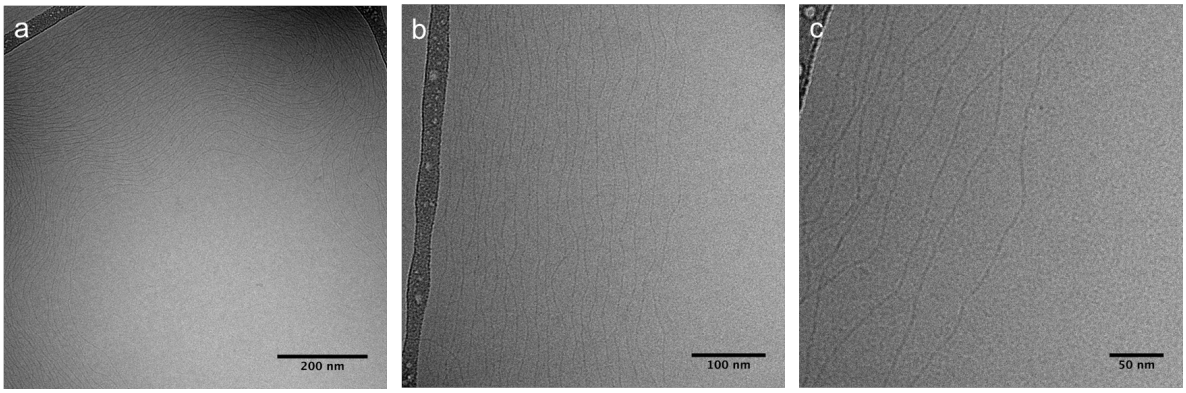

Figure 1.10. Cryo-TEM micrographs at increasing magnifications on 2mM ACD fibrils in 30 mM $Na_2CO_3/NaHCO_3$ buffer solution kept at room temperature.

For the interaction with microgels, ACD tubules were formed from a solution at 30 mM $Na_2CO_3/NaHCO_3$ buffer by heating the samples at 38°C for three days. Thereafter, the sample was equilibrated at room temperature before the microgels addition. The tubular aggregates prepared with the aforementioned protocol were observed to be stable for several weeks at room temperature. Electrophoretic mobility data confirmed the anionic nature of the aggregates (see Table 1.2). It is worthwhile noting that the aggregates formed by the pure ACD and by the mixtures at various X_{ACD} exhibit very similar circular dichroism profiles, suggesting that the

chiral packing of the molecules within tubular aggregates is very similar independent of their compositions.

For the experiments aimed to the preparation of PNIPAM microgels colloidal crystals, reported in Chapter 4, samples were prepared from a 2mM ACD solution in 30 mM $Na_2CO_3/NaHCO_3$ buffer, kept at room temperature to induce fibrils formation.

1.6.1.2 Nahpthoyl-amine- derivatives of Cholic Acid, supramolecular tubules

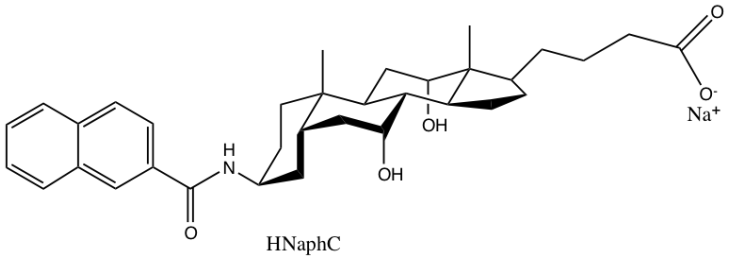

HNaphC

Figure 1.11. Molecular structure of the sodium salt of HNaphC

Multi-walled tubular structures were formed by the nahpthoyl-amine- derivatives of Cholic Acid (HNaphC) of Figure 1.11, by rising to 11.5 the pH of a 2mM bile salt derivative solution. It has been already demonstrated in previous works that these aggregates form within a wide spectrum of supramolecular structures induced upon pH or temperature variations (a summary is presented in Figure 1.12).[78,97] In facts, beside the multi-walled tubular structures at pH≥11.5, it has been reported the formation single-walled tubules at 8 < pH < 9 and the formation of helical or twisted ribbons at 9 < pH < 10, upon aging. Furthermore, it has been proven that multi-walled tubules at pH≥11.5 are broken by increasing temperature above 35-40 °C. Regarding to the length of the aggregates it has been found through electronic microscopy that they are 2-3 μm long at pH 8.5 while lengths of 7-9 μm are observed for the multi-walled tubular structures at high pH. From the latter single-walled tubules grow by aging reaching lengths up to 20 μm or even more and an increased polydispersity in term of lengths.

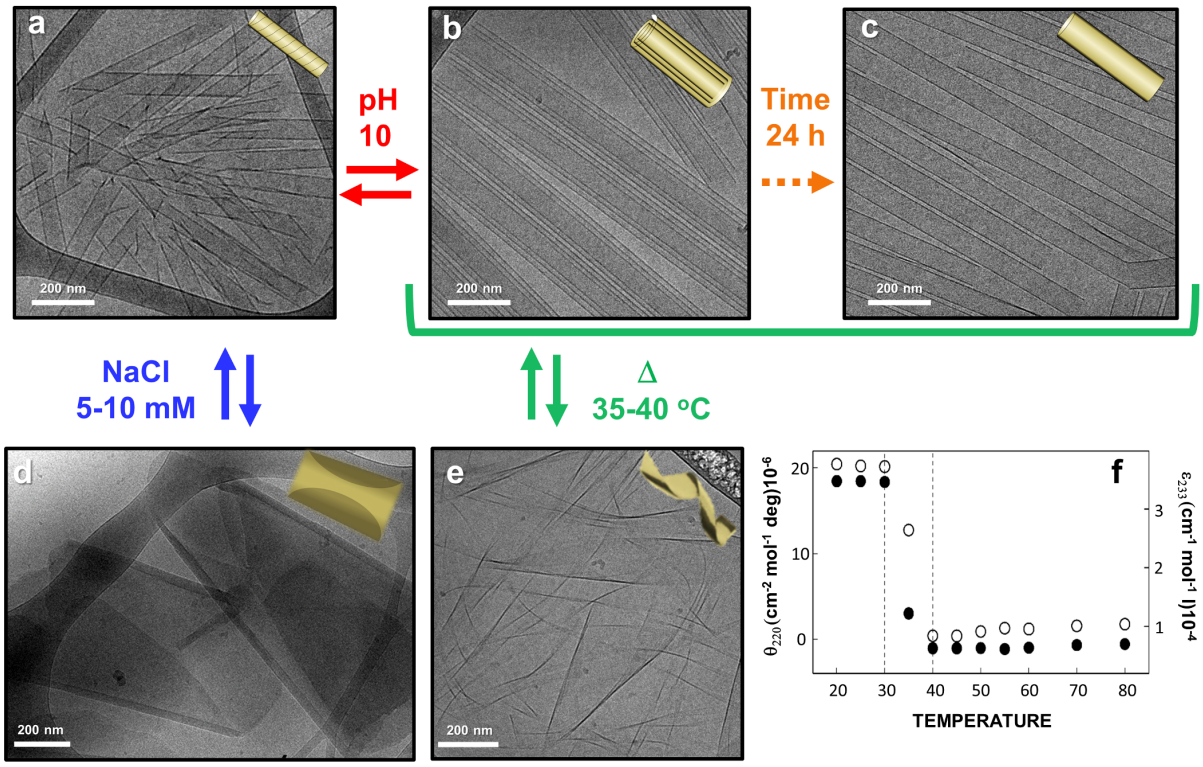

Figure 1.12. HNaphC supramolecular aggregates induced by different experimental conditions: single-walled tubules (a), multi walled tubules (b), long single walled tubules (c), folded bilayers (d), and twisted ribbons (e). Reported molar eliptixity and extinction coefficient values extracted at λ_{220} for a 1 mM HNaphC solution as a function of temperature. A full description of the behavior studied until now can be found in references [70] and [78]. Adapted with permission from di Gregorio, M. C.; Travaglini, L.; Del Giudice, A.; Cautela, J.; Pavel, N. V.; Galantini, L. Langmuir **2018**, acs.langmuir.8b02657. Copyright (2018) American Chemical Society.

Since the aim of this study was to obtain a roughly monodisperse population of multi-walled tubular aggregates, it was decided to work only with fresh (within 24 h after preparation) HNaphC solution samples, keeping the pH at 11.5. The pH value was monitored and in case adjusted adding few microliters of a 0.1 M NaOH filtered solution prepared in milliQ water, to avoid pH lowering due to CO_2 solubilization. The kinetics of formation was controlled qualitatively using the transmission channel of the CLSM (Figure 1.13). Beside the rather low resolution, was possible to appreciate the slow kinetics of the tubular structures evolution from multi-walled tubules 4μm long (Figure 1.13a) to very long single-walled tubules (Figure 1.13c). Each specimen came from a 2mM solution at pH 11.50 and a drop of the sample was analyzed freshly prepared, after 2 h, 3 d and 7 d, unveiling the kinetics of the structural changes of the aggregates. Since the lateral resolution was typical of an optical microscope having a x100x1.4NA objective, *i.e.* around 150 nm, no structural details could be observed. A higher magnification micrograph was captured and reported in Figure 1.13a but the reduced thickness and length of the aggregates made the tubular structures harder to image properly.

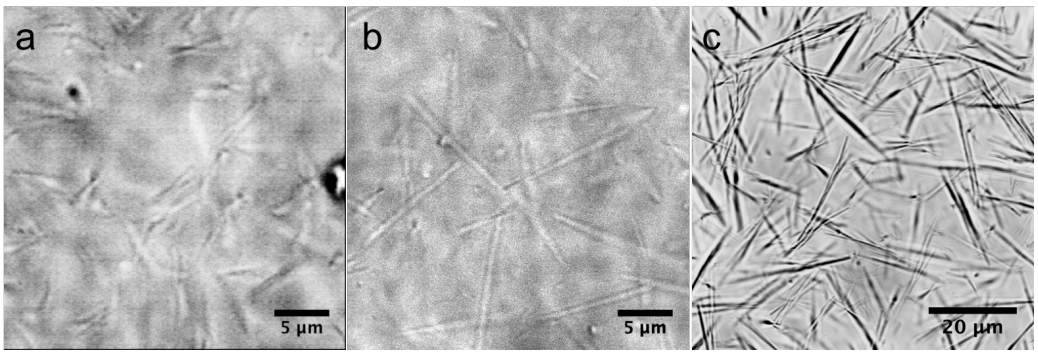

Figure 1.13. CSLM micrographs of 2mM HNaphC supramolecular tubules at pH 11.50 and 20°C taken through the transmission mode of the microscope at different times from sample preparation: 2 h (a), 76 h (b), 7 days (c).

To investigate the tubules features cryo-TEM microscopy was performed respectively on a 2mM solution of 12 h old and 3 days old HNaphC at pH 11.5. The specimen was prepared each time blotting the sample from behind and then freezing it quickly in liquid ethane trough an automatic blotting instrument. Then, it was stored in liquid nitrogen and examined after few minutes. The images obtained are represented below (Figure 1.14). Tubular structures have lengths around 5-6 μm in the just prepared sample. After 12 h, growth of the structures was already triggered highlighting the presence of a population of tubular structures with lengths up to 10-15μm, outside the wide range of the lowest magnification accessible to the instrument. At very high magnifications, images show that the multi-walled tubules have a clear double-scroll structure having 3-4 layers each. Since these tubules are basically formed in couples, each tubule of each couple has a similar number of layers and, interestingly, at high number densities, it was observed also through CSLM a certain tendency to associate forming arrays of tubules aligned in parallel. To have an idea of the diameter and of the number of layers for a single tubule, starting from the cryo-TEM images, was possible to record the transmission profile along a line lying perpendicular to the tubules longitudinal axis and then average it on the whole length of the tubules to increase statistics (Figure 1.15). The spacing within the layers seems to be fixed at 10 – 12 nm ± 2 nm ca. These result are in agreement with the spacing among the tubular scrolled layers deriving from previous SAXS measurements,[78] where a value between 10 and 15 nm was found. The tips of the scrolls are formed by the edges of the supramolecular rolled sheets. Sometimes irregularities in the molecular arrangement can be found, causing fractures, deformations and, seldom, the presence of anomalies, probably exposing locally disordered supramolecular domains towards the solvent.

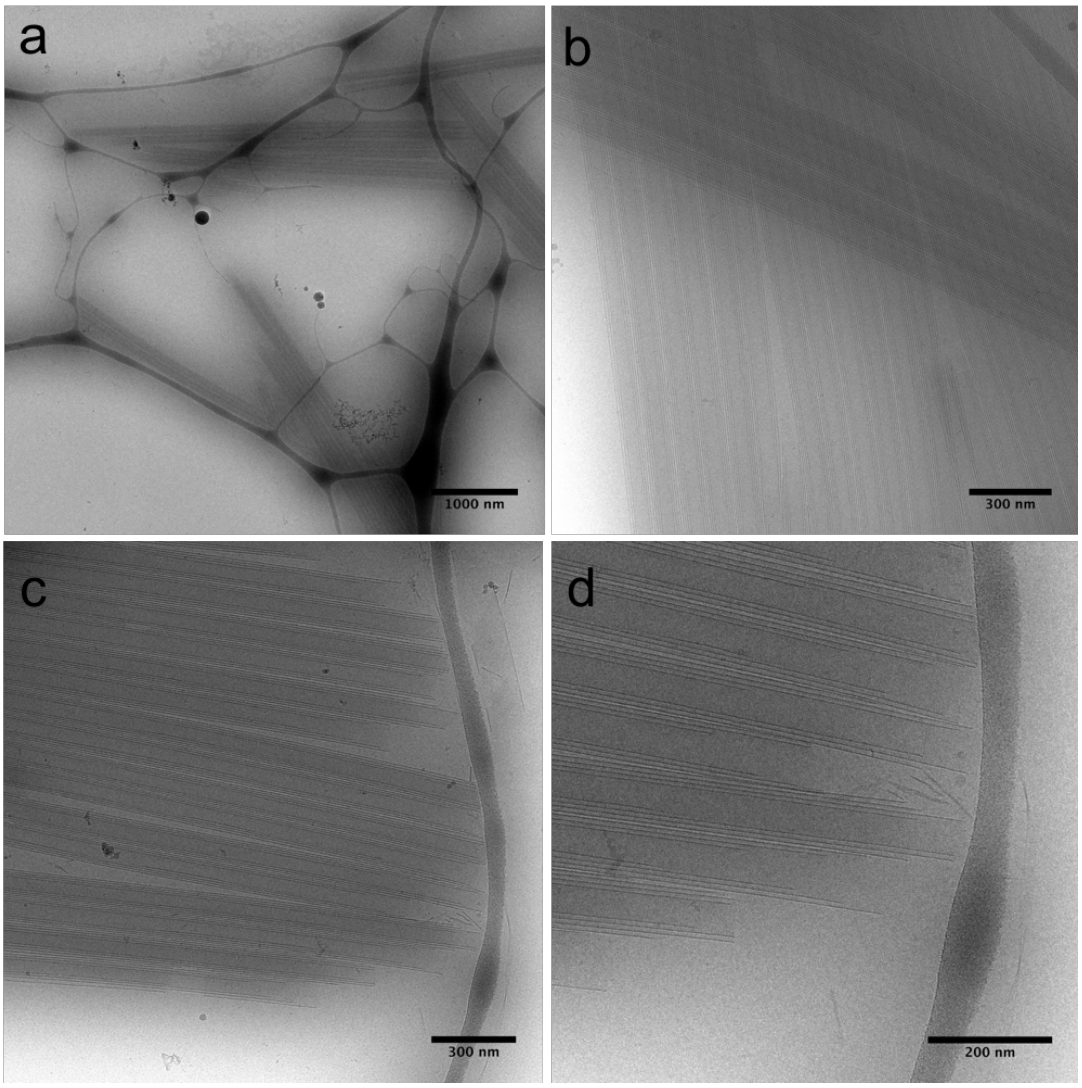

Figure 1.14. Cryo-TEM micrographs at different magnification of HNaphC multi-walled tubules at 5h from preparation at pH 11.47 and T=20°C.

Moreover, since the initial layer can scroll exposing or not the rim towards the solvent, it is likely to find both telescopic or flared tips, detail that was not discovered in the past studies on the same aggregates. As will be demonstrated further in the text, reasonably, this kind of edges help the interaction with a spherical particle, since make possible for it to dwell easily, maximizing the points of contact with the tubular tip. Surprisingly, no big changes were observed after 3 days (Figure 1.15b). It could only be visible how scrolls, undergo gradually a decrease of the number of the overlapped layers and an increase of both internal and external diameters. In particular, an increase of the internal channel of the tubules from 45 to 55 nm was observed.

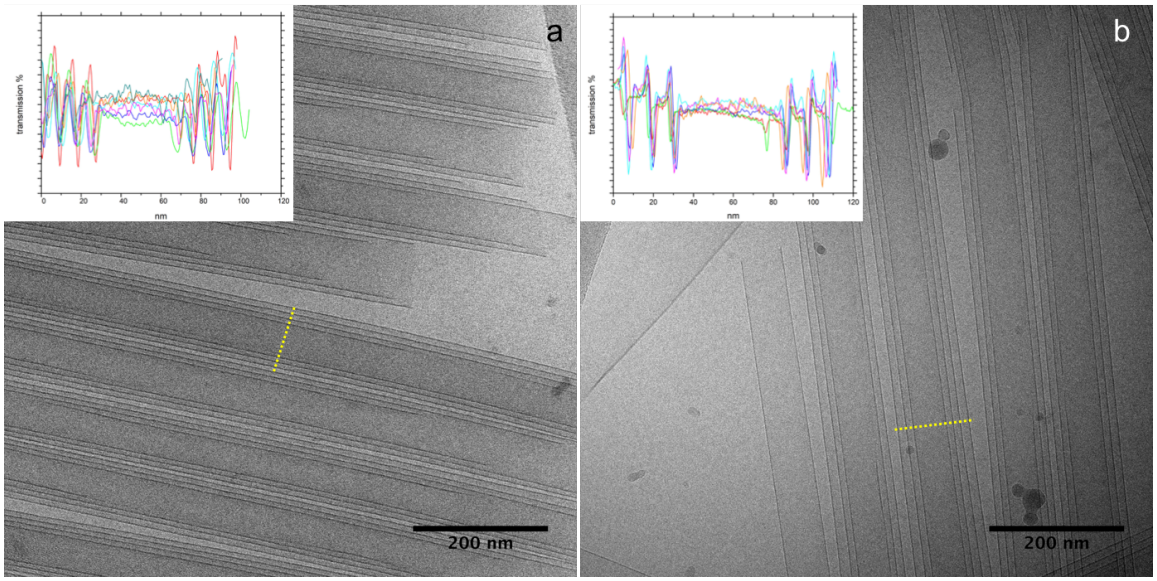

Figure 1.15. Transmission profiles (inset) extracted from elaboration of HNaphC 2mM pH 11.47 cryo-TEM micrographs.

1.6.2 PNIPAM microgels and PS/PNIPAM or PS/PNIPMAM core-shell particles

Interaction of the tubules with different types of polymeric particles was tested. Crosslinked (crosslinking degree 5%) poly(N-isopropylacylamide) (PNIPAM) microgels or composite core – shell with polystyrene (PS) core and PNIPAM or poly(N-isopropylmethacrylamide) (PNIPMAM) shell particles were used for the experiments reported in these paragraphs. Synthesis of the particles was already reported in a previous published work.[98] CSLM measurements were performed at 20°C where they are proven to be in the swollen and not collapsed state. Since confocal microscopy takes advantage of fluorescence for the imaging, the particles were synthesized labeled with tetramethylrhodamine TRITC (red) or fluorescein isothiocyanate FITC (green). Transmission electron microscopy (TEM) allowed to prove the low polydispersity of sizes of core particles as confirmed from the radii average determination which was centered at 267 ± 20 nm for the anionic core and 232 ± 13nm for the cationic core particles as well as the low polydispersity of the final microgels particles (Figure 1.17). DLS measurements were then performed at 20°C as complementary characterization of the low polydispersity in swollen state (Figures 1.16) giving results consistent with previous data obtained through crystallization at higher concentrations.[99] In the following table are reported the principal values for the hydrodynamic radius (R_H), type of charge (cationic/anionic),

electrophoretic mobility (μ) and apparent charge $Q_{app}= 6\pi\eta R_H\mu$ (where η is viscosity) (Table 1.2).

Name	***M+***	***CSM+***	***CSM−***
Composition	PNIPAM	PS/PNIPAM	PS/PNIPMAM
Charge	Cationic	Cationic	Anionic
Fluorophore	Rhodamine	Fluoresceine	Rhodamine
Core radius[1] [nm]		232	267
R_H(20°C) [nm]	299	401	528
μ(20°C) [$10^{-8}m^2/Vs$]	0.58	+1.72	-1.86
Q_{app} le-l	204	813	1157

[1]Estimated by TEM analysis.

Table 1.2. Acronyms and main characteristics of the microgels particles. R_H, μ and Q_{app} refer to the hydrodynamic radius, electrophoretic mobility and apparent charge of the different systems, respectively.

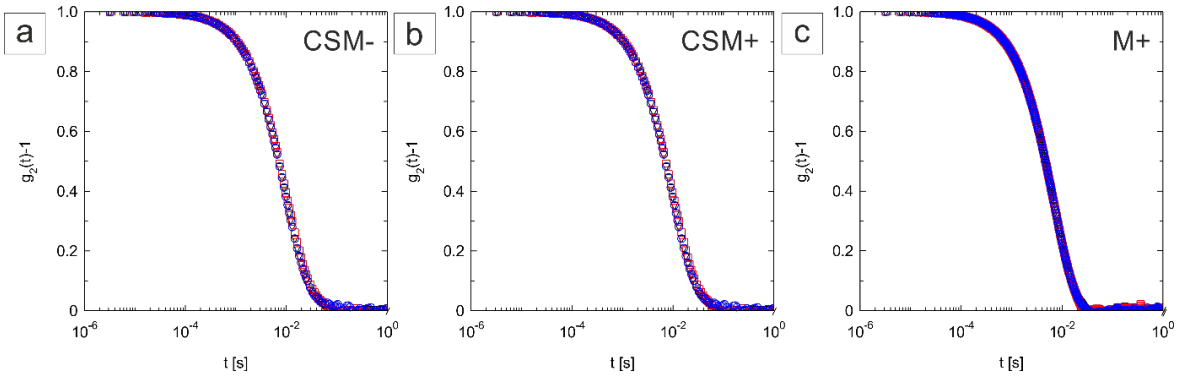

Figure 1.16. DLS time correlation functions of dilute solution of the polymeric microgels at 20°C in pure water. Adapted with permission from Ref 98. Copyright 2018 Wiley-VCH.

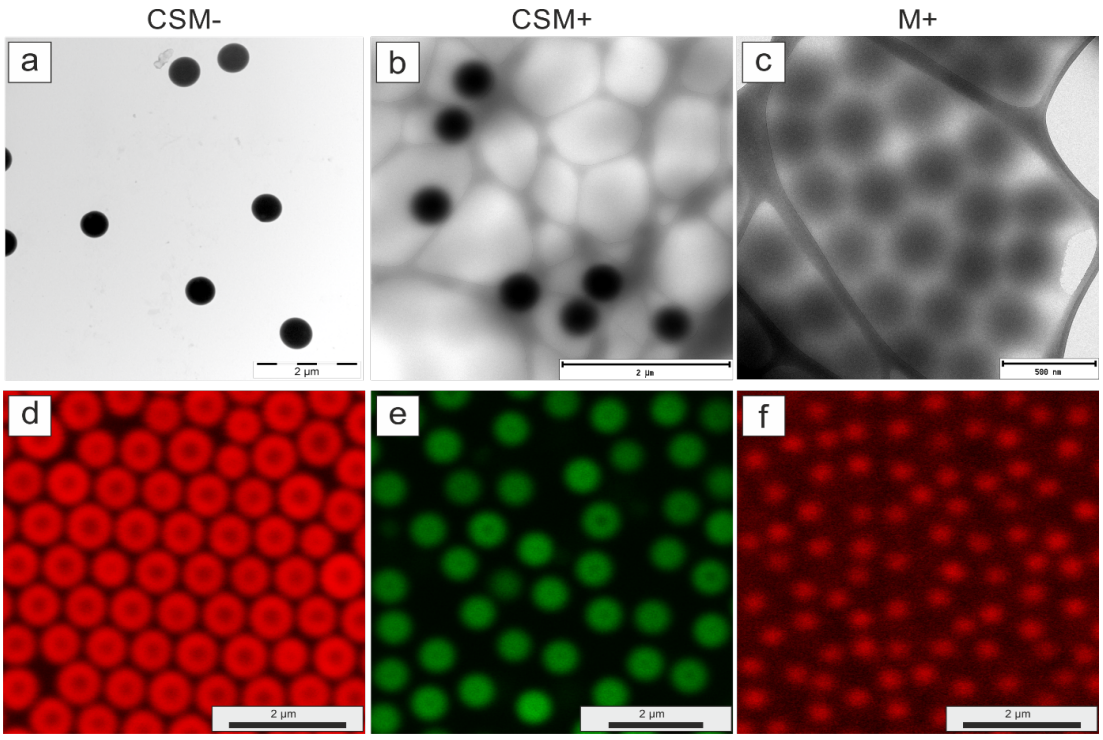

Figure 1.17. TEM (a, b and c) and CSLM (d, e and f) of the spherical polymeric particles. Adapted with permission from ref 98. Copyright 2018 Wiley-VCH.

2 Chapter 2 Hierarchical co-assemblies of ACD/CCD catanionic mixtures supramolecular tubules and polymeric particles

2.1 Chapter rationale

BSD supramolecular tubules present very peculiar features mainly regarding the fine control over their charge and structure. Control over both the charge and supramolecular structure can be imparted tuning easily the self-assembly conditions in either pure and catanionic mixtures solutions. This made these nanostructures eligible anisotropic building blocks in the context of the preparation of hierarchical co-assembled mixed systems formed through interaction with spherical microgel particles. In this light, the aim of this first basic part of the whole study was to test the ability of these tubules to work as colloidal linkers and templating surfaces through which build supracolloidal frameworks. As will be deeply described in the dissertation, rather high specificity of interaction occurred when these structures interacted with polymeric PNIPMAM or PNIPAM fluorescently labeled microgels. This specificity is intimately related to the discontinuities on the tubular surface as will be demonstrated further. With respect to this, one of the main findings consists in the presence of two differently interactive binding sites on tubular surface. Specifically, these two binding sites were observed to be the tip of the tubule and the rim on the longitudinal axis of its external surface, deriving from the peculiar type of folding described in the previous section. Independently from the tubular overall charge and surface features these sites seemed to be always characterized by different interaction strengths, so that particles tended to bind to them in a well precise order, dictated by charge *in primis,* and secondarily by the ratio between the radius of the microgel $R_{\mu gel}$ and the radius of the tubule R_{tubule}. With respect to interaction mechanism the electrostatic driving force gives an essential key to understand its nature, which is only partially addressable to opposite charges interplay. In facts, more than one experimental evidence pushes to take into account more complex phenomena like van der Waals interaction, hydrophobic effect and counter-ions release contribution to the entropic balance. Since primary interest was to test the influence of the electrostatic interactions imparted by the tubules charge ratio on the specific kind of supracolloidal assembly, the association between preformed catanionic tubules of different composition and charged polymeric particles was investigated. For this purpose, the association experiments are herein presented as a function of the tubular aggregate composition with decreasing X_{ACD}, starting with pure preformed anionic aggregates ($X_{ACD} = 1$) in 30 mM sodium

$Na_2CO_3/NaHCO_3$ buffer and followed by catanionic aggregates with X_{ACD} =0.7, 0.4 and 0.2 prepared in pure water. In the description, the terms "tubular aggregates", "tubules" and "scrolls" are used to identify the surfactant aggregates independently of their detailed architecture.

2.2 Co-assemblies of variable X_{ACD} tubules and polymeric microgels

2.2.1 Positively charged CSM+ microgels and negatively charged ACD tubules (X_{ACD} = 1)

Assemblies deriving from an addition of cationic core-shell CSM+ particles to an excess of ACD negatively charged tubules was observed to be characterized by very specific adsorption of the tubular extremities on the spherical particle surface. This adsorption had as a result the formation of core-corona assemblies resembling icosahedral viruses, having a polymeric core and a radial association of tubules in the corona (Figure 2.1a-c). As proven through CSLM, the core-corona assemblies were rather stable in full Brownian motion in solution thanks to the high efficiency of tubule binding site, whom characteristics will be investigated further in this work. Although the dynamic exchange between tubules adsorbed on the microgels polymeric surface and tubules in the bulk could not be followed by any means but indeed a certain ability of the tubules to diffuse and to pack at the microgels surface was visible. This suggests how the specific adsorption has basically enough strength to keep the assembly compact and stable but at the same time is sufficiently weak to provide the mobility tubules need to organize efficiently at the particle surface. As the formation of these core-corona assemblies was way more favored in respect to homogeneous bi-functionalization of both tubular extremities and no dumbbell were ever observed during the assembly process, seems legit to think that one extremity has an interaction potential more favored than the other, effect that could be related to the chiral packing of BSD molecules along the scrolled bilayer. Furthermore, adding M+ microgels to the core-corona assemblies already formed and stable in their dispersion a preferential interaction with the free extremities was observed, bringing to the formation of a peripheral distribution of equally spaced M+ microgels from the singular CSM+ core-particle (Figure 2.1d-f). After one day, the co-presence of fibrils with the tubules induced depletion (a similar effect was observed to be induced by wormlike micelles on other type of spherical colloidal particles)[100–102] of these

complexes, packing the assemblies in hierarchical clusters with respect to two different length scales imposed respectively by the larger particles (forced at long distance each other) and by the small particles (distributed peripherally) were the spacing is dictated by the tubular linker length (Figure 2.1d-k). The hierarchical organization of the two microgels was confirmed by the evaluation of 2D pair distribution functions between *CSM+*, *M+* and both particles (see Figure 2.2).

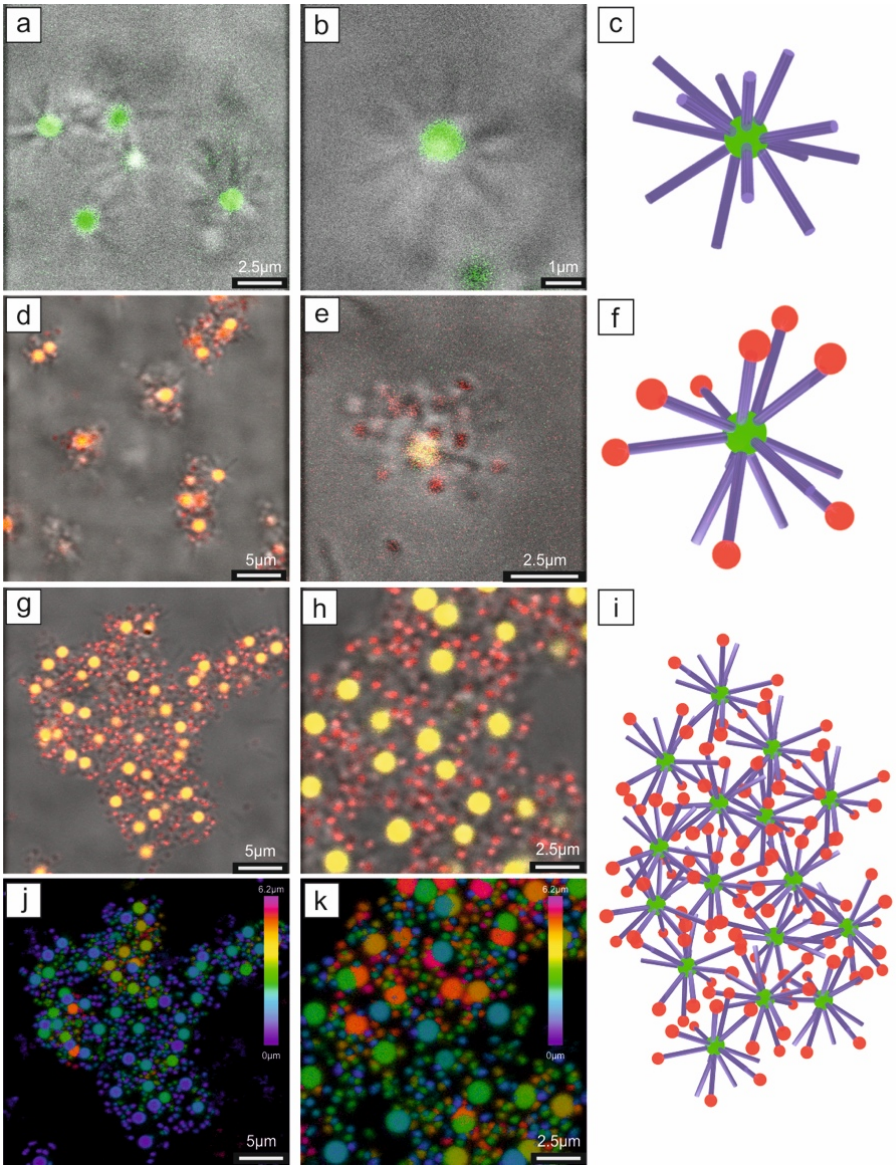

Figure 2.1. Specific association of ACD preformed tubules with cationic core-shell particles CSM+ and homogeneous microgels M+ in Na_2CO_3/$NaHCO_3$ buffer (30 mM) at 20°C. a, b: Combination of transmission and fluorescence imaging core-corona particles formed by self-assembly of ACD tubes (1.8 mM) and CSM+ microgels labeled in green (0.026 wt%). d, e, g, h, j, k: Complex assemblies observed by adding cationic M+ microgels labeled in red to preassembled CSM+ and ACD tubules (final concentration 1.6 mM ACD, 0.024 wt% CSM+, 0.045 wt% M+) imaged within 1 h. (d, e) and after one day (g, h, j, k). Combined transmission and fluorescence CLSM micrographs shown in d-e panels allow the clear determination of the M+ microgels in the periphery of the core-shell CSM+ microgels and their connection via microtubules. After 1 day the assemblies form a network defined by different length scale provided by the specific association between the particles and the microtubules. j, k illustrate the 3D localization of the labeled particles within the assemblies (color-coded as a function of the relative z in the xyz-stack). (c, f, i) Schematics of the different assemblies between the tubules and microgels. Adapted with permission from Ref 98. Copyright 2018 Wiley-VCH.

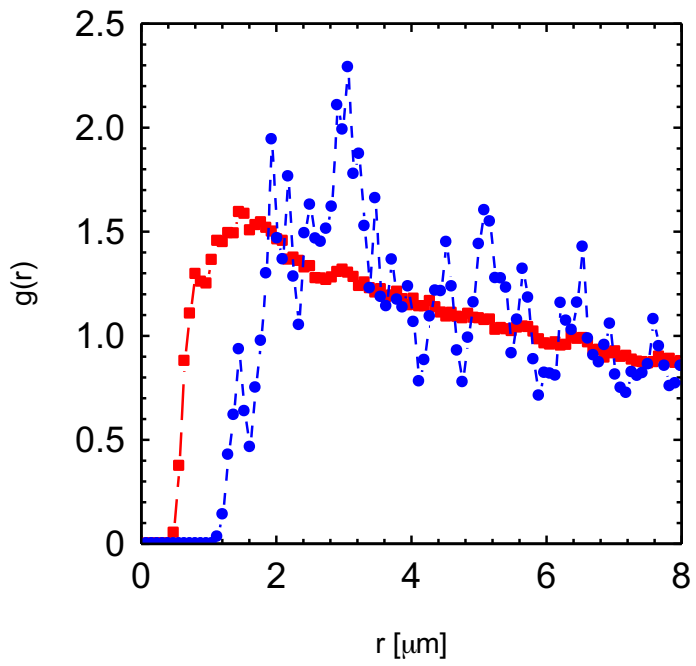

Figure 2.2. 2D *g(r)s* of the assemblies between preassembled *CSM+* microgels and *ACD* tubes after addition of *M+* microgels recorded after 1 day shown in Figure 2.1g-l. The solid dot symbols refer to the *CSM+ g(r)* showing a maximum around 3 μm in the order of the tubule length. The solid square symbols correspond to the *g(r)* considering both *M+* and *CSM+*. Hereby, the first maximum lays around 1.5 μm, which distance is much larger than the *M+* diameter, thus demonstrating that both microgels are maintained apart due to their assembly with the tubules. Adapted with permission from Ref 98. Copyright 2018 Wiley-VCH.

2.2.2 Positively charged CSM+ particles and ACD/CCD negatively charged tubules (X_{ACD} = 0.7)

When preformed tubules prepared in catanionic ACD/CCD mixtures having X_{ACD}=0.7 are mixed with CSM+ microgels at very low particle weight fraction (or particle/tubule numerical ratio), interestingly core-corona assemblies form again (Figure 2.3a-c), like in the previous case. Besides, in this case interaction seemed to be less efficient probably because of the increased tubular length and cross sectional diameter polydispersity, making the packing of the tubules on the CSM+ surface a process rather difficult to afford. Upon an increase of the particle fraction ($c_{\mu gel} \geq 0.013$ wt%), a decrease of tubules adsorbed per particle was observed. As consequence, progressive entanglement of core-corona units brought to the formation of clustered networks where particles were interconnected through tubular linkers (Figure 2.3b) exhibiting a number density of the particles proportional to $c_{\mu gel}$. The resulting supracolloidal networks presented an extremely low density in the order of 6.10^{-4} g/cm^3 (for $c_{\mu gel}$ = 0.013 wt% and c_{tub} = 0.8 mM) and thus demonstrated an interesting approach for the formation of low

density hybrid supramolecular-supracolloidal materials. Further increase of $c_{\mu gel}$ to 0.026 wt%, resulted in a secondary adsorption of the microgels at the sides of the tubules. Worthwhile noting was the absence of association in mixtures with *CSM-* confirming the important contribution of electrostatic interactions in the assembly (experimental data can be found in Ref. 98).

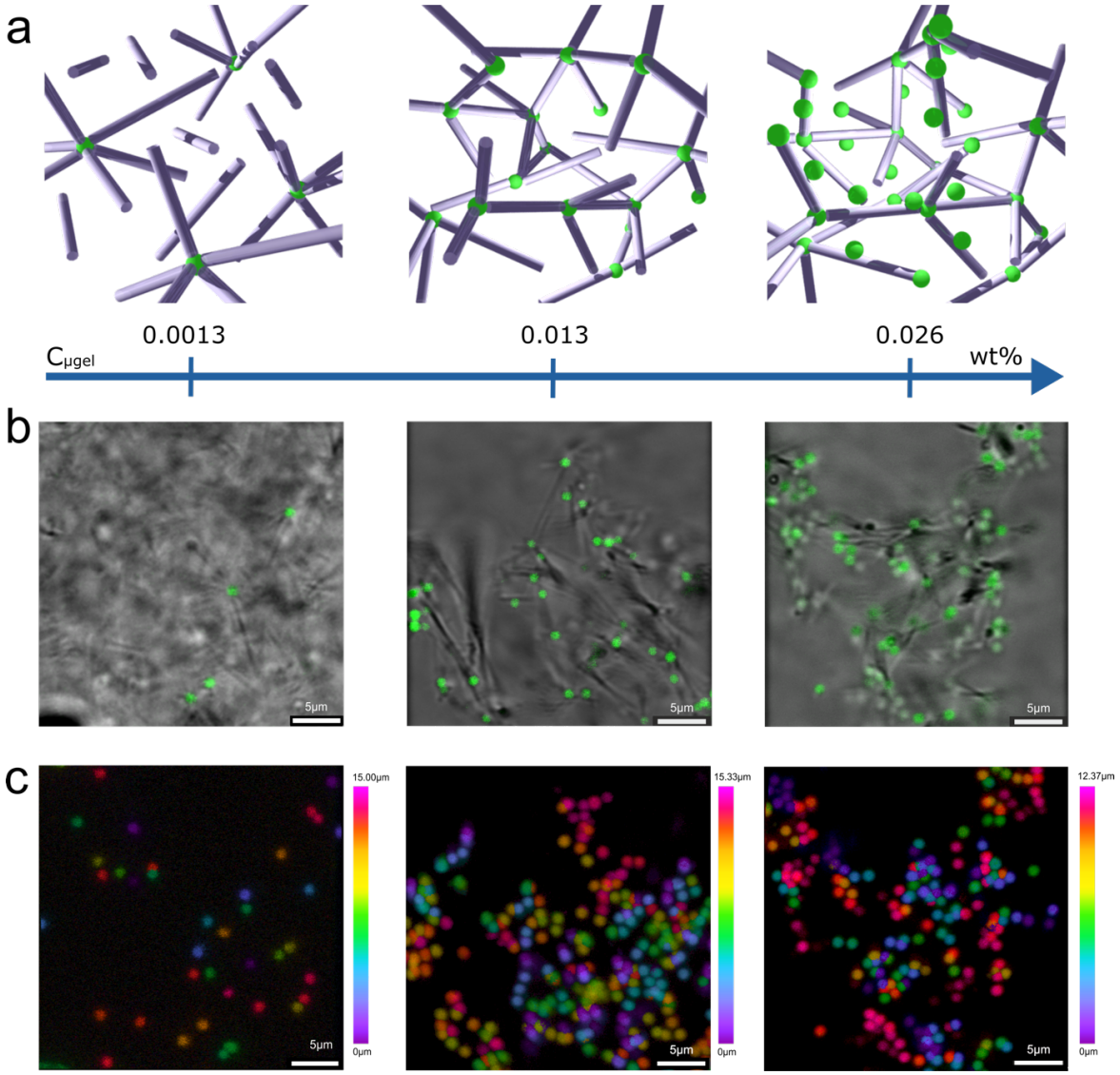

Figure 2.3. Assembly of cationic CSM+ with large negative tubular aggregates (X_{ACD} = 0.7). a: Schematic representation of the assembly with increasing $c_{\mu gel}$ at constant tubule concentration. b, c: The influence of the colloidal linker concentration $c_{\mu gel}$ on the assembly with large microtubules (0.8 mM) was imaged by CLSM at 20°C (from the left to the right with $c_{\mu gel}$ = 0.0013, 0.013 and 0.026 wt%. The superposition of 2D transmission and fluorescent CLSM micrographs is shown in b and the 3D localization of the linker is presented in c (color code indicates the relative z position in the xyz stack). Scale bars: 5 μm. Adapted with permission from Ref 98. Copyright 2018 Wiley-VCH.

2.2.3 Positively charged CSM+ microgels -ACD/CCD neutral and positively charged tubules (X_{ACD} = 0.4 and 0.2)

Weakening of electrostatic attractive component to the overall interaction potential was possible by decreasing the X_{ACD} ratio of the catanionic mixture from 0.7 to 0.4 and 0.2 obtaining respectively almost neutral and slightly positive tubules. Under these conditions when preformed tubules were mixed with CSM+ microgels only partial co-assembly was arising in terms of branched clusters or few tubular aggregates interconnecting microgels particles. Since the fraction of free microgels was rather high, no large network was formed as shown in Figure 2.4, as no enough entanglement points were available for the network to form. Remarkably, increasing microgels concentration up to 0.026 wt% the association was favored again towards tubular extremities, while almost no secondary adsorption at the sides of the tubules could be noticed. Clearly, since the charge ratio was near 1 and the aggregates were neutral or with a slight positive charge, low electrostatic interactions or repulsive interaction were taking place implying that overall interaction mechanism was relying on other contributions. Van der Waals or hydrophobic effect as well as counter-ions release must be invoked to explain such a specific but nevertheless weak particle binding.

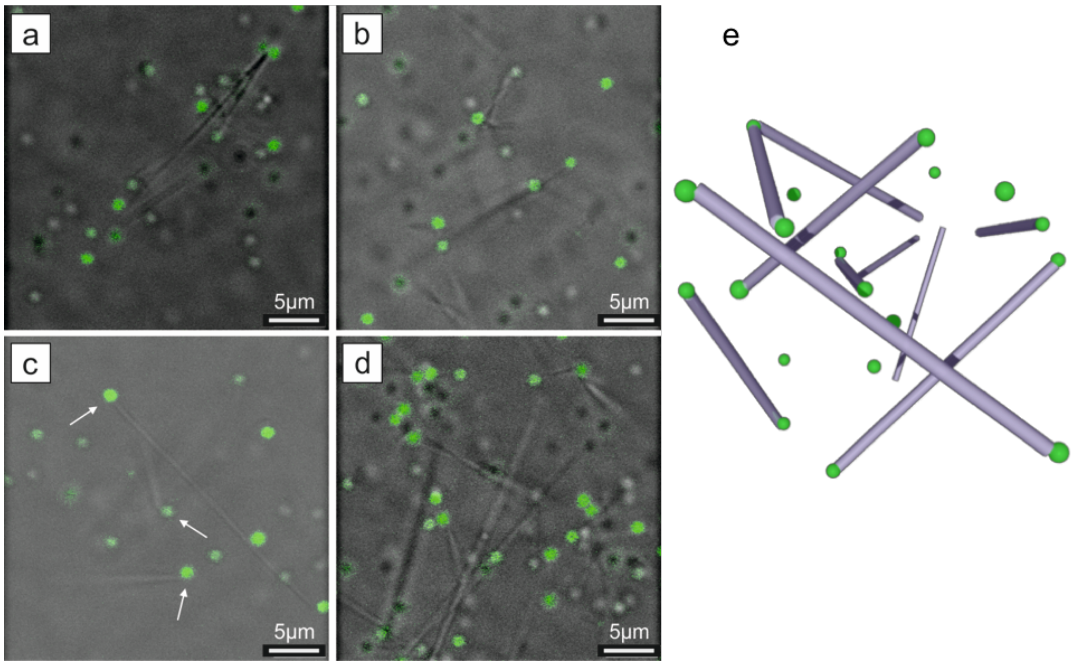

Figure 2.4. Assembly of cationic core-shell microgels CSM+ with neutral and positive catanionic tubules. The assembly is imaged by combining transmission and fluorescent CLSM modes for a mixture of cationic microgels (0.026 wt%) with neutral tubules in a and b (X_{ACD} = 0.4, total surfactant concentration 0.8 mM) and with positive tubules in c and d (X_{ACD} = 0.2, total surfactant concentration 0.8 mM). A specific adsorption of the microgels to the extremities of the tubular aggregates was observed (as shown by the arrows in c) whereas no large network formation occurred in both mixtures. Adapted with permission from Ref 98. Copyright 2018 Wiley-VCH.

2.2.4 Negatively charged CSM- microgels -ACD/CCD neutral and positively charged catanionic tubules (X_{ACD} = 0.4 and 0.2)

Dispersions of X_{ACD} = 0.2 tubules mixed with anionic CSM- microgels were investigated to test the response of the system when tubular charge was strongly unbalanced towards positive values. At low anionic core-shell microgels concentration ($c_{\mu gel}$ = 0.01 wt%) a lower selectivity of interaction with tubular extremities it's been observed. Still, a relevant amount of microgels was adsorbed on tubular surface (Figure 2.5a-b) mostly at equal intervals probably in correspondence of the rim profile as reported by the model represented in Figure 2.6c or helically aligned following the rim of tubules like in scheme reported in Figure 2.6f. In the micrograph reported in Figure 2.5c is possible to see how attached particles were exploiting the binding sites of the tubules, and hence their linking ability, to form full-spanning networks with very low density in terms of microgels weight percent and total surfactant concentration.

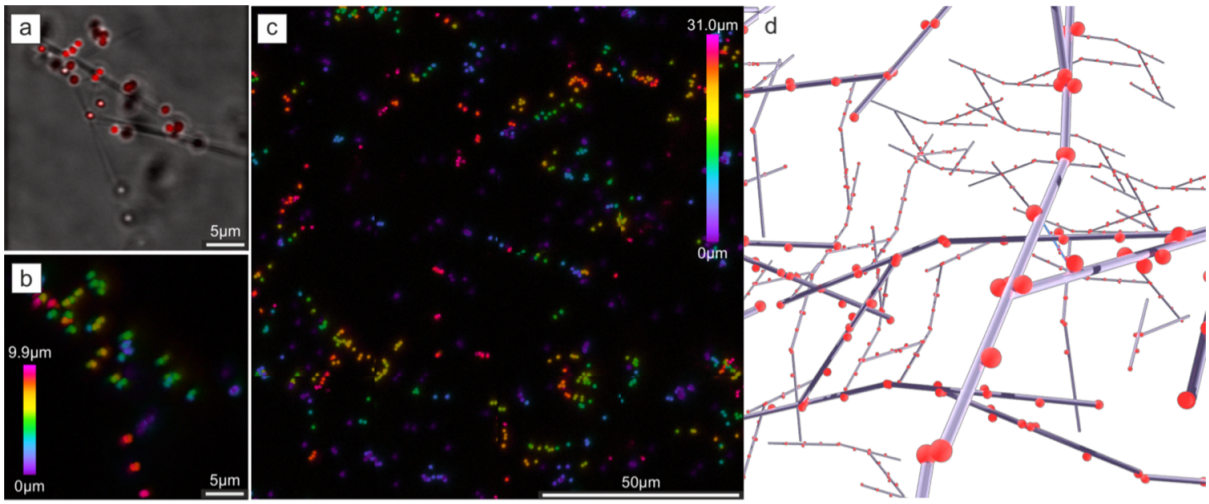

Figure 2.5. Assembly of anionic CSM– particles with slightly positive tubules in a large full-spanning network. A small amount of anionic core-shell microgels (0.01 wt%) was associated with positive scrolls (X_{ACD} = 0.2, total surfactant concentration 0.8 mM). The association was imaged by a combination of transmission and fluorescence CLSM to demonstrate the discrete regular presence of contact points in a together with the corresponding 3D assembly of the microgels color coded as a function of their relative position in *z* shown in b. A low density full-spanning network was observed at such concentration illustrated by the localization of the microgels in 3D shown in c. Adapted with permission from Ref 98. Copyright 2018 Wiley-VCH.

When the fraction of *CSM–* was increased, separated tubules fully decorated by microgels could be observed (Figure 2.6). Under these conditions, the microgels appeared to preferentially interact with the outer rims of the scrolled supramolecular sheet forming the tubular aggregates. Therefore, the microgels not only decorated the extremities of the tubules but also adsorbed along the accessible rim of the rolled sheet forming oppositely handed helical arrangements. The latter could present different pitches, with an order of magnitude ranging from one micron

(Figure 2.6a,b) to tenths (Figure 2.6d,e) of microns. The scrolls with shortest pitches looked almost fully covered by microgels when imaged by CLSM. Surprisingly, *CSM*- microgels were found to strongly interact with the almost neutral (X_{ACD} = 0.4, Figure 2.6d, e) and slightly positive tubules. This observation was ascribed to the different affinities of the bile salt derivative counterions, as discussed in more details in the following section.

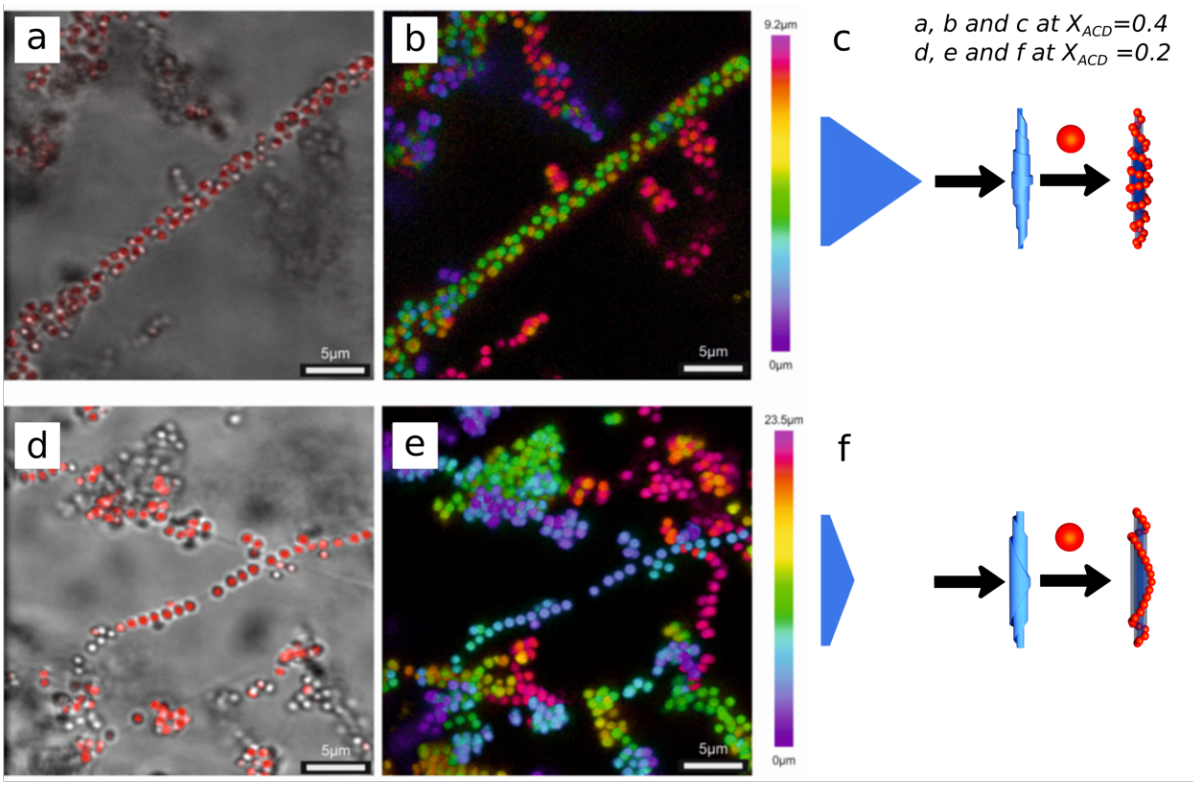

Figure 2.6. Assembly of anionic CSM- core-shell microgels with large neutral or slightly positive tubules. The assembly is imaged by CLSM for a CSM- mixture (0.1 wt%) with either almost neutral tubules (X_{ACD} = 0.4, 0.8 mM) (a, b) or slightly positive tubules (X_{ACD} = 0.2, 0.8 mM) (d, e) at 20°C in milliQ water. The microgels decorate the rims of the supramolecular sheets forming the tubules up to a full decoration and partially stabilized some of the assemblies. Different pitches, with an order of magnitude ranging from one micron (a, b) to tenths (d, e) of microns are formed depending on the shape of the triangular sheet forming the tubules according to the schemes shown in c and f. a, d Superposition of 2D transmission and fluorescence z-stack snapshots of the decorated tubules. b, e Corresponding 3D reconstructions of the fluorescent micrographs where the microgels are color-coded as a function of their relative position in z. Adapted with permission from Ref 98. Copyright 2018 Wiley-VCH.

When the microgels weight fraction is increased and decoration is triggered, the network previously established (see Figure 2.5c) persists, because of the strong interconnections among decorated tubules as show in the following figure.

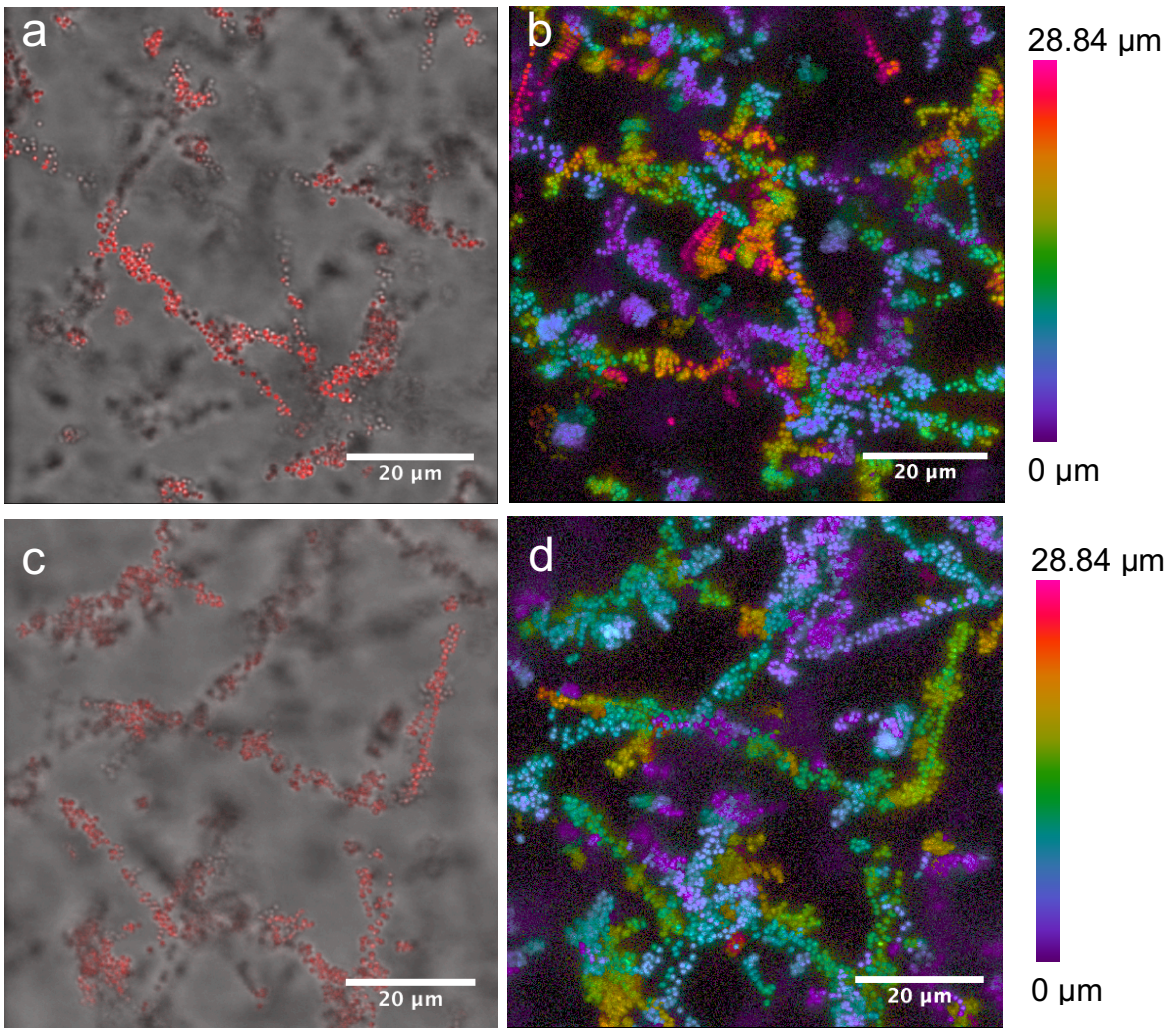

Figure 2.7. Combination of fluorescence and transmission CSLM modes (a , c) and corresponding orthogonal reconstruction of color-coded *z*-stacks related to the same detection volume (c, d) of a mixture of X_{ACD} = 0.2 and anionic core-shell CSM-microgels (0.1wt%). When the strong interaction occurs no free microgels are visible and the tubules are stuck in the same xyz coordinates. The part of the network imaged is 77.7μmx77.5μmx60μm.

2.3 Discussion

As proven by the results, a specific interaction occurred when spherical microgels particles were mixed with ACD dispersion of tubular aggregates coming from pure ACD solutions, as well as in ACD/CCD catanionic mixtures, at variable X_{ACD} ratio. Different tubular interaction sites could be chosen depending on the fine tuning of experimental conditions like X_{ACD} ratio, buffer concentration, total surfactant concentration c_{tot}, particle/tubule number ratio. One of the most important aspects is that the strongest interaction occurred where the two species, the microgels and the tubules, were oppositely charged. When this condition was verified the microgels showed a very high reactivity to the tubular binding sites either in the case of ACD

buffered solutions and in ACD/CCD catanionic mixtures in pure water (Figure 2.1 and Figure 2.3a), with the formation of core-corona particles at low microgels weight fractions. With respect to the systems where catanionic mixtures were employed, the interaction could be directed to different supracolloidal co-assemblies by controlling the microgels/tubule number ratio. By progressively increasing such a ratio, the formation of low-density supracolloidal-supramolecular networks of microgels interconnected with tubules by their extremities was observed (Figure 2.3b). In several samples an excess of microgels in respect to tubules, the formation of tubular structures helically decorated by microgels was obtained, as a consequence of the preferential adsorption of the microgels to the free rim of the rolled supramolecular sheet as shown by Figure 2.6. In fact, the positively charged scrolls were particularly prone to helical decoration since microgels were efficiently directed towards the oppositely handed helical rim, due to the convenient sizes proportion between the curved spherical surface and the tubular discontinuity represented by the scrolled bilayer interruption on the tubular surface. Moreover, electrostatic interactions between the positive tubules and the anionic microgels played a fundamental role. The interaction became much weaker with cationic microgels when neutral or slightly positive catanionic scrolls were used, as only a few microgels were observed to bind to the scrolls, again, mainly at their extremities (Figure 2.4).

The nature of the intricate mechanism of such interactions is rather hard to investigate and to deeply understand. Besides, the experiments results drove to two relevant conclusions. The first one concerns how the tubular architecture directs the co-assembly with the microgels particle. As the incremental number density of microgels rises, the steps of the co-assembly pathway seemed to be always the same, starting from core-corona assemblies, passing through network or clusters formation, and finally arriving to decoration. This observation implies that binding sites are basically of two types and have well precise order imposed by different strength of the interaction potential, somehow related not only to the residual charge distribution on the tubular structure, but also to their geometry and morphology of the folded supramolecular bilayer. Specifically, the tubular extremities are the first binding site while the second is represented by the external rim on tubules outer surface. Furthermore, a predominance of electrostatic contribution on the overall interaction mechanism is clearly visible and must be taken into account as crucially affecting the co-assembly formation. However, other contributions need to be included not as marginal factors but, in turn, fundamental, to explain some verified interaction between neutral tubules and cationic microgels or even with slightly positive microgels.

As already mentioned the release of counterions and its effect on entropy gain constitutes an additional term to the interaction general mechanism. Focusing on negative or positive catanionic mixtures with oppositely charged microgels, the assumption that the scrolled bilayers are composed by a homogeneous distribution of charged heads supports the conclusion that interaction strengthens for larger contact areas. That means that primary-secondary binding site stability order could be justified by a purely electrostatically driven interaction model considering a larger contact area of the tubular extremity with respect to the longitudinal outer surface discontinuity of the tubule. Moreover, during the interaction with the tubular extremities microgels could approach the scrolled tubular rim exploiting small distorsions of the scroll to adapt the tubule extremity to the spherical convex structure of the microgels maximizing and optimizing the interaction efficiency. As already mentioned the secondary binding site having intermediate stability was the tubular outer surface discontinuity represented by the helical rim along the tubule. Finally, the weakest interaction indeed was offered by smooth surfaces where contact area was basically minimized and so was electrostatic interaction between the charges of the two species. Accordingly, a lesser interaction was expected at the smooth external surface of the tubules. Interestingly, *CSM-* microgels were found to strongly interact with neutral tubules (X_{ACD} = 0.4). In this case a further assumption has to be made. CCD is bound with an iodide counter-ion having a stronger affinity with the CCD molecule with respect to the one of sodium with the ACD molecule. Therefore, even if the net charge of the tubules was supposed to be positive considering its composition, dielectrophoretic measurements proved that it was slightly negative. Besides, counter-ion release upon adsorption of the microgels could be mainly responsible for such an assembly. We hypothesized that the additional contribution to the interaction between microgels and tubules was related to specific features of the supramolecular sheet at the edges, that further supported the observed selective interactions. Indeed, if a typical bilayer structure was assumed for the rolled supramolecular sheet, more hydrophobic molecular moieties in contact with water were expected at the edges with respect to the surface and an interaction with microgels could be promoted to reduce the surface energy. As the extremities offered a larger area of accessible edges than the rims along the tubules this contribution to the interaction confirmed the stability order of the selective binding. The observed selective interaction of the cationic microgels with the extremities of uncharged or slightly positive tubules confirmed that this contribution to the interaction is not negligible. Previous reports emphasized the interactions between microgels and zwitterionic lipid bilayer in the fluid state.[38-40] In analogy, the less packed extremities and rims of the tubule bilayer

might offer the possibility to interact with the PNIPAM or PNIPMAM dangling chains of the microgels particles, contrariwise to the well-ordered walls presenting a lower solubility.
Finally, it was possible to investigate the interaction between negatively charged tubules and water soluble rhodamine. The aim of the experiment was to image directly through CLSM the tubules highlighting the binding sites and at the same time obtain major insights on interaction mechanisms. It was expected that when added to the tubule sample the cationic form of rhodamine could substitute the tubule counterions. The local fluorescence profile, related to the local concentration in rhodamine, could then be determined after long time image acquisition (Figure 2.8).

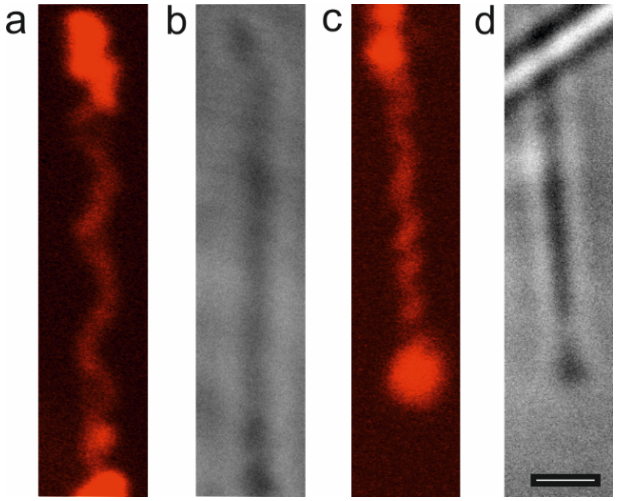

Figure 2.8. The preferential interaction of rhodamine at the edges of the triangular rolled layer forming the scrolls is shown by CLSM images on catanionic samples at $X_{ACD} = 0.7$. The fluorescent micrographs in a and c are obtained from the maximum intensity projection of xyz-stacks. b and d show corresponding transmission snapshots of the tubules. Scale bar=1μm. Adapted with permission from Ref 98. Copyright 2018 Wiley-VCH.

In Figure 2.8 the preferential association of the dye at the rim of the rolled supramolecular sheet forming the tubule is clearly marked. Due to this specific binding the fluorescence was particularly strong at the ends of the scrolls. Remarkably, some excess fluorescence was also emitted from the helical rim along the tubule making its helical profile, so far only evidenced by TEM, directly visible by CLSM. This result suggests that edges presented the highest density of exceeding charge heads (carboxylate groups in this case) and corresponding counterions, thus further explain the observed specific binding of oppositely charged microgels on catanionic rolls. It is worth remarking that as the curvature of the rims is different at the extremities and along the tubules, they could also have different charge densities which could further affect the rhodamine distribution and the related fluorescence pattern.

2.4 Conclusions

Using supramolecular and supracolloidal assembly pathways, we were able to demonstrate the specific and selective association between preformed BSD tubules and microgels. As interaction was promoted towards the edges of the tubules, it provided the possibility to build up defined architectures and low-density networks where the microgels, *i. e.* spherical particles, were linked through anisotropic communication channels. Catanionic tubules were here used with the clear advantage that their charge could be tuned by adjusting their composition, which was highly relevant to investigate the effect of electrostatic interactions on the assembly and in general to get insight into the nature of the supracolloidal interaction. Very interestingly, the results demonstrated that, without resorting to any specific functionalization, the supramolecular tubules spontaneously showed specific binding sites, thus unveiling fundamental binding features of these structures and promoting them as particularly suitable elements in the directed association at supracolloidal level. Therefore, with respect to their use as encapsulators or templates, the reported results highlighted a novel development of supramolecular tubules as building blocks for supracolloidal architectures opening up for the implementation of new functional materials. The hollow nature of the supramolecular elements supplies some additional features to the network such as a particularly low density and a protected communication among the linkers. The proposed concepts are very general and could be extended to sphere-tube superstructures of different materials and at different scales. We envision that assemblies similar to virus-like aggregates and networks could be implemented with nanoparticles or nanotubes to form structures with optical and electronic features not revealed so far. In addition, the selective interaction reported in this study represents an important knowledge in several nano-technological applications of tubules in the field of sensors or drug delivery, which could significantly benefit from a controlled docking to diverse substrates such as electrodes or cells. Lastly, following Nature's ability in fabricating complex materials by assembly at supramolecular and supracolloidal levels, the current synthetic developments combining molecular and colloidal building blocks will be keys to create more intricate bio-inspired superstructures.

3 Chapter 3: Hierarchical co-assemblies of HNaphC supramolecular tubules and polymeric particles

3.1 Chapter rationale

In the previous chapter, BSDs supramolecular tubules and polymeric microgels in aqueous solution were found to interact with different degrees of specificity. The outcome of this interaction was the formation of supracolloidal structures where, in principle, the architecture could be chosen depending on the charge of the two colloidal species together with the type of tubular aggregate used. One of the main conclusions was that electrostatic force between the opposite charges of the two aggregates was modulating and enabling the interaction. However, interactions were also observed in the absence of the electrostatic interaction component, such as in the case of catanionic neutral tubules, which means that the high specificity and the strength of the interaction observed in these conditions were relying also on hydrophobic effect, van der Waals short range interactions and a certain reciprocal affinity between the counterions of the two species (namely I^- and Na^+). As these forces are developed and stronger in correspondence of the tubules surfaces discontinuities (edges), the explanation for the high specificity was more clear. It is worth to remark that even if the interaction was specific the result was often affected by the polydispersity of tubular structures in both cross section and length preventing the formation of a homogeneous tridimensional supracolloidal framework. Moreover, a relevant geometric factor needs to be invoked, in fact, the disproportion between tubules radius and particles radius had a reasonable weight on the interaction success.

Herein, exploiting the same interaction mechanisms described in the previous chapter, the realization of various and well-defined supracolloidal frameworks with outstanding control over their morphology is reported. As deeply analyzed further in the text the interaction pathway through the tubules and the spherical linkers is confirmed to be recursive. Fixing the number density of tubules n_{tub} constant and adding increasing amount of microgels it was observed the progressive formation of core-corona assemblies and interconnected frameworks. A wider range of fluorescent spherical particles was used, varying their size, charge and chemical composition. The interaction with the HNaphC anisotropic structures previously described was analyzed.

Pure HNaphC supramolecular tubules were used in the whole study keeping constant their composition and charge in all the experiments, as they have been proven to constitute an improvement for the framework stability and extension, with respect to tubular aggregates used in the past based on ACD/CCD mixtures. A list of microgels used is given in Table 3.1. One of the most interesting insights provided in this chapter is the structural features achievable from this system, which is composed from identical interconnected spherical units spaced by tubules, with a well defined interaction potential on their tubular extremities. This unprecedented specific interaction allowed for the formation of ordered three-dimensional superstructures having some similarities with crystalline lattices, even though the fluid nature of the system makes not trivial the repetition of regular geometries across the whole structure.

Particle	Core	Shell	$R_{H, T=20°}$ (nm)	Dye
M+	PNIPMAM		298	TRITC
*__M-__[103]	PNIPMAM		244	TRITC
CSM+	PS	PNIPAM	401	FITC

*Characterization details are reported in ref. 103

Table 3.1. List of microgels used for the experiments reported in Chapter 3. Details were already reported in the previous chapter apart from M-.

3.2 Core-corona assemblies

In order to induce the proper formation of supracolloidal frameworks in a mixture of the two species a protocol and a specific method were implemented. The experimental apparatus was formed by a thermostated vessel containing a freshly prepared HNaphC 2mM tubules dispersion gently stirring at 20°C (Figure 3.1). Details on preparation of HNaphC supramolecular tubules and characterization of polymeric particles were given in Chapter 1.
Since the interaction between the particle is instantaneous and abrupt, to reduce mixing failures and local phenomena, the fluorescent particle dispersion was added dropwise with a syringe connected to the bottom of the stirring vessel through a tubing. From the final mixtures where performed regular withdraws with a pipette. A drop was deposited on a microscopy glass and then analyzed through CSLM. The fluorescent particles were dispersed in a 15 mM $Na_2CO_3/NaHCO_3$ buffer solution at pH 9.5 in order to avoid a decrease of pH of the final mixture. The result was the formation of specific supracolloidal structures depending on the

microgels weight fraction. Keeping really low ($c_{\mu gel} \leq 8x10^{-4}$ wt%) the microgels weight fraction in the final mixture and keeping constant both the BSD concentration and pH (respectively at 2mM and pH 11.50) but varying the microgel core particle, it was possible to obtain different core-corona assemblies with different features in terms of size of the core and number of tubules attached on the surface as depicted in Figure 3.2.

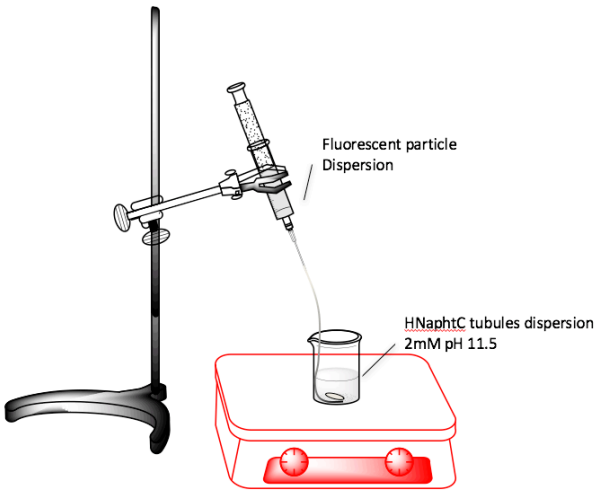

Figure 3.1. Experimental setup for microgels/HNaphC mixtures preparation: a low concentrated microgels dispersion in buffer solution is addedd with a syringe dropwise through a tubing directly at the bottom of a vessel where the tubule dispersion is gently stirring at room temperature.

The core-corona supracolloidal structures were clearly imaged by CLSM. In the above mentioned conditions the fraction of tubular structures was much larger than that of the microgels and free tubules could be imaged in the dispersion. By analyzing samples at different microgel size and similar charge, the effect of the microgel radius on the core-corona structure could be investigated. The results indicated that the increase of the number of tubules adsorbed on the core surface is proportional to the estimated hydrodynamic radius of the microgels. Although an exact estimation of this number could not be addressed easily through confocal analysis, it was possible to roughly determine a proportionality between R_H of the microgels and the number of attached tubules visible in the focal plane selected for the imaging of the core-corona assembly. The connectivity of these supracolloidal complexes was heavily influenced by time. To check the kinetics of the interaction among core corona-assemblies, a sample was diluted 2 times in order to clean the detection volume of the specimen from the majority of tubules not adsorbed on the particle surface. At $t = 0$ the supracolloidal units were basically far from each other and presenting the self-diffusion in the order of magnitude of a colloidal spherical particle in Brownian motion. However, their motion was partially hindered by the elongated anisotropic structures in their corona and consequently self-diffusion

coefficients will look lower in modulus with respect to that of free particles. After some time, core-corona assemblies were more and more able to stick together forming couples, triplets and so on, up to little highly ordered clusters which can be defined as "colloidal molecules". Given the big size of these supracolloidal particles and considering the presence in the solution of tubules not adsorbed to the microgels surface, characterization of diffusion properties was hard to investigate through scattering techniques. To overcome this, was possible to estimate a rough self-diffusion coefficient (D_s) for each different core-corona assembly through Mean Square Displacement analysis (MSD) based on CSLM frames and calculated from particle trajectories in diffusive regime. The results are indicated in Figure 3.4 and Table 3.2 and show a decrease of D_s inversely proportional to the hydrodynamic radius of the core.

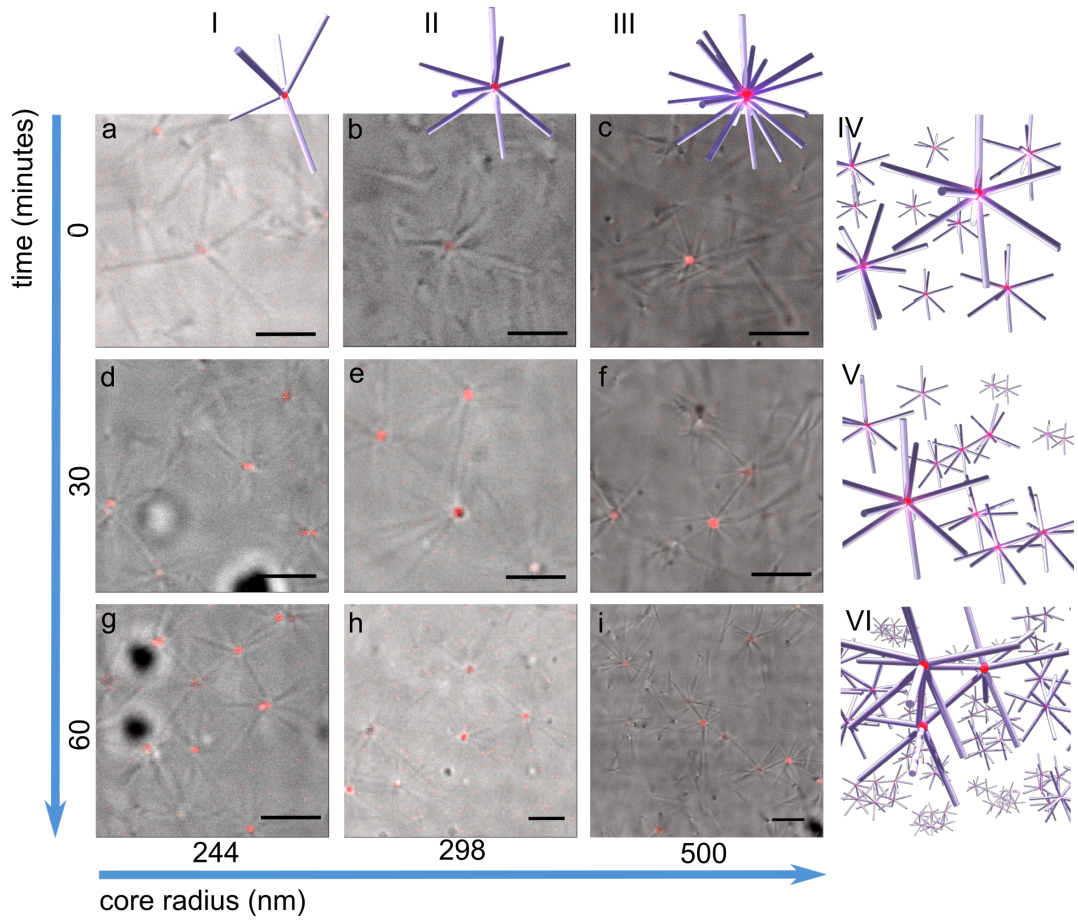

Figure 3.2. Combination of fluorescence and transmission CSLM modes of core-corona assemblies with different microgels cores ($c_{\mu gel}$ = 8x10^{-4} wt%). M- (scheme I, a, d and g), M+ (scheme II, b, e and h) and CSM+ (scheme III, c, f and i). C_{HNaphC} = 2mM at pH 11.50. The number of tubules adsorbed on the microgels surface depends on the microgels radius. With increasing times different units interact to form colloidal molecules and clusters (schemes IV, V, VI). Scale bar: 5μm.

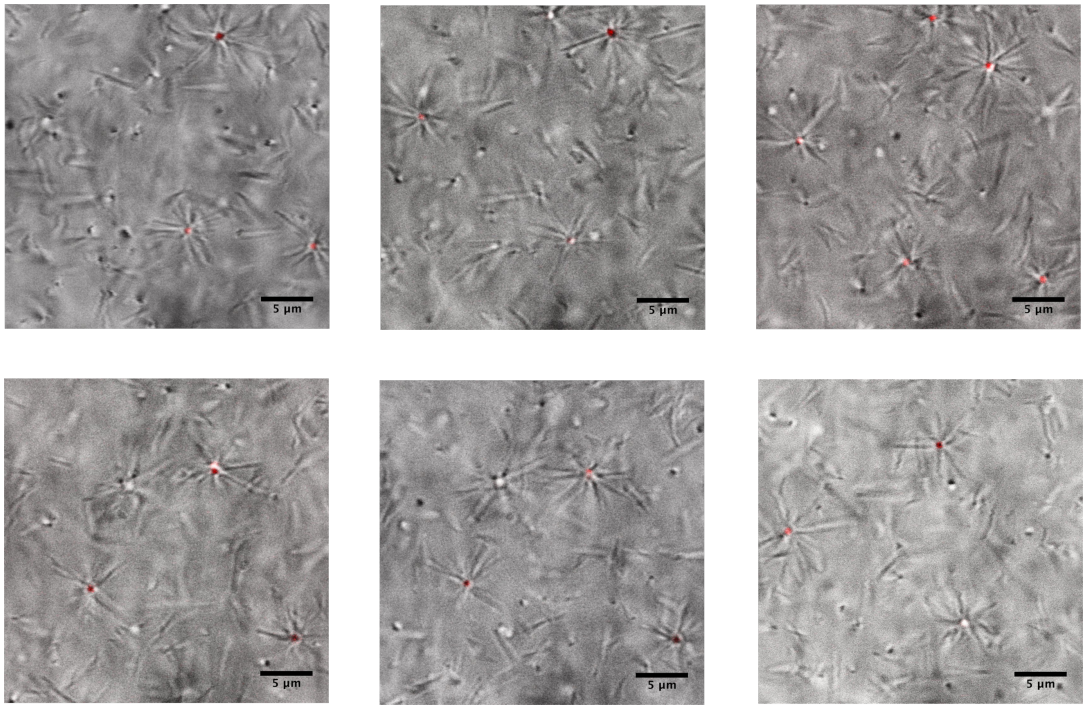

Figure 3.3. CSLM micrographs as combinations of fluorescence and transmission CSLM modes reporting core-corona assemblies of M+ microgels with concentration $c_{\mu gel}$ = 8x10^{-4} wt% at pH 11.50 and C_{HNaphC} 2mM.

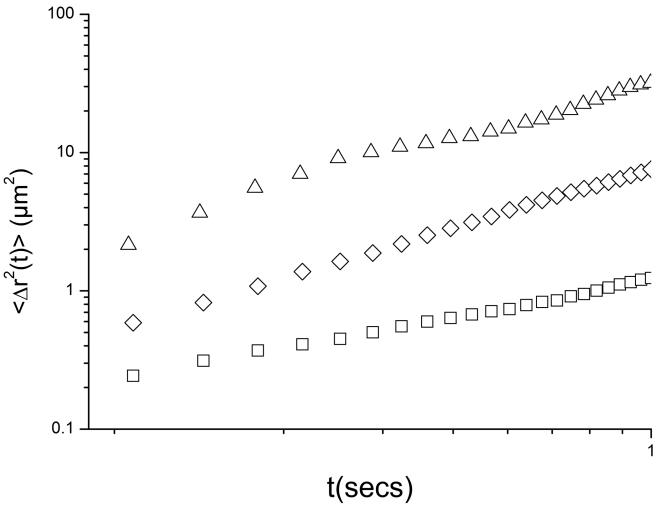

Figure 3.4. Mean Square Displacement $<\Delta r^2(t)>$ vs. time (secs) for three different core-corona assemblies with different size of core radius (R_H): 244 nm (triangle), 298 nm (diamond) and 401 nm (square)

Core - type	Core $R_{h,\ T=20°C}$ (nm)	Self- Diffusion coefficient D_s ($\mu m^2\ s^{-1}$)
M-	244	8.180
M+	298	2.036
CSM+	401	0.272

Table 3.2. Values of diffusion coefficients (D_s) obtained from Mean Square Displacement analysis.

3.3 Supracolloidal Sphere-Tubule Frameworks

Therefore, an analysis at increasing fraction of microgel up to 0.05 wt% was performed, finding that at sufficiently high fraction a supracolloidal lattice can arise from the interaction among spherical particles, characterized by complete interconnection, variable degree of local/medium/long range order and thermo-reversibility. The preparation of such supracolloidal structure followed the same procedure and was performed with the same experimental apparatus precedently reported.

As mentioned in the Abstract of this dissertation, for its features this framework resembled the "Atomium" building, in Brussels and the whole system was called "Superatomium" in honor of the famous work of art.

Again, the response of the system was studied with respect to the increase of R_H of the core particle. In each case studied, the arrangement of the framework was characterized extracting 2D Radial Distribution Functions, *g(r)*, from CSLM images elaboration.

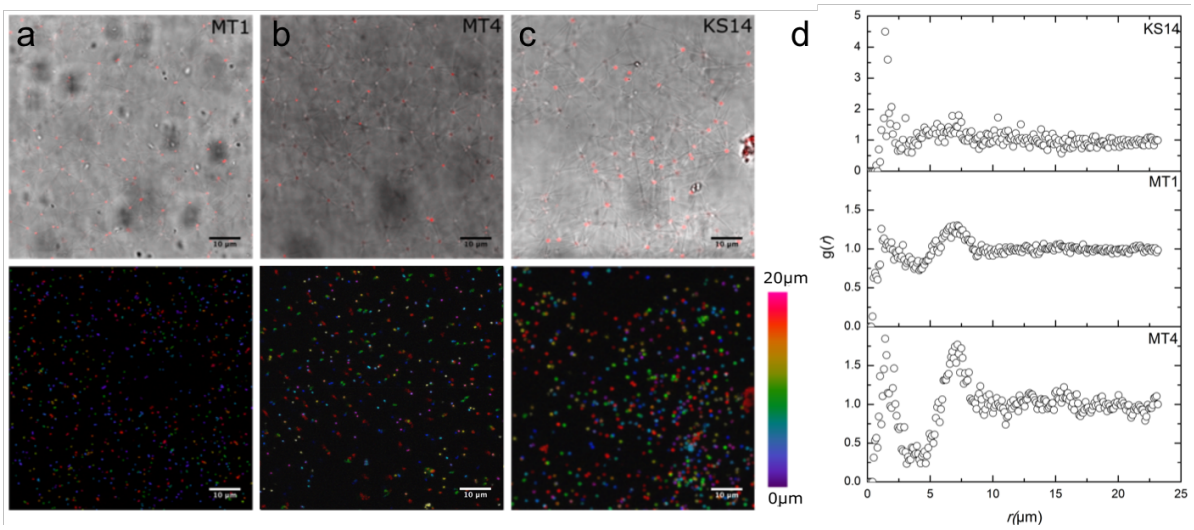

Figure 3.5. CSLM micrographs (top: combination of transmission and fluorescence modes; bottom: orthogonal projection of 3D reconstruction presented as color coded *z*-stacks images). 2D *g(r)* extracted from *z*-stacks acquisitions (standard error is omitted).

The 2D *g(r)* reported in Figure 3.5d with the corresponding sample CSLM micrographs, were calculated from 5 different 20 μm *z*-stacks acquisitions for each sample, averaged on the whole *z*-axis taken in exam. Each curve presents at least two peaks, where the first one falls approximatively within r = 1-2 μm and demonstrates the presence of microgels doublets adsorbed at the tubular edges. The high statistics of this peak comes from two factors: the first one is the actual presence of doublets within the framework which are the result of charges

screening on the microgels surface due to the ionic strength of the solution (and in turn increasing microgels-microgels interaction), together with the peculiar tubular extremity structure which is able to dwell more than one microgel. The other factor comes from an averaging over-estimation, caused by the very small *z*- motion of the particles around their average position. This caused the enriching of the doublets population peak in the *g(r),* since the particles seldom occupy more than one focal plane taken into account in the average. The second peak, falling around 7 μm, is in the order of the tubules length and it is consistent with what observed through confocal microscopy. The M+ based system presents peaks which are visibly sharper as the network is significantly more similar to a lattice with respect to the other systems considered, with another flat peak arising, that could be identified around 15-2μm, proving that this lattice persists as *r* increases up to two times the tubular length. As M+/HNaphC framework was considered the best system in the whole study, a further characterization was carried out. Several images of the M+ based framework are presented in Figure 3.8.

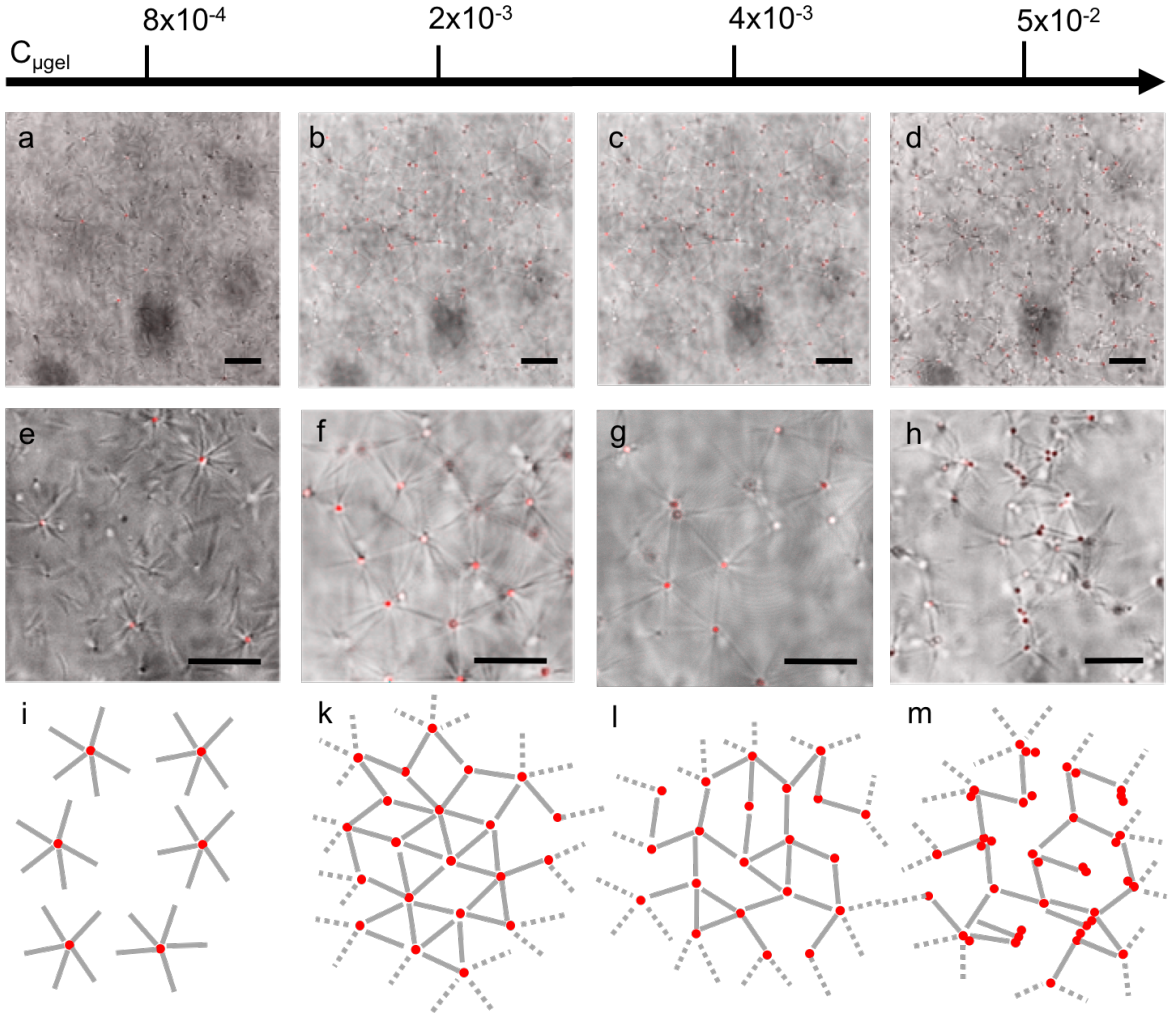

Figure 3.6. CSLM micrographs as a combination of transmission and fluorescence modes of supracolloidal "Atomium-like" frameworks with increasing concentrations of M+ microgels (a-h). Schemes representing the connectivity of the system (i-m) on the *xy* focal plane. Scale bar 10 μm.

G(r) of the sample having $c_{\mu gel}$ = 0.0008 wt% was not reported as the sample is basically a dispersion of core-corona assemblies with no network properties and then no relevant *g(r)*. What can be highlighted is that sample with $c_{\mu gel}$ = 0.002 wt% was the one with the most stable and ordered network connectivity, having a *g(r)* with three peaks, with at least two of them sharp and resolved. Increasing microgels concentration to 0.004wt%, samples preserve most of their connectivity and short range order, however peaks are clearly flatter than the latter case. The decrease in connectivity was certainly due to the increase of $n_{\mu gel}/n_{tubules}$ ratio which had a decisive effect on network branching. Increasing again microgels fraction towards 0.05 wt% microgels-microgels depletion interaction start to be predominant bringing disorder in the lattice and forming bulky groups of microgels adsorbed near the edges of the tubules. The average number of tubules adsorbed per particle is visibly decreasing as microgels fraction increases, even though is rather difficult to check the exact number of tubules attached on the microgels surface across all the dilutions.

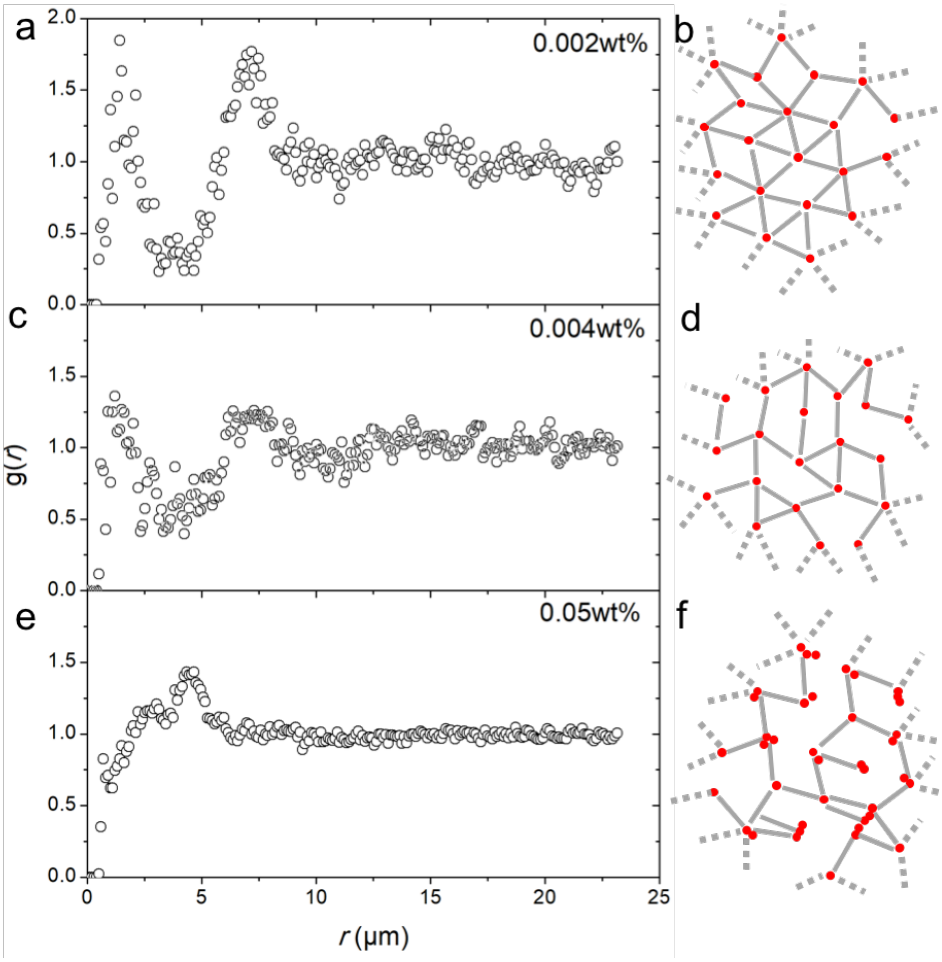

Figure 3.7. *G*(*r*) extracted from *z*-stacks acquired by CSLM on supracolloidal "Atomium-like" frameworks with increasing M+ microgels concentrations (a, c and e) and corresponding scheme (b, d and f) representing the network on the xy-plane.

It is worth to remark that regardless the concentration of microgels present in the mixture no free microgels were ever observed. That means that independently from the $n_{\mu gel}/n_{tubules}$ which has been both above and below 1:1, the interaction between tubules and microgels is strong, and its failure, induced when the critical microgels concentration (0.05wt%) was reached, proceeded with the intervention of the increase of microgels-microgels interaction because of the depletion effect.

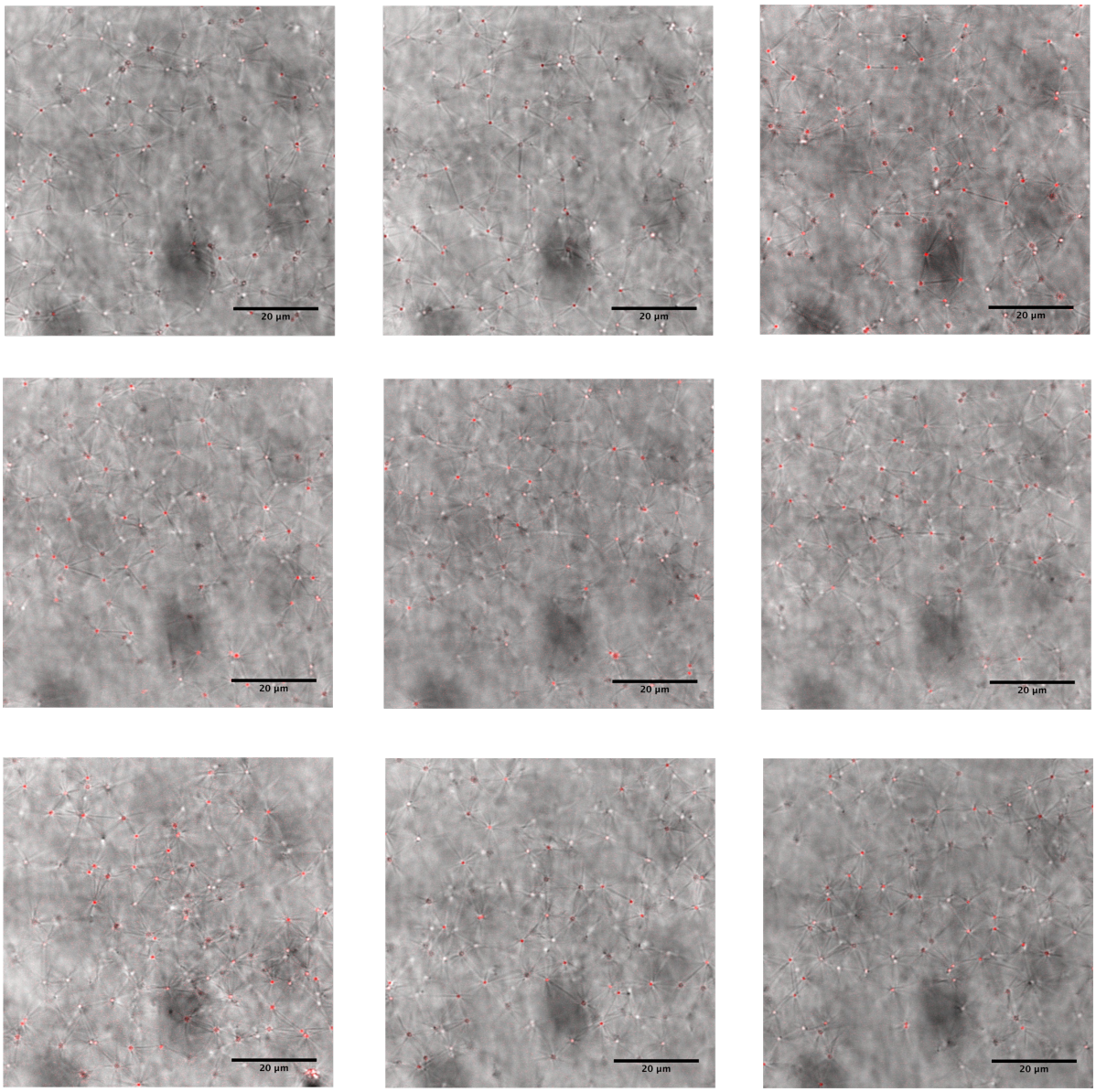

Figure 3.8. CSLM micrographs taken at low magnification and different times from preparation of a 2mM HNaphC pH 11.50 dispersion of supramolecular tubules mixed with M+ TRITC labeled polymeric microgels ($c_{\mu gel}$= 0.002wt%). Images are the superimposition of transmission channel and fluorescence emission channel of the confocal microscope.

3.4 Supracolloidal Sphere-Tubule Framework Formation Kinetics

Kinetics of framework formation was investigated with both CSLM and DLS. To perform DLS experiments, a quartz cuvette containing the HNaphC tubules dispersion kept at pH 11.50 was equilibrated at 20°C inside the instrument VAT. After 1 h from mixture preparation a concentrated dispersion of microgels was mixed very slowly with the tubules directly in the VAT, with a 2mL syringe, and then gently shaken, in order to reach the final microgels concentration of 0.002wt%. After mixing, an aliquot of the sample was taken and monitored with CSLM (Figure 3.10). The time correlation function of the mixture after 4 hours from preparation was then compared with the two obtained from the pure microgels and the pure tubules dispersions as an introductive experiment. The results are presented in Figure 3.9a. Predictably, the reduced translational mobility of the supracolloidal sphere-tubule framework results in a longer decay of the time correlation function with respect to the other two functions. Furthermore, the kinetics was monitored in a new experiment where step by step was performed an acquisition of a TCF each 10 minutes starting from mixture preparation, for a total time of 210 minutes. All the TCFs obtained are reported in Figure 3.9b. What can be seen is that the decay of the function is already delayed at $t = 0$ with respect to that of the only spherical particles, which means that the single units (*i.e.* core-corona assemblies) were already hindered in their Brownian motion at $t = 0$, determining a slow relaxation time because of the friction between the tubular corona and the medium. As the time increases and the single units entangle and interact, clusters form to give rise to the framework, following the pathway already reported in the previous paragraphs, spreading uniformly within the scattering volume. The effect of the network formation is the increase of the decay time of the TCF as reported in detail in Figure 3.9b (the inset is representing log-log version of the correlogram). Visibly, as time increases, the slope of the functions becomes less steep. Another effect although less marked is the progressive decrease of the correlogram intercept as a side effect due to the progressive arrest of the network. Consistently with DLS data, CSLM micrographs (Figure 3.10) show a slow but constant improvement of the network homogeneity together with both long- and short-range orders, towards a fully connected lattice which was reached after approximately 210 minutes. Accordingly to CSLM and DLS, was evidenced how the first interaction among core-corona units, to form the primary clusters, was a fast process with respect to that belonging to the arrangement and order degree increase throughout the specimen.

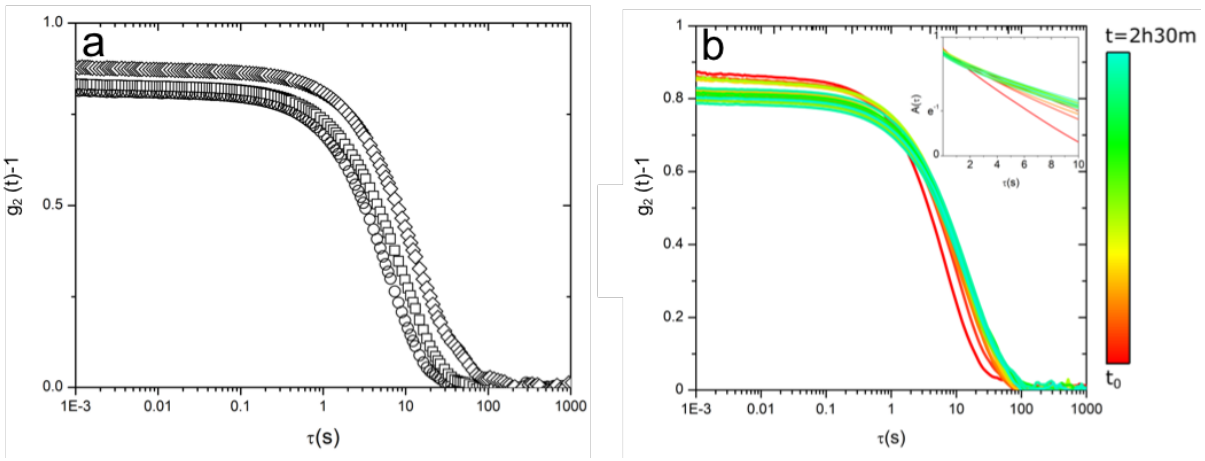

Figure 3.9. DLS autocorrelation functions of 0.002 wt% M+ microgels suspension (circles), HNaphC tubules dispersion (squares) from a 2mM solution at pH 11.50, and mixture of both at t = 0 and $c_{\mu gel}$ = 0.002 wt%(diamonds) (a). DLS autocorrelation functions registered every two minutes at 20°C from the mixture preparation (b). Detector angle: 50 deg (a) and 90 deg (b).

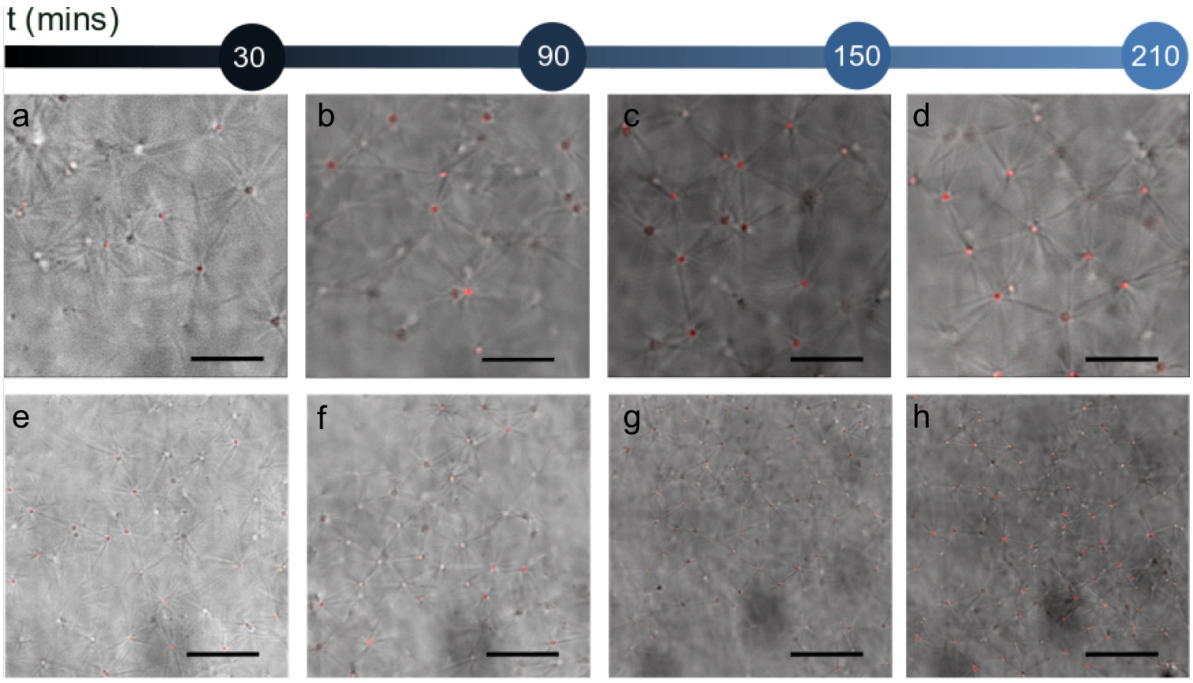

Figure 3.10. CSLM micrographscombinations of transmission and fluorescence channel of a M+ HNaphC "Atomium-like" framework sample with increasing time. Scale bar 5 μm (a-d) and 10 μm (e-h). The kinetic of the system develops in approximately 3.5-4 h and its basically governed by the adjustment and arrangement of the framework from branched superstructure towards an ordered supracolloidal lattice.

3.5 Supracolloidal Sphere-Tubule Framework Thermo-responsivity

The response of the supracolloidal lattice to heating was tested with another CSLM experiment and followed through DLS. A mixture composed from HNaphC tubules and M+ microgels 0.002wt% was pipetted in a flat bottom quartz cuvette and left inside the VAT for around 3 h at 20°C, the laser shutter was kept closed to avoid any local heating due to the laser radiation. After that, the shutter was opened and experiment started setting the goniometer at 90° and the measurement time duration at 60 secs. The temperature was then increased from 20°C to 45°C

and then a first measurement was performed. The temperature was then gradually decreased in a controlled manner and set from 45°C (starting temperature) to 20°C (final temperature) acquiring a total of 45 autocorrelation functions in a time span of approximately 4 h. The results are plotted in the following graph (Figure 3.11a). CSLM experiment was performed simultaneously with the DLS experiment. CSLM measurements were carried out as follows: few microliters of the M+/HNaphC mixture were taken from the DLS quartz cuvette from the heated up sample, and rapidly transferred on a microscopy glass slide. The specimen was then imaged, following the cooling by decreasing manually the temperature of the controlled CSLM enclosure (images are reported in Figure 3.13b).

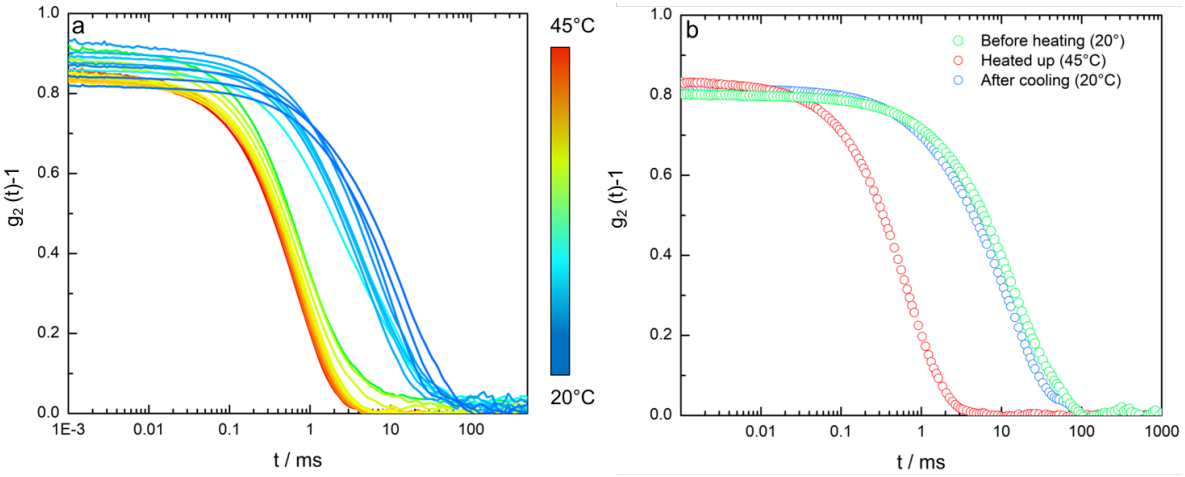

Figure 3.11. DLS autocorrelation functions of M+ HNaphC supracolloidal "Atomium-like" framework ($c_{\mu gel}$ = 0.0020wt%). Autocorrelation functions with decreasing temperature from 45°C to 20°C. The curves are presented color-coded, following the temperature change in the VAT, as showed in the right panel (a). Autocorrelation functions of the same specimen at 20°C (before the heating), heated up to 45°C and stabilized after being cooled down to 20°C (b).

The temperature was already proven to have a negative impact on both the microgels and the HNaphC supramolecular structures. HNaphC tubules disaggregate when temperature is increased beyond 30°C. Moreover, it is well known the behavior of PNIPAM polymer when subjected to temperatures near to 32°C-33°C which implies change in hydrophobic-hydrophilic balance of the polymer chains, resulting in a volume phase transition (VPT) of the microgels from the aqueous solution. The outcome of these two catastrophic effects was clearly visible through DLS since decay of the TCF was becoming less and less marked and slow as the temperature was decreasing and moving across the transition temperatures, towards the stabilization of the initial system. Interestingly a marked shift of the TCF took place between 30°C and 28°C probably related to the aggregation of the supramolecular structures previously disassembled by the heating stress. Meanwhile, through CSLM was not possible to observe neither supracolloidal structure nor fluorescence emission from the corresponding fluorescence

channel (Figures 3.13b, f) until 20°C were reached again (Figure 3.13c, g). As soon as the temperature inside the CSLM controlled environment reached 20°C, no supracolloidal framework was observed yet, but instead a population of core-corona assemblies was present and characterized by smaller tubular lengths, high number density, low $n_{\mu gel}/n_{tubules}$ ratio and overcrowded detection volume. That allows to hypothesize that HNaphC supramolecular tubules have the ability to interact with the microgels no matter the stage of aggregation. The final stage of the cooling process was represented by the complete formation of the supracolloidal framework as the TCF became delayed by more than 1 order of magnitude and intercept decreased. From CSLM was also observed an elongation of the supramolecular tubules which in turn caused the increase of the center-to-center distance among the microgels particles, now fully interconnected with a reduced translational movement resembling the starting conditions.

Besides, although the system was demonstrating reversibility after destructive heating process, the TCFs acquired at 20°C before and after the heating had basically same features (Figure 3.11b) but to a different extent. As proved by CSLM measurements (Figure 3.13d, h), the network structure obtained after the cooling down procedure was not comparable in connectivity and in both short- and long-range orders with the initial lattice. This difference was due to the nucleation process of tubules induced by temperature variation which may differ from the one induced exclusively by the increase of pH from spontaneous values to pH 11.50 at 20°C. In fact, an increase of tubular length polydispersity was observed in the sample from the cooling experiment. This consideration was supported by analysis of the *g(r)* extracted from the *z*-stacks on the sample before and after the heating-cooling experiment and consequently reported above in Figure 3.12.

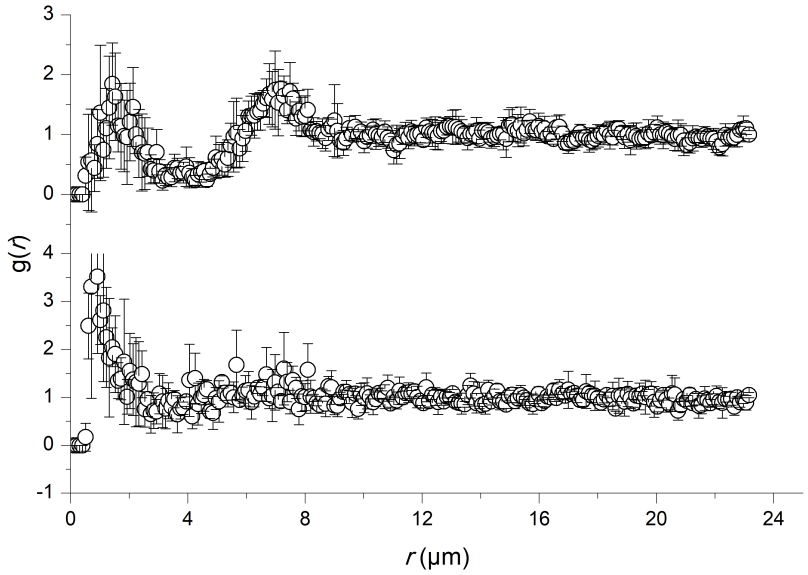

Figure 3.12. *G(r)*s extracted from *z*-stacks of M+ HNaphC mixtures of supracolloidal frameworks having $c_{\mu gel}$ 0.0020wt%, before (top) and after(bottom) heating-cooling experiment.

What can be immediately noticed is that after the cooling of the sample to the initial temperature conditions the framework was not able to interconnect efficiently as it used to do before its destruction. Peak at 7-8 μm is flattened and broadened. First peak shifts back to smaller values of r probably due to the formation of little clusters of spherical particles due to the heating induced destabilisation. No significant relevance was addressed to this effect. In conclusion the interaction strength was apparently preserved and restored to the initial conditions.

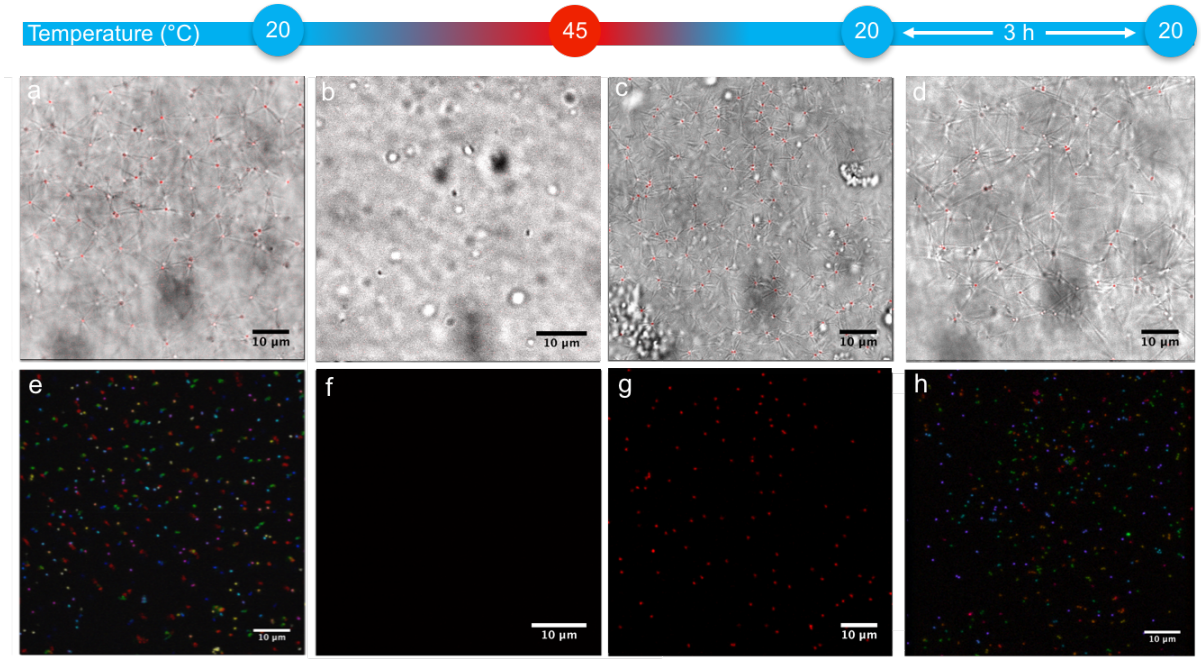

Figure 3.13. Combination of CSLM transmission and fluorescence channels (a-d), color coded images of *z*-stacks (e, h) and fluorescence emission (f, g) of M+ HNaphC with $c_{\mu gel}$ = 0.0020 wt% at pH 11.50 at variable temperatures. After 45°C were reached, sample was cooled down to 20°C (right

3.6 Fluorescent Sphere-Tubule Frameworks

To better highlight the three-dimensional framework structure a fluorescent bile salt was synthesized. The inclusion of such compound in the HNaphC bile salt supramolecular tubular structure was envisioned to give more visibility to the sphere/tubule interaction taking place at supracolloidal level. In order to exploit the CSLM Argon laser emission line λ_{em}= 470 nm and to use a small sized probe (similar to the naphtoyl-amine- group present in C3- position of HNaphC), NBD-Cl (4-chloro-7-nitro-1,2,3-benzoxadiazole) was selected as fluorescent probe to functionalize the pure cholic acid on the C3- carbon position. A general scheme for the synthesis of the molecule is reported above and led to the final compound of Figure 3.14.

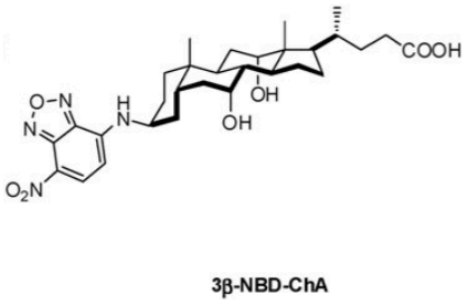

Figure 3.14. Molecular structure of the fluorescent NBD-derivative of cholic acid.

The fluorescent derivative (NBD-ChA) selected (for structural similarity to HNaphC) was the 3β.

3.6.1 Summary of NBD-ChA synthesis

The synthesis described below refers to the preparation of a fluorescent anionic derivative of CA, already synthesized from Rohacova *et al*.,[104] which aggregation has been already partially investigated for the characterization of BSs micelles,[105–107] merely from a structural standpoint from Cuquerella *et al*.[108] Herein the specific synthetic pathway adopted in the form of brief summary suitable for the fruition of this work is reported. The derivative was obtained by a three step functionalization of the hydroxyl group on carbon 3-α (C-3) of CA with the fluorescent probe 4-chloro-7-nitro-1,2,3-benzoxadiazole (**1b**) via an amine bond. As already mentioned the so called NBD-ChA was obtained through three essential steps as depicted in the scheme of Figure 3.15. The first was the substitution of the 3-α hydroxyl group, present on

the starting compound CA (**1a**) with the mesylate, a good leaving group in nucleophilic substitution reactions. The following step consists in the conversion of the mesylate in a primary amine via catalytic reduction having as a result the compound (**5**). The amine allows for the further conjugation of the NBD to the steroidic skeleton through a nucleophilic aromatic substitution and subsequent cleavage of the ester bond (**6**), ending up with the compound (**7**).

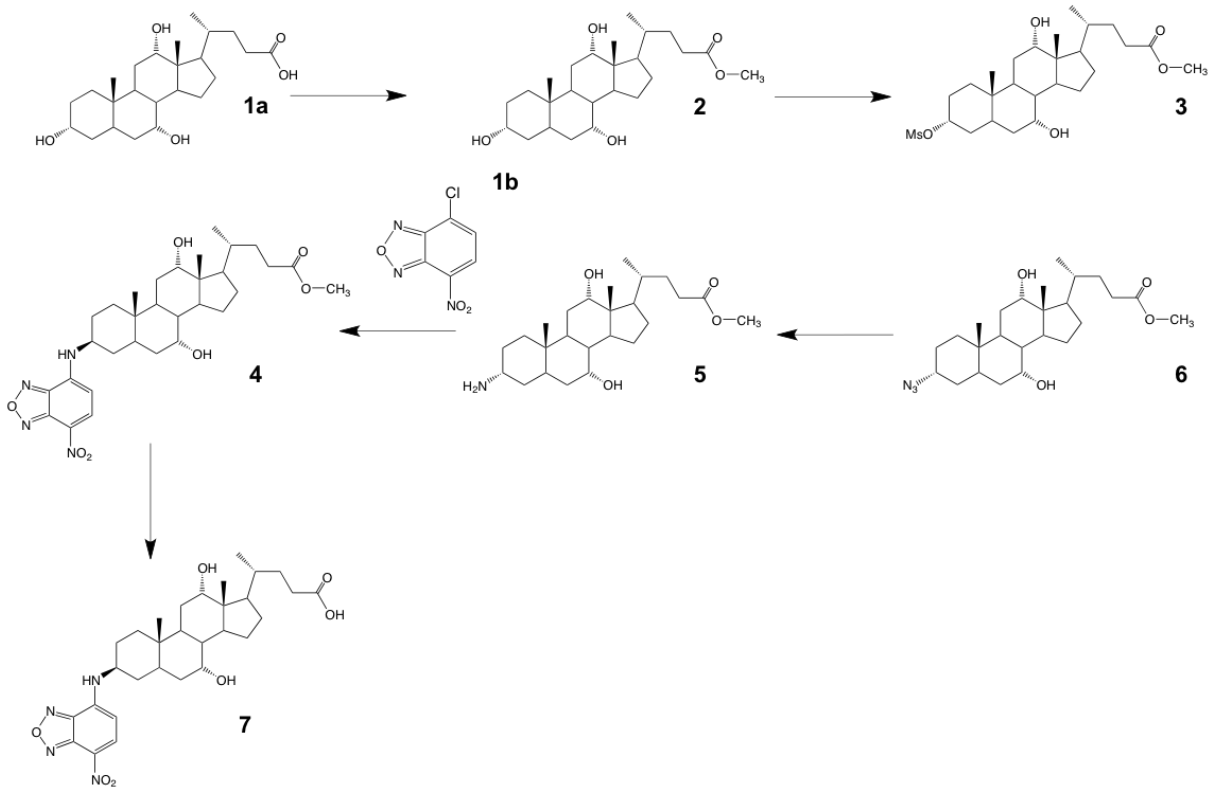

Figure 3.15. Synthetic pathway for the preparation of 3β-NBD-ChA (**7**) using as starting molecules CA (**1a**) and NBD-Cl (**1b**).

The esterification of the carboxylic group in C-17 of CA using methanol is a common reaction used for two main reasons: to protect the carboxylixc group due to its high reactivity in the reaction environment and to enhance the solubility of the natural bile salt, hardly soluble in organic solvents. The preparation of the compound (**2**) followed a protocol according to the description reported from Gouin and Zhou[109] as depicted in the scheme of Figure 3.16 and giving rather high yields (93%).

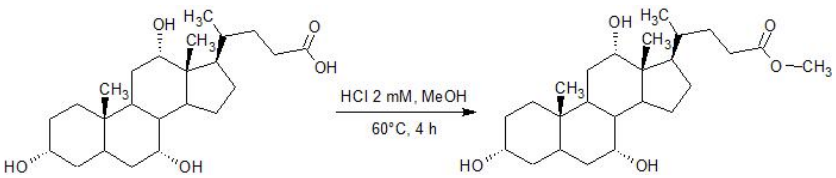

Figure 3.16. Synthesis of the CA methyl ester (**2**).

The C-3 position of the steroidic skeleton has been very often used for derivatization in past works employing carbohydrates such as glucose and mannose,[73] hydrophobic moieties (naphtoyl-, t-butylbenzoyl-)[78,79] and aminoacids (tryptophan, phenylalanine)[72,110] with various synthetic approaches. In this case the conjugation reaction needs the substitution of the C-3 OH, a bad leaving group, with the good leaving group MsO (mesylate), via an S_N2 mechanism, in order to extremely facilitate the consequent C-3 insertion of the N_3 group, necessary for the further steps. Albeit the procedure adopted was already reported in the above mentioned works were found high discrepancies with respect to the amount of trimethylamine (Et_3N) and mesyl-chloride (MsCl) used in literature and hence the conversion of the initial substrate (**2**) in (**3**) requested more reagents in order for the reaction to proceed accordingly. Was hypothesized that possible aggregations phenomena regarding the methyl cholate could have been detrimental for the access of the methanol to the reaction site (carboxylic group). The increased concentration of mesyl chloride, was probably responsible for an increase of the ionic strength of the solution resulting in the aggregates rupture to the form of monomers. This reaction step was crucial also for the impossibility to quantify yields due to significantly high amounts of impurity in the final product.

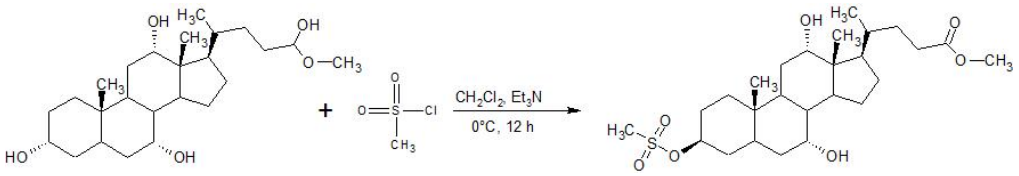

Figure 3.17. Synthesis of the compound (**3**).

The good leaving group mesylate was replaced by the azide through nucleophilic substitution with a S_N2 mechanism as represented in the scheme in the Figure 3.18. The reaction brought to a yield of 58%.

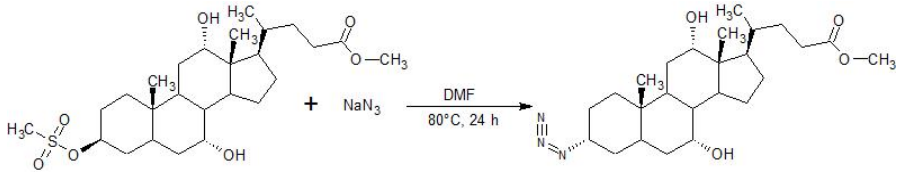

Figure 3.18. Synthesis of the compound (**4**).

The use of a Pd \ C (Pd 10%) etherogeneous catalyst was mandatory for the reduction of the C-3 azide in amine. The complete reaction was carried out as represented in Figure 3.19. The

compound (**5**) was highly instable and thus stored at -4°C due to the tendency to isomerization and scarce thermal stability. The yield obtained of the expected compound was 80%.

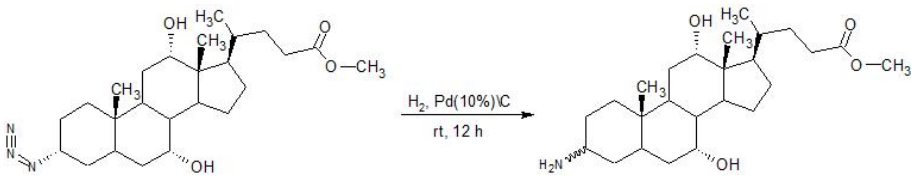

Figure 3.19. Catalytic reduction used in synthesis of compound (**5**).

The conjugation of fluorescent probe (**1b**) to compound (**5**) was carried out through a nucleophilic aromatic substitution between the C1 chlore of the (**1b**) aromatic ring and the nitrogen of the amine group belonging to compound (**5**) which had the role of the linker (Figure 3.20). The yield of compound (**6**) estimated was 48%.

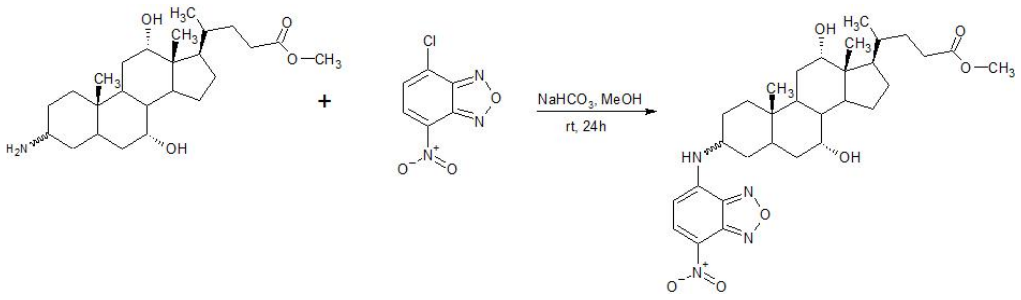

Figure 3.20. Synthesis of the compound (**6**).

The last reaction step was the alkaline hydrolysis of the carboxylic group of the compound (**6**). Compound (**7**) was obtained with yield ranging between 27% and 73% depending on post column purity. The purification was crucial not only to remove the scarce presence of the 3α isomer (the amine tend to maintain the azide configuration) but also because (**7**) had the tendency to adhere on the solid phase and a series of eluitions with polarity gradient (from lower polarity to higher) was requested for the complete eluition of the hydrolyzed. In literature was found that a method implying the use of silica reversed phase column as purification approach.

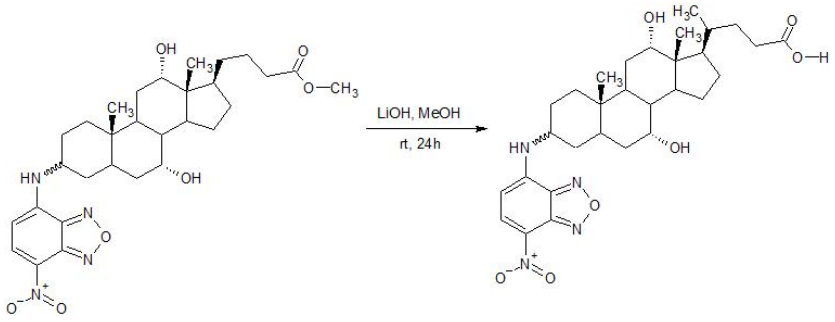

Figure 3.21. Preparation of compound (**7**) through hydrolysis of compound (**6**).

Compound **7**: **^{1}H-NMR** (400 MHz, CD3OD): δ (ppm) 0.74 (s, 3H, 18-CH3); 1.03 (t, J=6.42); 2.88 (d, J=0.67); 3,01 (d, J=0.37); 3.32 (m, J=3.29-1.64); 3.36 (s); 3.83 (s); 3.99 (br s, 1H, 12β-H); 4,87 (s); 6.38 (br s); 7,99 (s); 8.49 (d, J=8.80 1H, 5'-CH(Ar)); **^{13}C-NMR** (75 MHz, CD3OD): δ (ppm) 11.56; 16.23; 21.98; 22.78; 26.31; 27.26; 28.4; 30.64; 30.73; 30.92; 33.94; 34.80; 35.38; 35.52; 37; 39.58; 41.62; 46.16; 46.65; 46.94; 47.18; 47.37; 47.58; 47.77; 48; 48.21; 48.42; 67.59; 72.55; 176.79. ESI-MS: calc. for [$C_{30}H_{42}N_4O_7$]: 570.3055; found 569.55.

3.6.2 Fluorescence emission characterization of NBD-ChA and of NBD-ChA/HNaphC mixture in supramolecular aggregation conditions.

Fluorescent supramolecular mixed tubules were prepared as follows: a stock solution of NBD-ChA 200 mM was prepared rising the pH at 11.50 due to the low solubility of the derivative in pure water at spontaneous pH. The sample was kept under vigorous stirring overnight. A HNaphC stock solution was prepared separately at pH 8.5 1.2 mM. The two compounds were then mixed under stirring, injecting dropwise the NBD-ChA solution in the HNaphC solution until a 4μM final concentration was reached. In the meantime pH of the final solution was eventually adjusted to 11.50 in order to trigger the formation of tubules. NBD-ChA was already synthesized and characterized by other groups and its fluorescence was basically addressed to the presence of two absorption bands ($\lambda_{max,1}$= 380 nm and $\lambda_{max,2}$= 450 nm) both able to shift depending on different factors such as pH and solvent polarity. In the experimental condition the two maxima were found to be centered respectively at 360 nm and 468 nm. While the less intense band is due to the $\pi \rightarrow \pi^*$ transition of the aromatic ring of the NBD-ChA, the second one is the result of an energy transfer involving the amine bond between the probe and the bile

salt molecule, in fact no fluorescence has been observed when probe is not provided of an amine group. Since the latter transition band is stronger with respect to the other (ε = 25000 M^{-1} cm^{-1}) this excitation band was used to induce the fluorescence emission. In water and in alkaline conditions the fluorescence spectrum was acquired and reported in Figure 3.22, right.

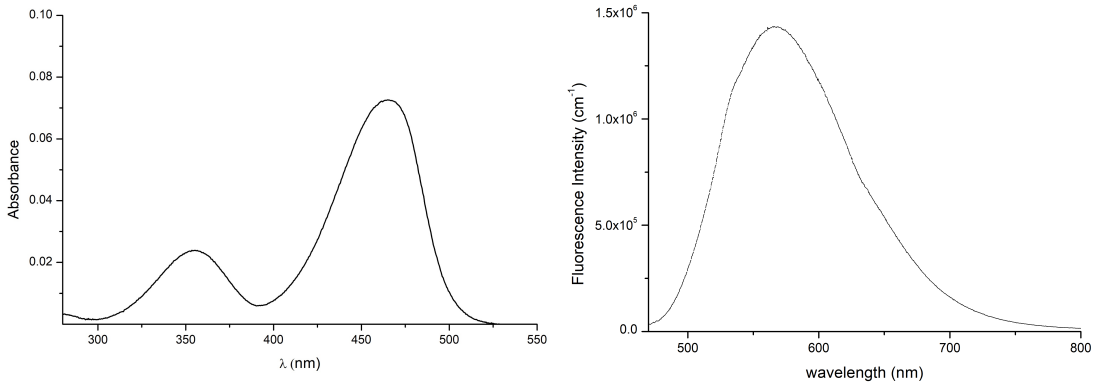

Figure 3.22. UVvis (left) and fluorescence emission (right) spectra of NBD-ChA 4μM at pH 11.50.

Fluorescence peak falls at 567 nm which is in line with the value already reported in literature. Previous works based on the fluorescence features characterization of NBD-ChA proved how the change of micro-environment from polar to non-polar has a remarkable effect on the emission. Specifically Cuquerella et al.[108] reported how the non-polar micro-environment, in NBD-ChA and cholic acid micelles, has as a result the enhancement of fluorescence emission together with an hypsochromic effect. This behavior of the fluorophore was only characterized about the *cmc* of the CA used in mixture with the NBD-ChA itself. In this case the same method was used to characterize the integration of the probe inside the molecular packed structure of the supramolecular tubules. The fluorescence spectrum of 4 μM water solution of pure NBD-ChA is reported in the figure below (Figure 3.23, right) together with the fluorescence spectrum of the mixture (molar ratio 1:250) of NBD-ChA with HNaphC. Both solutions were kept at 20°C and at pH 11.50 and the fluorescence emissions was excited using an excitation wavelength of 450 nm. As can be inferred from the spectra the fluorescence band peak translates from 567 nm, value in agreement with Schneider et al.[107] and correlated in literature with a slight increase of quantum yield (0.025 to 0.040). The mixture's peak, a little stiffer, has a flat curvature that complicates the peak maximum assignation. Besides, a clear blue-shift is visible to wavelengths near 530 nm, which is in agreement with the expected values. In addition to this is also visible an increase of band intensity due to the non-polar micro-environment that enhances fluorescence emission.

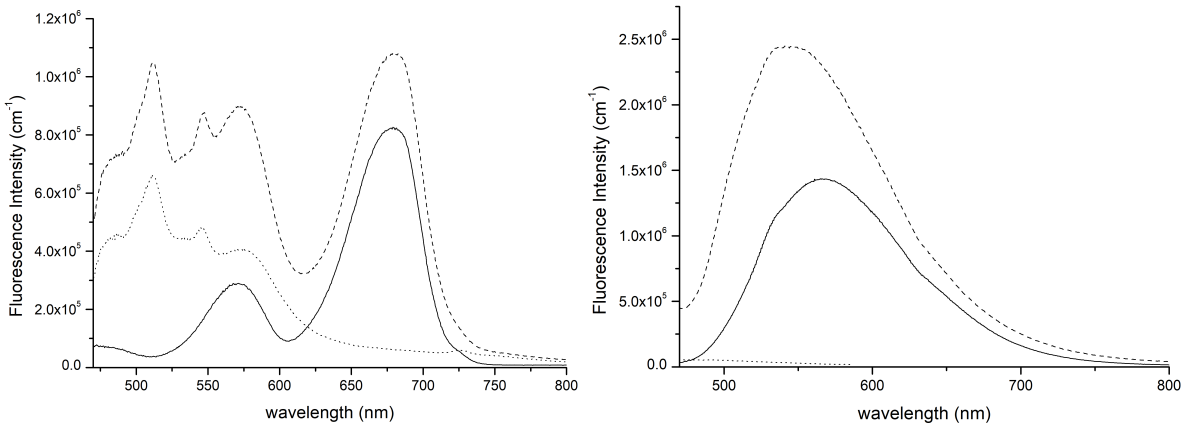

Figure 3.23. Excitation (left) and emission (right) spectra of : NBD-ChA 4μM pH 11.50 in water (solid line), mixture NBD-ChA/HNaphC 1:250 C_{tot} = 1mM pH 11.50 in water (dashed line) and HNaphC 0.95 mM pH 11.50 in water (dotted line). Slits 2.5/2.5 nm, step: 1nm.

This effect, similarly found in other studies where the fluorescence of the compound increases as polarity of the solvent decreases,[111] brings to the assumption of major hydrophobic interaction with HNaphC present in the mixture. This augmented hydrophobic interactions are somehow related to reciprocal perturbation of the dipoles created by photon absorption by the fluorophore at the ground state and of the surrounding molecules dipoles. After the fluorophore has been excited to higher vibrational levels of the first excited singlet state (**S(1)**), excess vibrational energy is in general rapidly lost to surrounding solvent molecules as the fluorophore slowly relaxes to the lowest vibrational energy level (occurring at the picosecond time scale). Non-polar surrounding molecules with a small or absent dipole cannot assist in stabilizing and further lowering the energy level of the excited state by re-orienting the dipoles around fluorophore molecules. This enhances the energy separation between the ground and excited states, which results in a blue-shift (to shorter wavelengths) of the fluorescence emission with a consequential increase in intensity. In Figure 3.23 (left) are reported the excitation spectra of the mixture, the NBD-ChA solution and of a HNaphC 1mM at pH 11.50. In all the three experiment excitation was set at 620 nm and then was scanned the whole spectrum of interest in the interval 450 nm – 800 nm. As a results the excitation spectra (Figure 2.23, left) were found to be in agreement with absorption spectra already reported in literature. In the range 450 nm - 600 nm is remarkable the presence of sharp peaks resembling vibronic bands not present in NBD-ChA spectrum and then correlated to HNaphC molecule. These bands increase in intensity in the excitation spectrum of the mixture as consequence of some energy transfer phenomena of difficult interpretation.

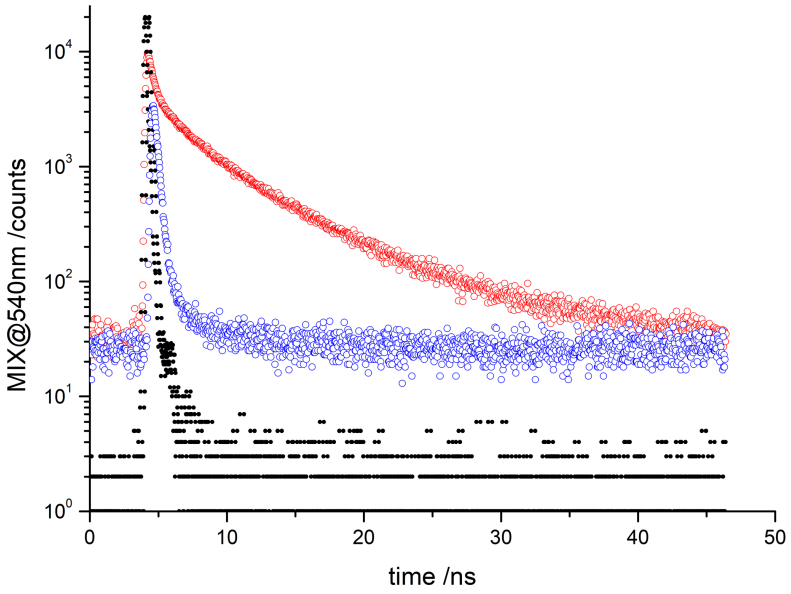

Figure 3.24. Time correlated single photon counting measurement (TCSPC) on NBD-ChA/HNaphC molar ratio 1:250 pH 11.50 (red) and on NBD-ChA pH 11.50 (blue).

Time-correlated single photon counting (TCSPC) measurements were carried out on the same samples to have confirmation on the over mentioned observations. In Figure 3.24 are represented the time decay functions of NBD-ChA/HNaphC mixture at pH 11.50 in aggregation conditions (red) and of pure NBD-ChAsolution at the same pH value. The result shows an increase of decay time in the order of few nanoseconds for the mixture, while NBD-ChA specimen shows fast decay at the picoseconds scale. Emission intensity was lowered with respect to static fluorescence analysis due to the laser excitation wavelength used which was 378 nm, outside the *optimum* spectral range for excitation. A complete interpretation of the result was furthermore helped by polynomial fitting of the curve accomplished through software "PicoQuant FluoFit" which was able to perform the multiple exponential decay time deconvolution obtaining three single decay times τ_1, τ_2 and τ_3 each one related to a precise population of events. As can be seen from the fitting results (Figure 3.25) the majority of the fluorescence emission transitions happened with fast speed (0.269 ns) which indicates that the most of fluorescently labeled molecules do not perceive any change in polar/non-polar balance of the micro-environment and were likely still in bulky water with no interaction with HNaphC packed molecules.

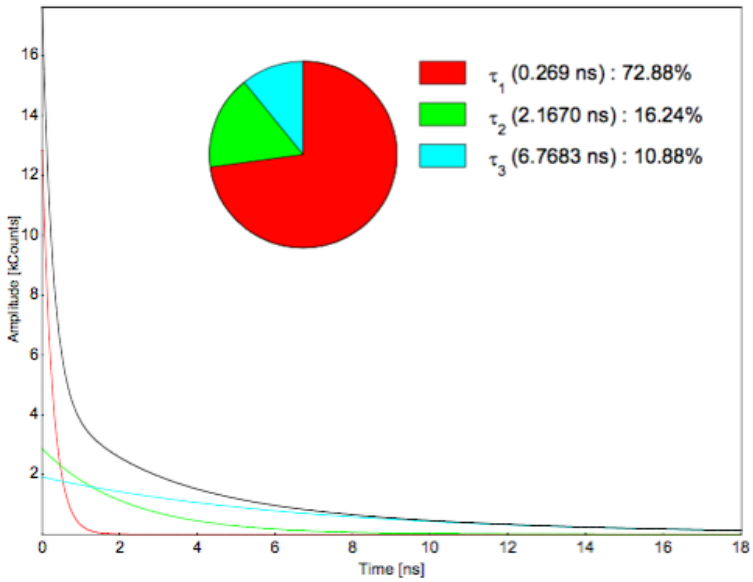

Figure 3.25. Exponential fit on NBD-ChA/HNaphC 1mM pH 11.50 solution (molar ratio 1:250) performed with software FluoFit on a TCSPC curve. Each color is associated to a population of fluorescence emission events, from the faster (red, polar micro-environment) to the slower (cyano, non-polar micro-environment).

τ_2 and τ_3 suggest that the minority of the probe molecules feel a different micro-environment as the relaxation time is more than one order of magnitude bigger, which means that in this case probe was incorporated in hydrophobic domains of tubular supramolecular structures. As the decays are basically two, it is legit to think that two are the binding conditions in which the probe was interacting with the packed HNaphC molecules but no further information can be addressed to this hypothesis.

3.6.3 CSLM Imaging on Supracolloidal Fluorescent Frameworks

Even if both quantum yield of conjugated NBD derivative and its incorporation percentage inside supramolecular tubules were lower than the expected, confocal microscopy imaging performed on M+/NBD-ChA/HNaphC mixures produced images very appealing to the eye. To successfully perform the measurements, the technological differences between the fluorimeter and the confocal in terms of sensitivity to the fluorescence emission, and the SNR were taken into account. In fact, even though CSLM PMTs (photomultipliers) are a very performing detection instrument, the measurement conditions were constraining the range of probe concentration possible, so that was necessary to increase probe concentration by factor 10 in order to achieve a good emission from the probe within the aggregates. Moreover, SNR was affected by the noisy background visible in the fluorescence PMT1 channel of the confocal

microscope, since, as remarked previously, a big amount of labeled molecules was in solution and not packed inside the aggregates. To increase SNR, gain was increased to 200 V and offset lowered to -20. Detector slider was then optimized to eliminate the noisy background refining the window of signal detection. Seldom, a mathematic polishing of the background was then performed afterwards. Results are presented in the following figures. Again, keeping the tubules number density in large excess with respect to the microgels was possible to direct the co-assembly towards the formation of core-corona particles as shown in the montage of Figure 3.26.

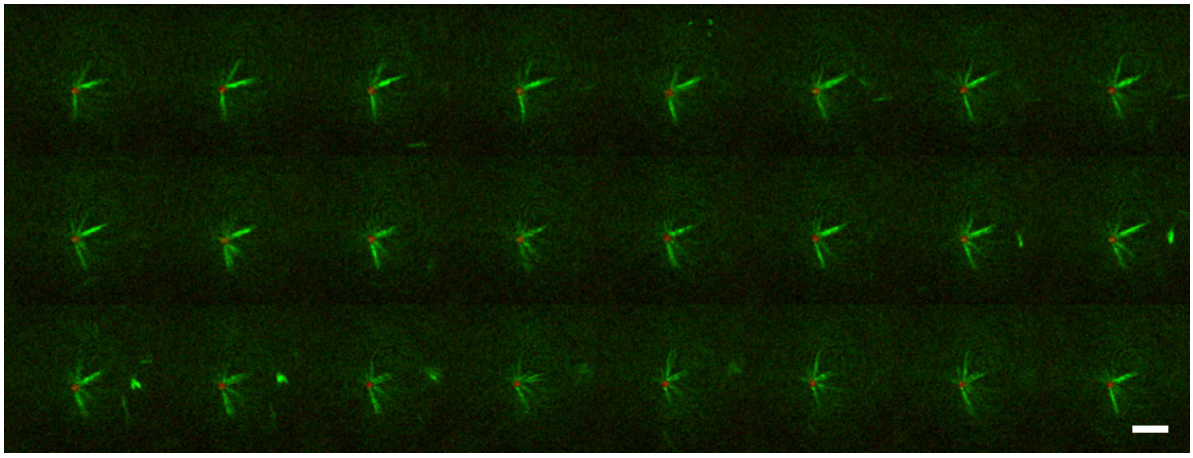

Figure 3.26. Time sequence (5 secs) acquired through CSLM in combination of both green and red fluorescence modes, of a core-corona assembly in rotational motion. The microgel-core is red because of the TRITC emission, while the tubules are green for the NBD-ChA probe within (or bound to) the supramolecular HNaphC packing (scale bar: 5 μm).

Since tubular scrolls suffered from discrete polydispersity cluster assemblies were more seldom observable but still, after some time, couples triplets and then more complex colloidal molecules arise as stable dispersion in solution (Figure 3.27b, f, j). Increasing microgels weight fraction allowed for network formation, which didn't show any regularity and then no *g(r)* could have been extracted. Was already stressed that tubular length polydispersity enormously affects the structural features of network. In the case of NBD-ChA/HNaphC mixtures was likely that the presence of the probe embedded in the supramolecular structure partially hindered the adsorption of the microgels to the tubular extremity. In facts, very often were observed single microgels with one or two tubules bound, meaning that the interaction suffered because of the presence of the fluorescent probe. A less marked ability of the network to spread three-dimensionally, with respect to the same structures not provided with the probe, can be deducted from Figures 3.28 and 3.29. However the network had the same stability over time (24 h).

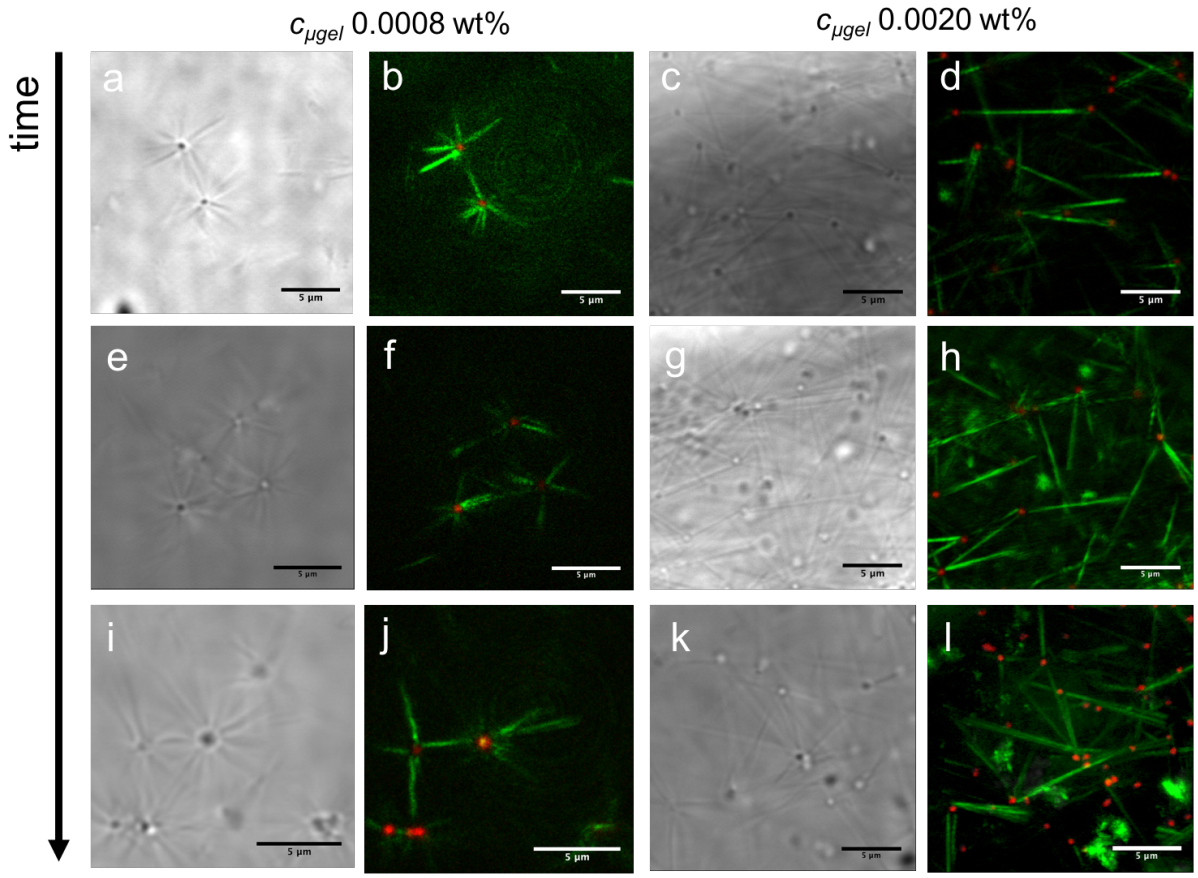

Figure 3.27. CSLM micrographs shown as transmission mode (a, c, e, g, i and l) and fluorescence mode as superimposition of TRITC (red) and NBDChA (green) emissions (b, d, f, h, k and m). When $c_{\mu gel}$ is kept at 0.0008 wt% core-corona particles assemble in clusters of 3-4 particles while at higher concentration ($c_{\mu gel}$ = 0.0020wt%) produces disordered, but full-spanning networks.

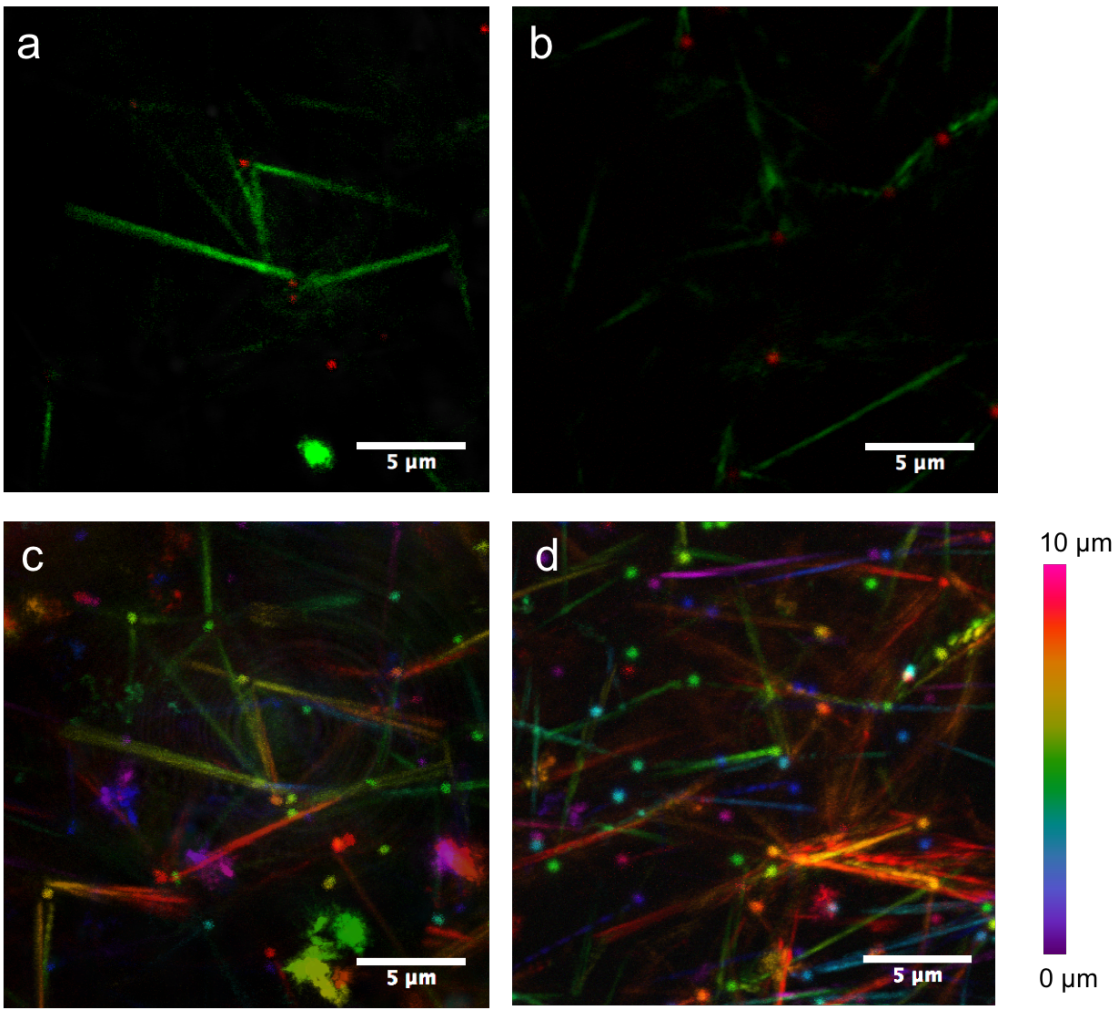

Figure 3.28. CSLM micrographs reported as superimposition of red (TRITC) and green (NBD-ChA) fluorescence modes (a, b) and corresponding orthogonal projection of color-coded *z*-stacks acquisitions of an NDB-ChA/HNaphC 1:100 mixture with M+ microgels. (c_{tot} = 2mM, $c_{\mu gel}$ = 0.0020wt%)

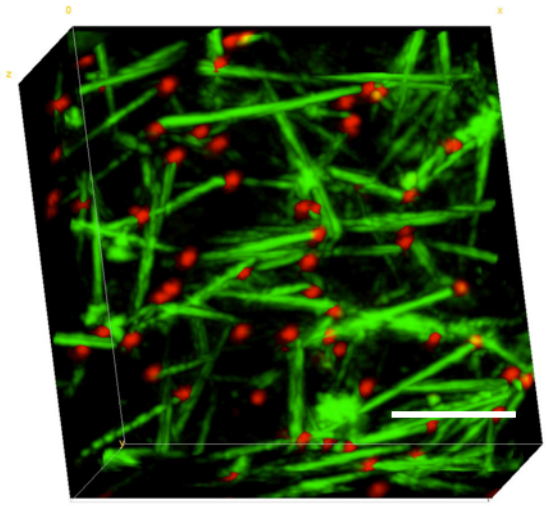

Figure 3.29. CSLM 3D reconstruction of a *z*-stack acquired on 2mM NBD-ChA/HNaphC 1:100 mixture with M+ microgels ($c_{\mu gel}$ = 0.0020wt%).

3.7 Discussion

The above reported experiments proved the formation of different self-organized frameworks in each case characterized by extreme hierarchical order as result of the unique specificity of interaction between various spherical particles and anisotropic HNaphC supramolecular tubules. As a very general trend, when spherical microgels based systems were mixed with HNaphC dispersion of tubules at pH 11.50, a strong interaction between the spherical surface of the particle and the tip of the scrolled tubules occurred. Taking into account each experiment performed, several observations can be made to highlight the most important features of the system. Before all, thanks to the highly narrow distribution of lengths, the multi-walled scroll-like HNaphC tubular structure seems to be the ideal candidate for the role of anisotropic colloidal linker for particle bridging and bottom-up directed framework formation. Besides, the co-assembly features of the frameworks here described seems to have some aspects in common with what observed between microgels and tubules from pure ACD – ACD/CCD catanionic mixtures reported in Chapter 2, still considering the relevant differences regarding the interaction specificity. When spherical particles weight fraction is really low, core-corona assemblies form, manifesting a natural predisposition to the formation of hierarchical clusters with time as presented in Figure 3.2. What can be easily deduced is a certain similarity with the images reported in Figure 2.1a-c (see Chapter 2). Differently from the latter case, where the clusters were the result of a rather disordered aggregation due to uncontrolled depletion phenomena, these clusters are smaller in size, less dense thanks to the higher spacing imparted by the higher tubular length, very ordered and rigidly arranged with rather precise entanglement angles (dependent from microgels hydrodynamic radius) among the spherical colloidal units, directly depending on the size of the core and on the length of the scrolls interconnecting the microgels. Surprisingly, these core-corona assemblies seem to have a controlled but fast reactivity as the formation of clusters took place in a time span between 1 and 1.5 h.

Remarkably, these frameworks may be considered as a stick and ball model of molecules where the directional bonds are represented by the tubules while the atoms are represented by particles (see the glucose “chair-like” structure in Figure 3.2h). Diffusion and size of these core-corona assembly was impossible to characterize correctly through scattering techniques in solution because of the big size of the particles and of the presence of unattached anisotropic aggregates visibly complicating the measurements. To investigate the diffusion behavior in diffusive regime, MSD was performed starting from CSLM images analysis. Finally, two main features

could be highlighted. The first is that, in the same boundary conditions, like BSD concentration and microgels number density, diffusion depends strictly on the size of the core, meaning that assemblies with bigger cores have slower diffusion, caused by the higher resistance to the motion through the medium. Consequently, was found that self-diffusion coefficients decreased as the core of the assembly increased in hydrodynamic radius.

The second concerns the fact that concentration has a big impact on the framework morphology. Increasing the microgels weight fraction up to values suitable for the units to interconnect, a three dimensional full spanning network form, with relevant spatial order. However, the attaching angles between the scrolls on the spherical surface, and their number, seem to be preserved regardless the concentration, whereas the angle increased and number decreased as hydrodynamic radius of the core decreased.

The abundancy of free unattached tubules suspended in the medium very quickly decreases with time as the core-corona are interacting and gathering thanks to the great reactivity of the tip binding-site, meaning that at sufficiently high microgels concentrations ($c_{\mu gel} = 0.0020$ wt%) no free scrolls are observed and all of them are employed in the interaction with microgels. At this microgel fraction the framework occurs and from CSLM images it is possible to extract *g(r)* to better characterize networks features. From 1 to 3 peaks at 1, 7 and 15 μm, were obtained in the *g(r)* of the M+ based, thus highlighting the ability of the M+ based system to give stable 3D supracolloidal networks with local- and medium-range orders. This feature is directly related to core size: considering a fixed perpendicular adsorption of the tubule on the surface, a bigger spherical particle implies more entanglement angles possible between the units (more disordered arrangement) while a very small core implies less degrees of freedom, less and wider entanglement angles accessible among the units and in turn more ordered frameworks. Beside these considerations, as proved by *g(r)* data elaboration, it seems that M+ based system represents the *optimum* in this respect, consisting in a proper balance of diverse conditions like the ratio between the scroll cross section and the microgel size, the charges of the colloidal species involved, and the tubular length. However, a completely ordered lattice was not achieved in the first place for the fluid and non-covalent nature of the framework as well as for the geometry of the single unit. Through CSLM was possible to measure, and statistically average, the angle described by two adjacent tubules adsorbed on the microgels surface, when the network was formed. This angle ranged between 60° and 70° which in turn is relatable with a 5- and 6-fold geometries of the single core-corona unit. Of course the pentagonal geometry of the elementary unit is not consistent with a regular three-dimensional lattice.

By further increasing stepwise the concentration of microgels, more tubules were busy in inter-particle bridging as more of them were solicited to leave the microgels surface resulting in disorder increase throughout the framework. Interestingly, the increase in microgels concentration didn't exalted any presence of a secondary binding site on the scrolls as, instead, proven in the mixtures studied in Chapter 2. In this case no secundary binding site on the tubular surface could be observed. At very high microgels weight fractions ($c_{\mu gel}$ = 0.05 wt%) network disconnected and clusters of microgels were visibly attached at the tubular tips, meaning that microgels-microgels interaction was more favored with respect to microgels-secundary binding site interactions (Figure 3.6). Taking into account all these experiments performed, one thing can be stressed about scroll reactivity: considering both mixtures at the lowest and the highest microgels concentration investigated, no dumbbells were ever observed, (*i.e.* couples of microgels interconnected by a tubule) and, additionally, even the favored formation of core-corona units at low microgels weight fractions proved how scrolls have most likely an asymmetry of tips reactivity or, in other words, a tip more reactive than the other one. This could explain the core-corona assembly formation, the absence of dumbbells at the highest microgels concentration, the slow kinetics of cluster formation with respect to the very fast kinetics of core-corona assembly formation. This latter observation indeed takes into account that the slow diffusion of the different core-corona units heavily affects the kinetics of their interaction. It is in any case evident how really near core-corona units struggle to cluster and the adsorption of a tubule which has already one of its tips adsorbed on the microgels surface seems to be less favored (slow process) with respect of that of free tubules on microgels surface (fast process). Moreover, the complete absence of any surface-directed decoration pattern on the tubules indeed comes from reasons strictly related to the scrolls structural appearance. As mentioned in the first part of this Chapter, HNaphC fresh tubules kept at pH 11.50 are basically couples of twin tubules folded in a scroll-like fashion as found by cryo-TEM images (see Figure 1.15 Chapter 1). This implies that tubules offer a smooth surface towards the solvent on a side and a linear tight groove on the other, in both cases polar heads of the packed bile salt derivative are most likely directed towards the solvent, as the aggregate is proven to be highly negatively charged from dielectrophoretic measurements (-50 mV). This could in turn imply two aspects about the impossibility of the microgels to bind the linear groove: the first could be the unequal proportion between the radius of the microgels and the spacing of the linear groove which is too small to accommodate a surface with a rather low curvature (~600-700 nm particle diameter vs. few tenth of nanometers of the linear rim width), the second could be related to the surface charge. In the linear groove a higher charge density should be present and available for

electrostatic interaction with oppositely charged microgels. Absence of any interaction microgels-linear rim could testify the very low contribution of the electrostatics to the overall interaction mechanism in this specific system.

Interestingly, to an opposite conclusion we may be driven considering parallel experiments carried out with mature (1 week old) HNaphC tubules and M+ microgels. Performing CSLM on mixture samples at increasing microgels concentrations, as reported in Figure 3.30, was observed the same interaction mechanisms reported in Chapter 2 when interaction of microgels was studied with respect to anionic ACDtubules. As shown in Figure 3.30 the interaction is different when the scroll dispersions are aged. In fact, mature, big sized HNaphC elongated structures are formed by aging and interactions of the microgels with the tips and along the structure lateral surface seemed to occur, thus highlighting two binding sites on the BSD aggregate. By progressively increasing the microgel fraction, M+ microgels first adsorbed to the tips and then on the tubules outer surface, up to a complete covering of the surface when microgels weight fraction was increased up to 0.05wt%. Twisted ribbon structures highlighted in a previous paper on HNaphC self-assembly[97] can be recognized on the images on which an helical arrangement of the microgels occurs (Figure 3.30k-l).

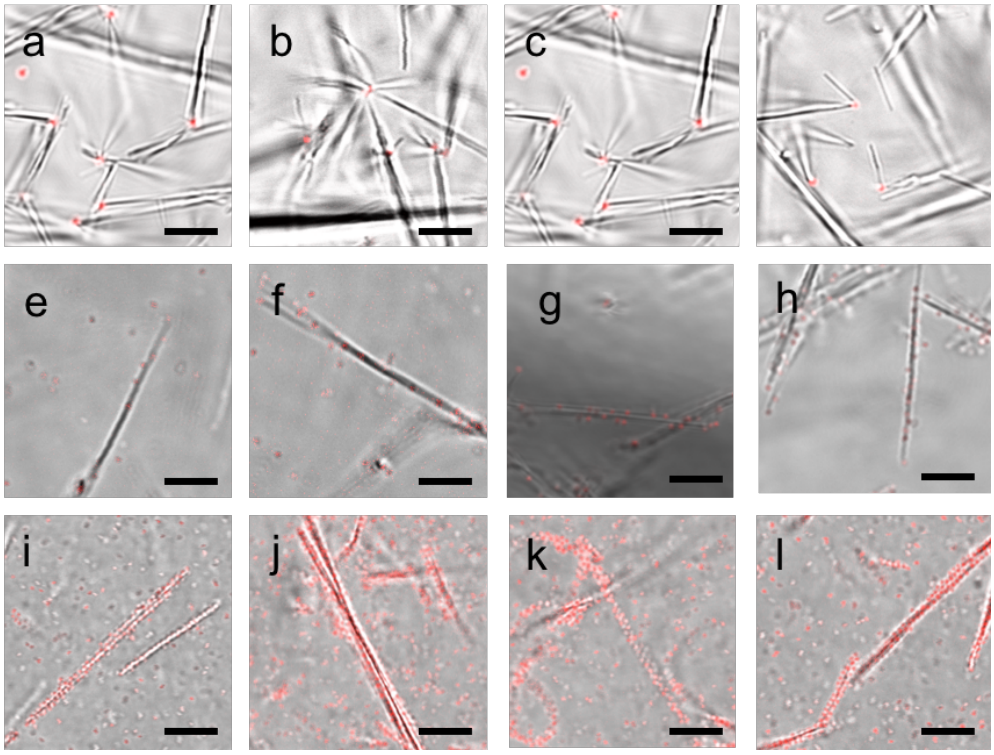

Figure 3.30. CSLM micrographs reported as superimposition of transmission and fluorescence modes of mixtures of HNaphC (1 w old sample) and M+ microgels with progressive increasing concentrations : 0.0020wt% (a-d), 0.0040 wt% (e-h) and 0.05wt% then diluted x2 times to clean the background from not adsorbed microgels (i-l). Scale bar 5μm.

Concerning network formation kinetics, DLS measurements showed a slow trend that brought initial core-corona units to gather in hierarchical ordered three-dimensonal sphere-tubule networks. Specifically, was found that the whole time that a M+ core-corona assembly needs to form the ordered network seems to be around 210' as the TCF intercept with the ordinate was observed to decrease, and decay time to increase, proving the stepwise reduction of microgels diffusion. On the other hand, the tubules-microgels mixture has, at $t = 0$, a decay time much longer than that of the pure microgels suspension meaning that the core-corona formation takes place instantly as soon the mixture is prepared. These experimental results, together with CSLM data, could bring us to the conclusion that the formation of big sized clusters it's a process slower than core-corona unit formation but still faster than the interaction among those clusters and their gradual increase of order and homogeneity toward the framework formation, which is a really slow process. The supracolloidal three-dimensional framework always exhibited a strict temperature dependence. Rising temperature from 20°C to 30°C was observed to be detrimental for the network stability, mostly for the unstable structural integrity of the supramolecular HNaphC scrolls when temperature is increased. However, performing up to three cycles of heating and cooling in a temperature range chosen between 20° and 50°C, it was possible to disaggregate and re-aggregate the initial 3D ordered network, regardless the phase separation of both PNIPMAM or PNIPAM microgels, which thermo-responsivity is well known to be characterized by a VPT around 32°C (above which structural collapse of the microgels usually occurs), and HNaphC supramolecular tubules which at temperature higher than 30-40°C disaggregate forming a suspension of colloidal sized amorphous particles. However, it must be considered that the *g(r)* before and after the heating looks different as the final networks had no medium range and really low short range orders. This could be explained thinking that the heating on a metastable and consequently not mature state of aggregation of the tubules has an annealing effect, enhancing the secundary nucleation and forming scrolls actually longer, slightly thicker (increased contrast at CSLM was observed) and less monodispersed with respect to the pH induced self-assembly. For sure the pH induced nucleation process is far more controllable with respect to the temperature induced one. Another factor to take into account is the local aggregation of the microgels during the phase separation which could lead to hindered re-dispersion upon cooling, meaning that inhomogeneities during the network reformation can easily arise and have a huge impact on the *g(r)*.

The inclusion of a NBD-labeled derivative within the HNaphC supramolecular aggregates, allowed for the major recognition of the scrolls during CSLM analyses. Performed fluorescence characterization in steady state and in time resolved conditions proved how the compound was

actually packed inside the folded BSDs bilayer. The extraction of the decay times from the TSCP measurements could unveil the partial, but still sufficient for the aim of this study, inclusion of the probe inside the aggregates while the remaining part was present as monomer not packed inside the tubules. CSLM performed on mixtures of NBD-ChA/HNaphC and microgels M+ proved again how varying boundary conditions, as type or composition of tubules and/or type or composition of the microgels, the supracolloidal assembly pathway towards network formation was unvaried. Core-corona assemblies were the product of the interaction of microgels with a high excess of tubules. Diffusion of the core-corona units through the medium produced the formation of clusters of colloidal molecules. When the number densities of microgels and tubules were roughly comparable a network was observed but to a less remarkable extent because of the uncomplete packing of the tubules on the microgels surface most likely due to different supramolecular morphology of the NBD-Cha / HNaphC tubules. Furthermore, the peculiar adsorption of the tubules on the microgels surfaces was highlighted by the probe presence and it will be rationalized and discussed in Chapter 5. It was unveiled how tubules can adsorb either perpendicularly to the microgels surface either tangentially with consequentially two different binding energies. This could be due to the different tips of the singular scroll having a side convex and a side concave so that the convex side has small frontal area to bind the microgels but high lateral area (for the presence of the elicoidal external rims) while when the concave approaches the microgels offers a convenient binding size in term of contact area (for the ideal radii ratio) but no lateral surface because the elicoidal rim are on the internal surface of the tubule.

3.8 Conclusions

Herein was demonstrated how supramolecular tubules of HNaphC are able to co-assemble in a controlled manner with polymeric PNIPAM and PNIPMAM microgels-based systems, building diverse and precise supracolloidal frameworks. Supramolecular HNaphC tubules are the result of the folding of supramolecular sheets in twin scrolls, obtained through self-assembly at alkaline pH values (pH 11.50). Spontaneously, the microgels adsorb directly to the most reactive tip of the tubules determining the formation of core-corona assemblies, which can entangle in a gradually more expanded networks as time and microgels weight percent are increased, providing a framework having both supramolecular and supracolloidal nature. This kind of trend not only resembles the microgels / BSD tubules system studied and reported in Chapter 2, but consists in its implementation. Particularly interesting were the supracolloidal

three-dimensional frameworks as was proven by their continuous connectivity throughout the sample, by the strength of the interaction (enough to prevent the collapse of the structure on itself), and finally on the rather high short- and medium-range order of the network, reached thanks to the ability of the tubular structure to work like spacers among the microgels. The possibility to exploit this features for further applications is certainly feasible. The implemented interaction established could be inspiring in terms of modeling novel surfactant-based supracolloidal frameworks, opening the path for the hypothetical preparation of mesoscale scaffolds acting as bridging framework between sub-micrometer templating surfaces and biopolymeric mesoporous and microporous materials.

4 PNIPAM colloidal crystals formation by depletion interaction and percolation in a BSD hydrogel matrix

4.1 Chapter rationale

Yablonovitch and John[112,113] pioneered the study of PhCs more than 20 years ago, triggering the interest of the whole material science community. Stimulated by the numerous examples of photonic band gap (PBG) materials in nature, different preparation pathways have been investigated, through both top-down and bottom-up approaches.[36]As mentioned in the introduction chapter, the bottom-up approach is gradually transforming the panorama of the whole field of research, bringing to better and more straightforward protocols to build applicable colloidal crystals with intriguing PBG properties. In this chapter detailed information on the preparation of a PNIPAM microgels colloidal crystals suspended in a gel matrix (an example of self-assembled fibrillar network or SAFIN) will be given. These colloidal crystals are the result of a combination of depletion interaction and segregation effect induced by the self-assembly of ACD in fibrils. Besides, even though this type of crystals doesn't show any photonic behavior mainly because of the size of the particles and their refractive index (which are not suitable for the preparation of PBG-based systems), however, the work could be interpreted as a pilot study intended to give some insights on the preparation of hypothetical photonic crystals of a dispersion of particles in a surfactant solution, whom the formation is triggered by the unidirectional growth of surfactant micelles. CSLM was performed to follow the kinetic of crystal nucleation from early to the final stages, monitoring the effect of microgels weight fraction on the crystalline domains features. ACD fibrils were analyzed through cryo-TEM for a proper characterization at the nanometer scale; although, no kinetics of the fibril growth could be imaged as too fast for the experimental techniques used.

4.2 PNIPMAM microgels colloidal crystals in ACD hydrogel matrix

To induce colloidal crystal formation a protocol was defined to standardize the samples preparation. A 2 mM solution of the BSD ACD was prepared at pH 9.5 using a 30mM $Na_2CO_3/NaHCO_3$ buffer in order to induce supramolecular aggregation of the surfactant into fibrils. Visibly, the solution was increasing its viscosity until a gel was formed. Mixing the

microgels particles at this stage would have been critical as the presence of the fibrillar matrix would have hindered the fast diffusion of the particles across the solution. To bypass this problem, the solution was heated up for 1 hour in a ventilated oven at 70°C in order to disaggregate the fibrils. Successively, an aliquot of 200 μl was transferred into a vial kept at 20°C and mixed, under gentile stirring, with a buffered suspension of homogeneous M+ microgels (15mM $Na_2CO_3/NaHCO_3$). The effect of microgels concentration on colloidal crystal formation was investigated preparing series of samples with different $c_{\mu gel}$ keeping constant both the BSD and the buffer concentrations.

Respecting the protocol already described in the previous paragraph, the samples were prepared mixing respectively 0.2 wt%, 0.5 wt%, 1 wt% and 1.5 wt% microgels particles. Few seconds after the mixing a drop of the sample was each time transferred using a spoon on a microscopy glass slide and analyzed in a temperature controlled environment containing the microscope, set at 20°C. Any use of pipettes or syringes was avoided to get rid of shearing effects due to the flow of the dispersion through the needle.

CSLM was performed on each sample for a range of time variable depending on the aggregation state of the specimen. In principle for each concentration the depletion interaction was found to be effective during the first 30 minutes. Independently from the microgels concentration used, well separated particles were found to dynamically interact, moving from a bunch to another one adjacent and rearrange to lower the energy at polymer/water interface. However, after the first half an hour samples with low concentration showed extreme difficulty to form ordered crystals. The sample with $c_{\mu gel}$ = 0.2 wt% didn't show any crystalline aggregates revealing how the concentration threshold for crystal formation should in general fall between 0.2wt% and 0.5wt%. After the fibrils were completely formed depletion interaction started to decrease sensibly in strength, towards negligible levels. The low concentration was not sufficient to guarantee enough microgels to percolate among the fibrils, the assembly process stopped after 2 hours and stabilized in a suspension. The sample with $c_{\mu gel}$ = 0.5wt% seemed to be characterized in a slightly different way in terms of co-assembly behavior: after the depletion stopped, assembly process was continuing to bring particles in bunches having rather low lattice regularity; moreover, aggregates seemed to be homogeneously dispersed across all the volume investigated. Even though the increment in size was still perceptible after 2 h, the clusters were showing only seldom an ordered packing, (Figure 4.1b, f, j) with a few traces of crystalline packings visible. Increasing $c_{\mu gel}$ up to 1wt% several interesting features were observed. Given the relatively high microgels concentration the depletion was strongly favored bringing towards the formation of jammed disordered arrays of microgels in short times (less than 15 minutes).

Contemporarily, the arrangement process of the microgels was also favored and from the first 30 minutes on, the majority of the clusters were under the form of crystalline lattices. Furthermore, colloidal crystalline clusters were joining in expanded crystalline domains with different degrees of crystallinity. After two hours, due to the high microgels concentration, the whole system was undergoing a spinodal decomposition where a progressive demixing[114] brought to a compresence of an amorphous phase (fibrillar phase) and a crystalline phase (microgels phase). This kind of mechanism has been abundantly investigated and observed in colloidal systems of soft spheres and hard rods[115] separately.

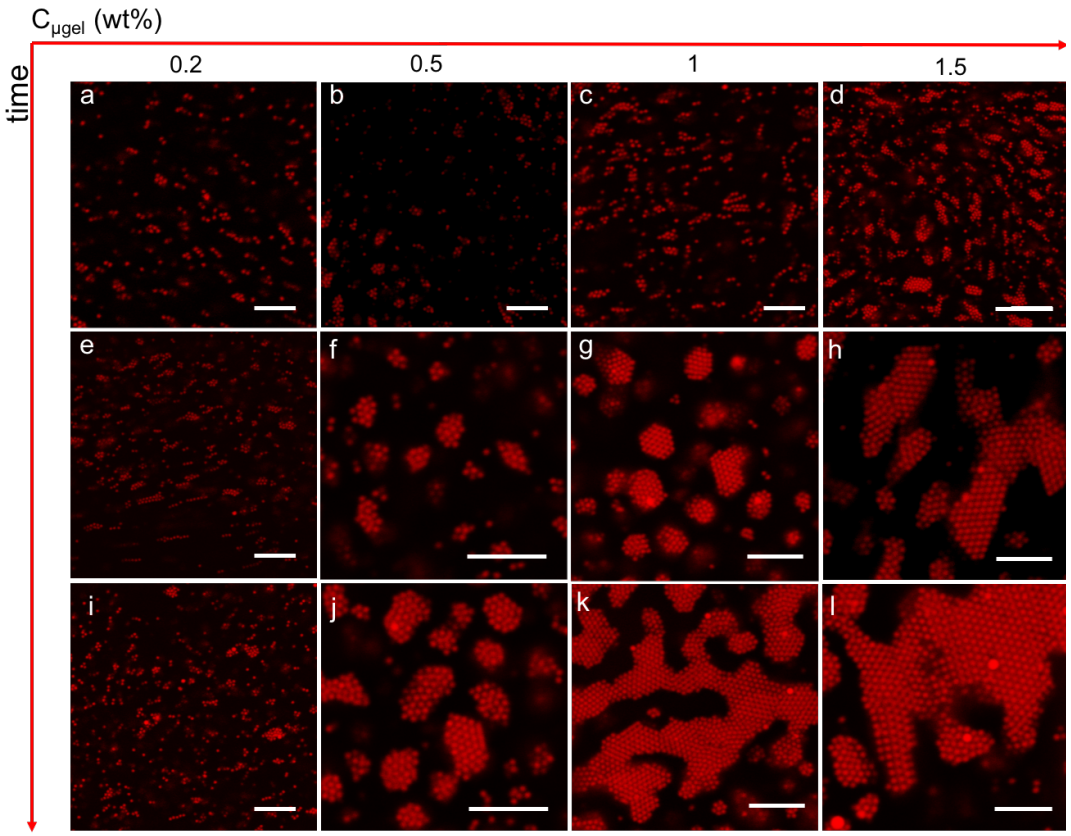

Figure 4.1. CSLM micrographs iof M+ microgels mixed with ACD 2mM in 30 mM Na_2CO_3/$NaHCO_3$ buffer solution. The concentration of microgels increases following the values reported above the upper red arrow (scale bar 10 μm).

CSLM experiments were also carried out to characterize the kinetics of colloidal crystals formation, followed by *g(r)* extimation, from CSLM data. The *g(r)* were calculated analyzing images related to several colloidal crystals imaged at the same stage, and then averaging the resulting radial distribution functions. The results are reported in Figure 4.2, in the inset a CSLM micrograph taken from the sample in analysis is also reported.

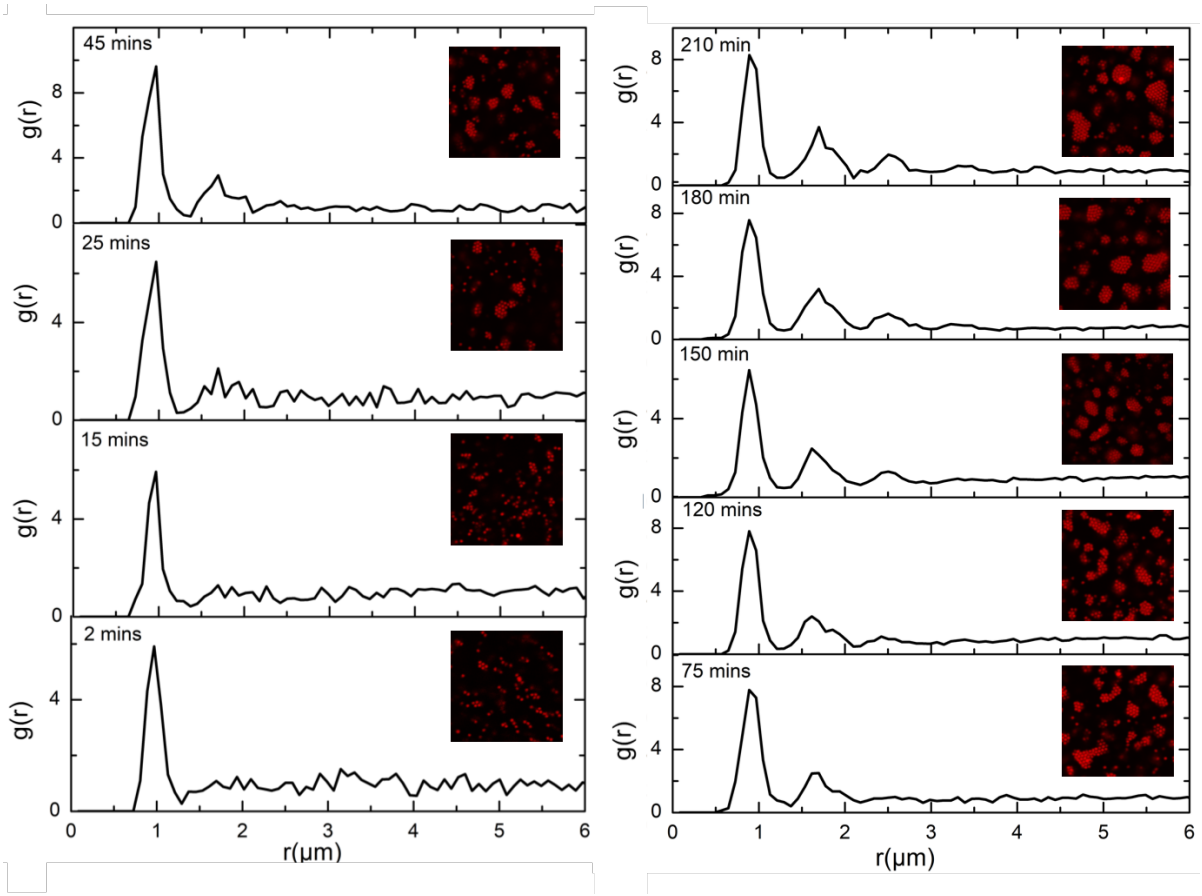

Figure 4.2. *G(r)* extracted from statistically averaged *z*-stacks of a microgels suspension in a NatBuPhC solution. (c_{ACD}= 2mM, $c_{\mu gel}$ = 0.5wt%, c_{buffer} = 30 mM). In the insets are represented purely informative CSLM micrographs of the fluorescence channel of the microscope related to the sample during the corresponding stage of growth.

The *g(r)* calculation didn't show any peak at concentration of microgels below 0.5 wt%, demonstrating the inability of the system to generate colloidal crystals. In the case of 0.5wt% mixture small colloidal crystals can be observed, resulting from a rather low kinetics of formation. The system, initially characterized by the presence of microgels far from each other, turns in a suspension of aggregated microgels clusters in 25-30 minutes, when the second peak starts to arise on the *g(r)* function (Figure 4.2). The complete process took 210 minutes to complete (after which no relevant evolution was observed) and a maximum of 3 sharp peaks were observed.

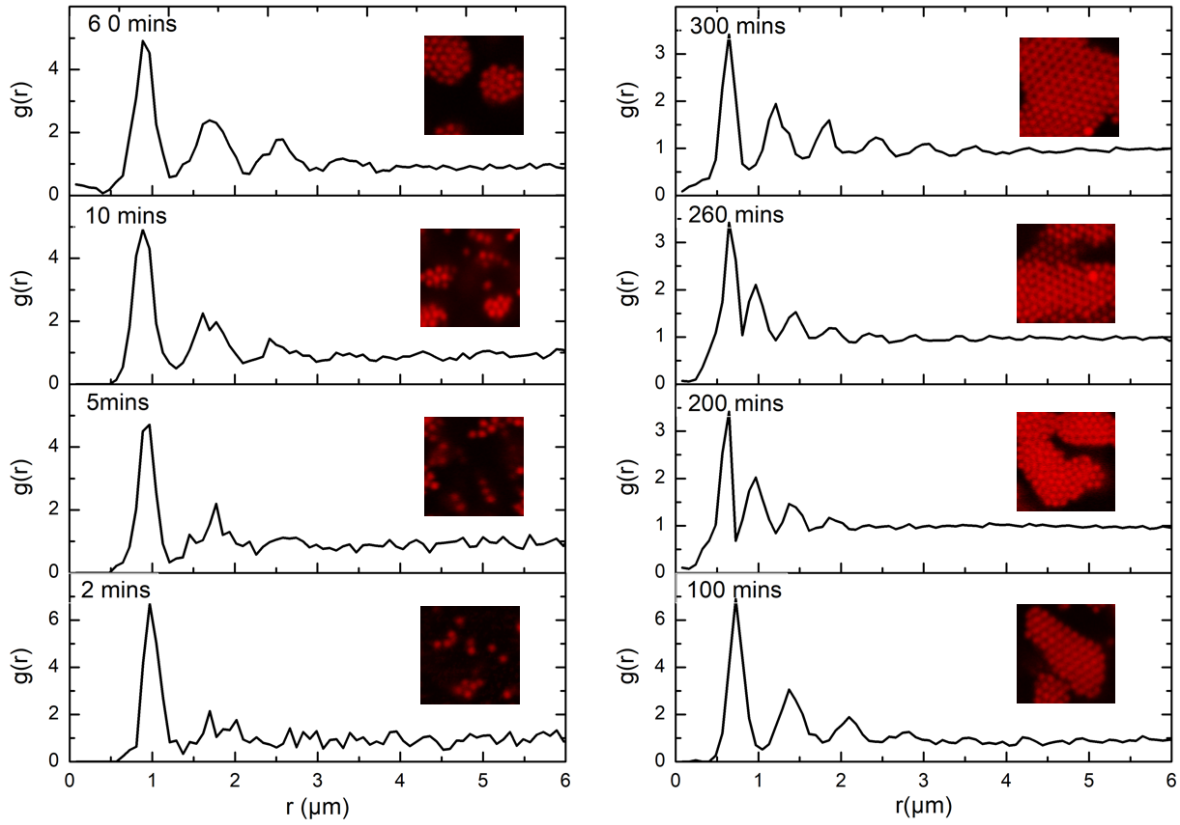

Figure 4.3. *G(r)* extracted from statistically averaged *z*-stacks of a microgels suspension in a NatBuPhC solution. (c_{ACD}= 2mM, $c_{\mu gel}$ = 1wt%, c_{buffer}= 30 mM). In the insets are represented purely informative CSLM micrographs of the fluorescence channel of the microscope related to the sample during the corresponding stage of growth.

Results reported in Figure 4.3, regarding the sample at $c_{\mu gel}$ = 1 wt%, show how the system turned into a dispersion of colloidal 3D crystals and self-organized within crystalline domains with short, medium and long range orders already within 60 minutes. The formation of the crystals was the result of rather complex combined processes. The starting system composed from BSD micelles rapidly underwent a *sphere-to-rod* transition when internal temperature started to decrease progressively towards 20°C. PNIPMAM microgels are known to have a VPT temperature above 32°C meaning that, during the first few minutes of the experiment, most likely a great amount of microgels should have been present in the collapsed state, undergoing a phase separation from the BSD solution. However, through confocal microscopy performed during the same lapse of time, thanks to the *ad hoc* preparation protocol adopted, no signs of phase separation or undesired aggregation were found near the glass level nor several tenth of microns inside the specimen (*i.e.* not during the measurement), and hence no detrimental inhomogeneous heat distribution phenomena occurred as microgels were locally protected by the high temperature gradient within the solvent. At the same time at $t = 0$ particles were in moderated Brownian motion, because of the low viscosity environment due to the low presence of elongated and/or entangled fibrils. At t = 0 the corresponding *g(r)* shows one

correlation peak consistent with the first neighbors distance and, in facts, with the diameter of a single microgel, as actually clusters of few particles were present already. In the solution, furthermore considering presence of the buffer and monomeric BSD charged molecules are present that could interact with the microgels and neutralize their charge, thus reducing the stability of the microgel dispersion. This could address for their initial and unavoidable clustering in bunches of several particles. Visibly as the time increases the number of peaks increases towards a crystalline *g(r)* with a medium-long range orders. From t = 100 minutes on, 2D crystals were starting to layer on top of each other forming three dimensional colloidal crystals. After approximately 300 minutes the whole system stabilized and no more changes in the *g(r)* were observed. The first peak position reached at t = 300 mins is abundantly below 1 μm and is slightly longer that maximum hydrodynamic radius of microgels in swollen state, which is in agreement with values reported in literature for PNIPAM microgels found in crystalline domains. The number of bumps of the *g(r)* function corresponds to the most abundant reciprocal distances found within the colloidal lattices, and they increase from 0 to a maximum of 7-8 following the kinetic of crystals formation. As soft particles, microgels tend to vary their inter-particle distance in a manner dependent on the number density of the particles (number of particles per μm^3). Moreover, as different works have proved, the type of crystalline lattice is strongly related to the inter-particle distance found. To investigate the inter-particle distance in our samples, a center-to-center distance d_{ctc} was extracted from *g(r)* first peak position, and plotted as a function of time (Figure 4.4). Predictably, the center-to-center distance decreases with increasing time as a result of the progressive packing of the microgels to form crystalline domains. The minimum falls at t = 200 mins where d_{ctc} was found to be around 0.64 μm hence smaller than the particle diameter in agreement with litterature.[116] From t = 200 mins a plateau is reached, indicating that the local packing was not changing anymore with time. However, the number and position of the bumps in the *g(r)* function slightly change between t = 200 and t = 300, probably because of further lattice rearrangements happened at all length scale.

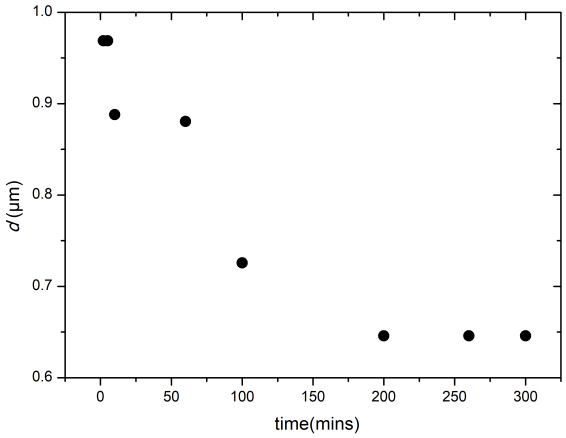

Figure 4.4. Center-to-center distance (d_{ctc}) extracted from *g(r)* first peak position and represented as a function of time, following CSLM data.

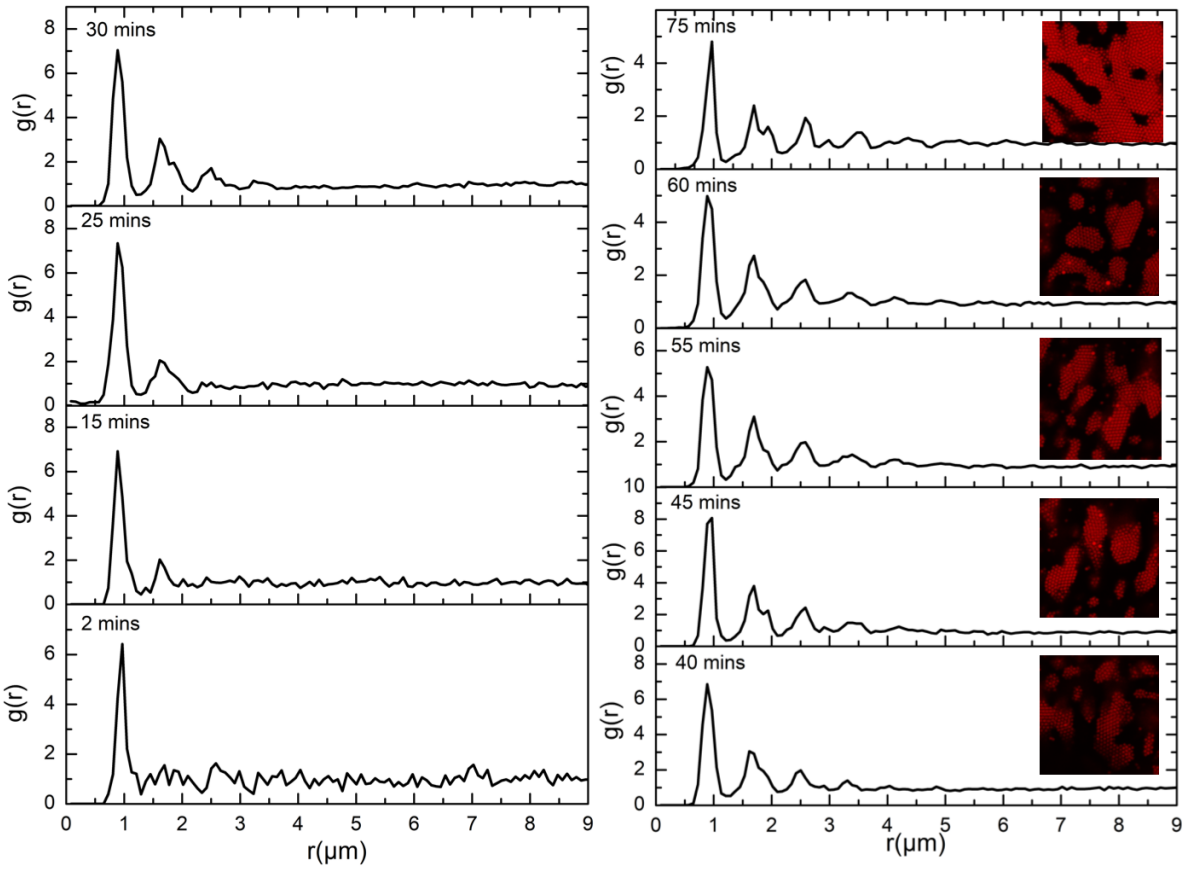

Figure 4.5. *G(r)* extracted from statistically averaged z-stacks of a microgels suspension in a ACD solution. (c_{ACD} = 2mM, $c_{\mu gel}$ = 1.5 wt%, c_{buffer} = 30 mM). In the insets are represented purely informative CSLM micrographs of the fluorescence channel of the microscope related to the sample during the corresponding stage of growth.

Finally, a sample with $c_{\mu gel}$= 1.5wt% was studied. In this case the high concentration of microgels implied a fast kinetics of formation of the crystals as extended domains were already formed and ordered in 40 minutes. From 40 minutes on, interestingly, the crystallinity of the lattice increased to a less marked extent with respect to the 1 wt% sample. In principle this could be explained hypothesizing that the faster the kinetics of supracolloidal aggregation, the

shorter the time available for the microgels to rearrange in an ordered fashion before other microgels pack on their surface. This could address for the lower degree of crystallinity within the supracolloidal crystals domain.

A closer look to the *g(r)* between 45 and 75 minutes denotes how some peaks are actually couples of overlapped peaks (*e.g.* 75 mins: peak @ 1.6 μm, peak @ 1.9 μm).

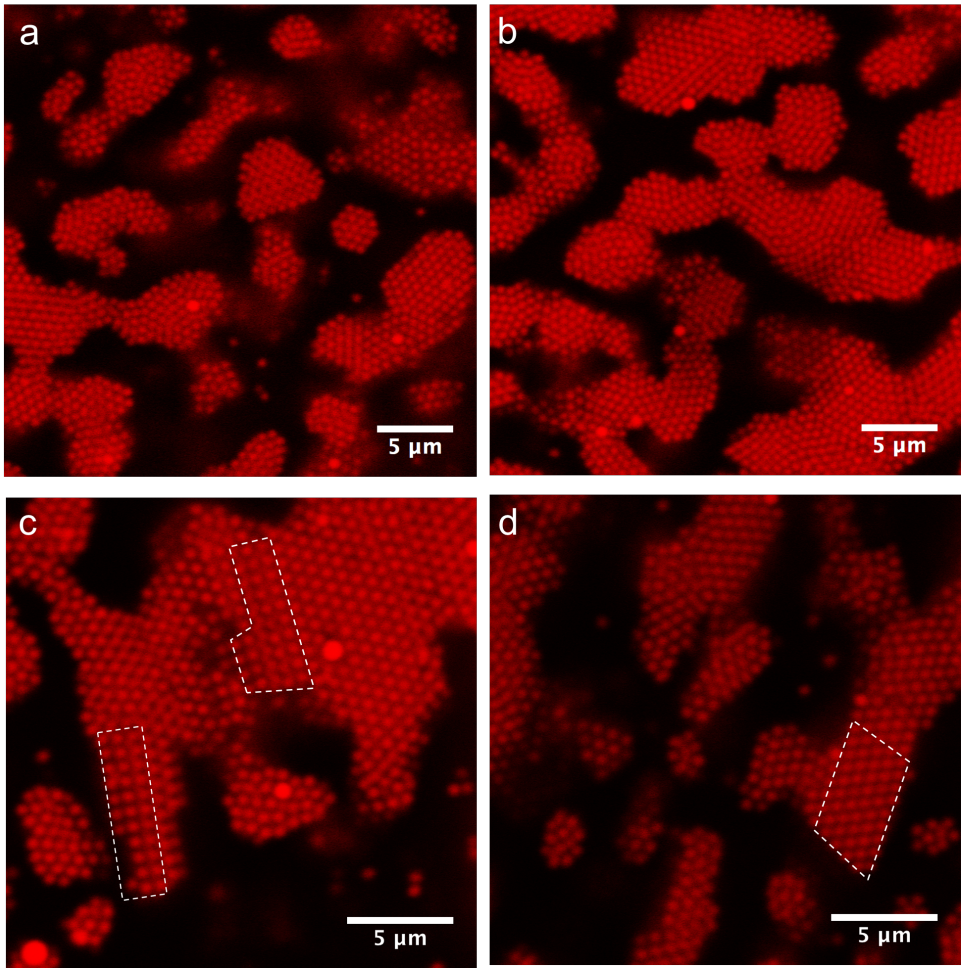

Figure 4.6. CSLM micrographs of the fluorescent emission of PNIPMAM microgels assembled in crystalline domains in mixtures with Cμgel=1 wt% (a, b) and Cμgel = 1.5 wt% (c, d).

This means that at concentrations above 1 wt%, the principal 6-folds symmetry, likely FCC or HCP for "soft spheres",[117–119] could be accompanied by other crystalline forms with a 4-folds symmetry which were found to be seldom distributed along the edges of the 6-folds domains. Plotting d_{ctc} as a function of time for the three samples analyzed allows us to summarize the behavior of the mixtures (Figure 4.7). The sample with $c_{\mu gel}$ = 0.5wt% is the one having slower kinetics and only after 100 minutes the jammed phase turns into a packed supracolloidal lattice. However, the concentration is not sufficient to impart a close packing and d_{ctc} does not reach values below 0.8 μm. When $c_{\mu gel}$=1wt% conditions seems optimal for the formation of

FCC/HCP lattices with high degree of order and the high concentration of microgels allows for optimal packing. In this case d_{ctc} goes far below 0.8 μm and reaches 0.65 μm. Remarkably the kinetics is faster and the d_{ctc} decreases under 0.9 already after 20 minutes. When concentration is increased up to 1.5 wt% the kinetics seems very similar to the latter case, but the whole process is much faster, and in turn this does not allow the lattice to arrange in an optimal extent: d_{ctc} remains above 0.8 μm and 4-folds areas were found seldom together with 6-folds geometries as highlighted in Figure 4.6c, d.

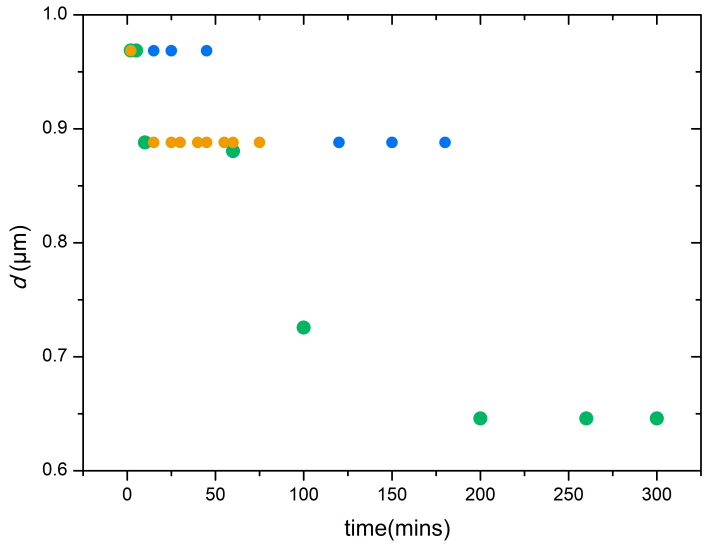

Figure 4.7. d_{ctc} parameter plotted for the three mixtures at different microgels concentration and in a 2mM ACD solution (c_{buffer} = 30mM) as a function of time. $c_{\mu gel}$ = 0.5wt% (blue circle), $c_{\mu gel}$ = 1wt%(green circle), $c_{\mu gel}$ = 1.5wt% (yellow circle).

In their final form the crystals are stuck and perfectly immobilized by the gel matrix as can be seen from 3D DLS analysis performed in 3D cross-correlation mode and with a rotating VAT for non-ergodic samples (Figure 4.8b). Confronting a sample of a pure 1wt% microgels dispersion with a sample of the same microgels in the gel matrix taken at 300 minutes after mix preparation, it can be seen how the two autocorrelation functions differ very visibly. While pure microgels have a fast diffusion and a corresponding fast decay time of the autocorrelation function, the same microgels within the colloidal crystalline domains present a really flat function with a lower intercept caused by decrease of statistics. The decay is less steep and does not seem to go to 0 at high correlation times, indicating the presence of a remarkably hindered diffusion of the microgels inside the crystalline domains, confined by the ACD fibrils. This observation is also confirmed from CSLM images which were analyzed through tracking analysis. The results are represented in Figure 4.8a. While in the left panel the position coordinates are related to a fast and free Brownian motion, in the right panel they follow short

and rigid tracks as consequence of the particle confinement. A slight drift of the crystal makes more visible the tracks left by the single particles, however the displacement calculated from the original position is extremely lower than the pure microgels sample.

The fine characterization of the colloidal crystals obtained goes beyond the aim of the thesis and was addressed only to a superficial extent. Besides, it can be inferred a certain dependence of the lattice geometry from the microgels concentration in the mixture and therefore from the packing of the crystalline phase. Predictably, increasing the microgels weight fraction, which means consequently decreasing the inter-particle distances, implies in turn closer packings (Figure 4.9).

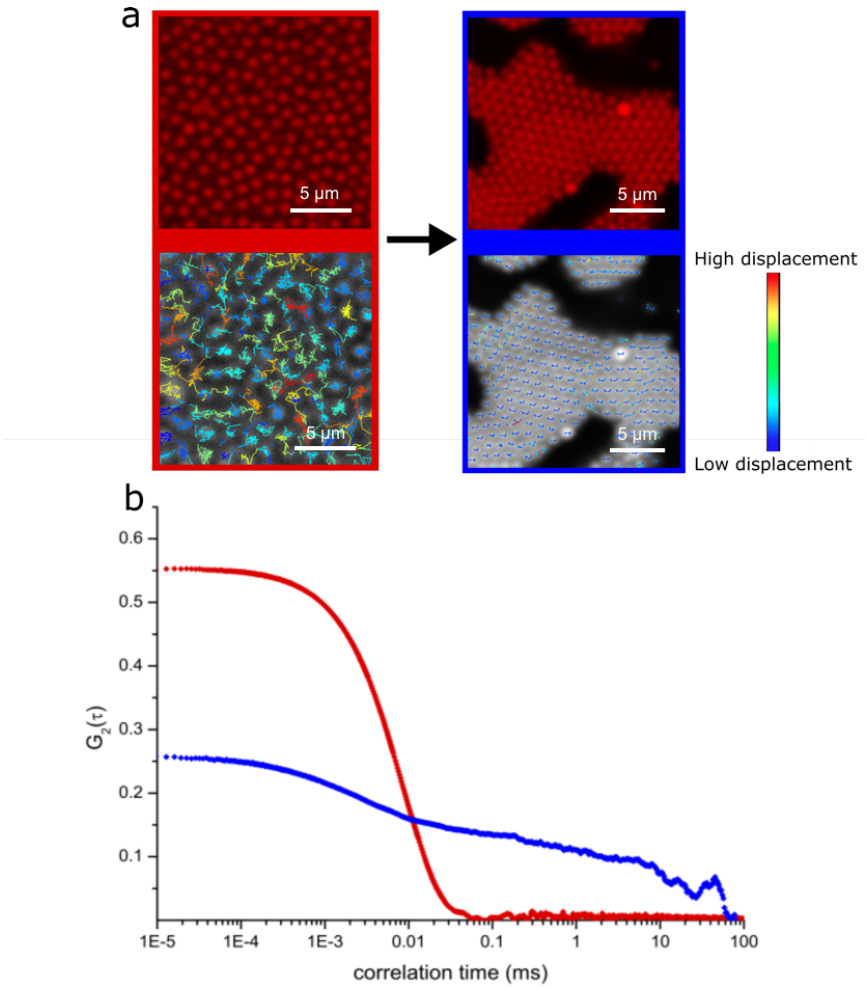

Figure 4.8. Tracking analysis and MSD performed on CSLM images of 1wt% M+ microgels dispersion in water (red) and of a 1wt% M+ microgels dispersion in ACD gel matrix in carbonate buffer (blue) (a). The progressive position coordinates are highlighted with colors depending on their calculated mean square displacement from the initial *xz* coordinates. Autocorrelation functions acquired by 3D DLS in modulated cross correlation mode of the same samples (b).

It was observed a transition from a disordered arrested phase, where microgels were kinetically trapped at 0.5wt%, to a 6-folds geometry lattice as the microgels fraction was increased to

1wt%. However, no sharp transition was verified but still there were traces of disordered jammed phase in the early and medium stages of the 1wt% sample crystals formation.

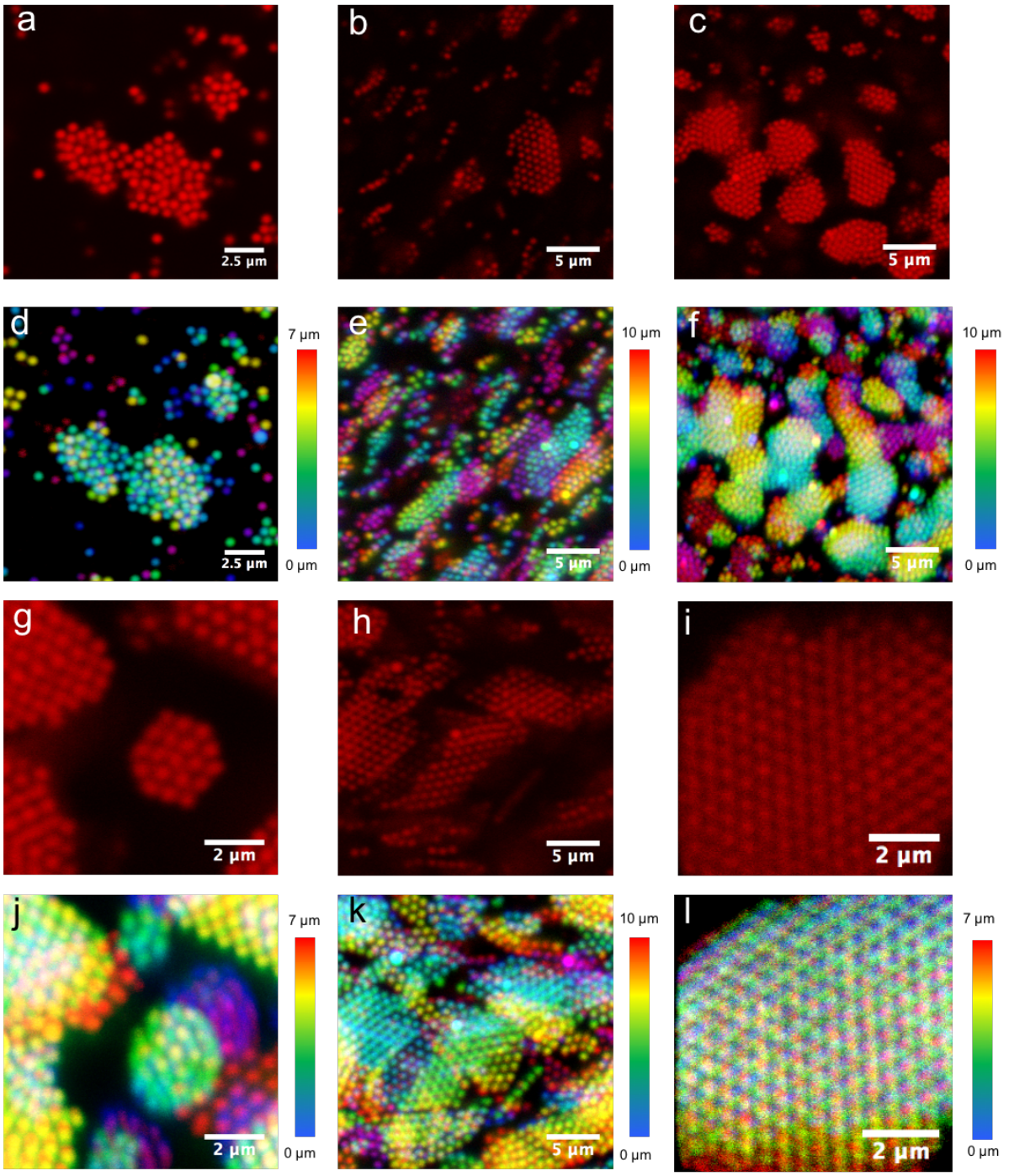

Figure 4.9. CSLM micrographs in fluorescent mode (a, b, c, g, h, i) and z-stacks color coded recostructions with corresponding z-axis values (d, e, f, j, k, l) of different samples with various microgels concentration at 20°C in 30 mM Na_2CO_3/$NaHCO_3$ buffer. The crystals formed are strongly influenced by concentration: $c_{\mu gel}$ = 0.2 wt% (a, d), $c_{\mu gel}$ = 0.5wt% (b, e, c, f), $c_{\mu gel}$ = 1 wt% (g, j, h, k, I, l).

4.3 Discussion

A brief study on colloidal crystals formation triggered by depletion process imparted from a fibrillar gel matrix was above reported. The characterization of the ACD fibrils was already reported in the introduction part (see Chapter 1, par. 2.2). As already remarked, ACD fibrils are the result of instantaneous self-assembly process starting from primary BSD micelles. Compresence of adjacent micelles (c_{ACD} = 2mM) in the suspending medium (an aqueous 30mM carbonate/bicarbonate buffer solution at pH 9.5), induces the aggregation of such structures already at room temperature which spontaneously self-assemble in elongated charged fibrils, forming a SAFIN gel. Depletion effect on the microgels is then induced by the BSD *sphere-to-rod* transition to fibrils, as demonstrated by the progressive formation of bi-dimensional crystalline nuclei, followed by secundary nucleation in more extended 3D lattices. The formation of such crystals was observed to be strongly concentration-dependent as the sample with the lowest microgels weight fraction analyzed ($c_{\mu gel}$ = 0.2 wt%), didn't show any crystalline structure or showed little disordered depleted arrays of microgels (figure 4.1a, e,h), while the higher concentrated sample analyzed (1.5 wt%) gave colloidal crystals formation already in short times. The kinetics of colloidal crystal formation together with the progressive increase in crystallinity of the microgels phase as a function of time was followed efficiently by CSLM. As shown in Figure 4.1, a rather intuitive progressive growth of the crystals took place in a time range which was strongly concentration dependent. The growth was characterized always by a corresponding increase of crystallinity as proven from *g(r)* extraction performed on CSLM micrographs (Figures 4.2, 4.3 and 4.5). The number of peaks of the *g(r)* was observed to grow linearly with time and first peak position, meaning that center-to-center distance (*i.e.* inter-particle distance), to decrease. The progressive decrease of the inter-particle distance could be explained by considering the "soft" interaction potential on the microgels surface which indeed allowed them to compact towards a limit value when pushed from an external force or when a certain value of the volume fraction is reached, as different studies have confirmed.[120–122] This kind of potential was already defined in literature and is characterized by a finite repulsion at particle-particle contact points given by the softness and the high elasticity due to the low degree of crosslinking of the PNIPMAM network. It's been reported that the density of a PNIPMAM microgels radially decreases in a manner strongly dependent on the degree of crosslinking.[123,124] As direct consequence, the packing of these colloidal crystals reaches center-to-center distances below the accepted value for hard spheres colloidal crystals having theoretical infinite repulsion at the overlap region. Assuming a constant particle diameter, in

the fluid regime the interaction potential could theoretically be described by a Hertzian potential given by the equation 4.1:

$$U(r) = \varepsilon \left(1 - \frac{r}{\sigma}\right)^{2.5} \qquad (4.1)$$

Where r is particles radii, σ is the inter-particle distance and ε the strength of the interaction potential.

The strength would be then apparently set by the degree of elasticity of the PNIPAM crosslinked network. The lower limit for the inter-particle distance found for lattices of PNIPAM microgels is around 0.7-0.65, value found also on the lattices reported in this study. The increase of crystallinity was not correlated to the depletion interaction but to the progressive energy lowering process which the microgels undergo due to particles accommodation in a surrounding of sterically stabilized neighboring microgels. Adjacent fibrils, forming an envelope around the crystals increasing the local pressure on the lattice, triggering the consequent increase in crystallinity.

Furthermore, as represented in Figure 4.1c, g, k, after 2 h from preparation, the crystalline domains give rise to a uniform microgels phase which demixes from the monophasic system in the spinodal decomposition regime where the two phases have opposite features (anisotropic/amorphous and isotropic/crystalline). This effect is reasonably reached in the last stages of the process and does not represent a relevant feature for the aim of this study.

Concluding, several observations can be made on the above reported experiments: the *sphere-to-rod* transition is responsible for the formation of primary nuclei of crystallization. It must be stressed that the *sphere-to-rod* transition of ACD from micelles to fibrils is a really fast process, and even though several methods were used (cryo-TEM and DLS) to characterized the kinetics of such transformation, none of them succeeded.

The entity of the depletion will be discussed in Chapter 5 with the help of some theoretical models that constitute just the first attempt to a better understanding of the process of colloidal crystals formation in the above mentioned conditions. Without any doubt the possibility to explain the phenomenon resorting to a basic "spheres in a rod-like dispersion" model is feasible, as long as this approximation is not used to justify the details of the whole process.

Fibrils elongation is fast and cannot be responsible for crystalline growth *tout-court*. While the depletion interaction decreases as a function of time and of fibrils elongation from rods, microgels have instead a reduced but still persistent freedom of translational motion through the fibrillar network. Percolation through the fibrillar network allows for crystal expansion and

optimization of configuration towards the 6-folds symmetry lattices since is the lowest energy demanding configuration accessible. FCC and HCP are probably both present within crystalline domains because of the similar energetic level but the relative amount could not be addressed to a satisfactory extent[119].

4.4 Conclusions

The experiments proved how depletion effect induced by *sphere-to-rod* transition of ACD is effective on PNIPAM microgels having a soft Hertzian inter-particle potential, bringing to the formation of extended supracolloidal crystalline assemblies with different degrees and types of crystallinity. The fibrillar framework, an example of application of SAFIN gel, worked as both depletant and confinement mesh. When mixture was prepared, microgels were able to diffuse, even though the Brownian motion was already reduced at $t = 0$ because of the partial elongation of the fibrils, which is a rather fast process of aggregation. With time, translational motion became more and more hindered ending up with a frozen status when the microgels were kinetically trapped inside the fibrillar domains.

It was found that increasing the microgels weight fraction up to 1.5 wt% the crystals formation accelerated, as a result of the incremented kinetic of primary nucleation directly dependent on concentration. Inter-particle distances were found to decrease linearly with increasing concentrations, while the degree of crystallinity increases. The insights on the type of lattices formed were not part of the subject of this dissertation, besides, was found through FFT processed on crystallites CSLM images, that FCC constitutes the most diffused type of symmetry, with seldom observable traces of other crystalline types at 20°C. The reported results can be read in the light of the new use of a rapid bottom-up assembly pathway to form a stable dispersion of colloidal crystals. A supramolecular self-assembled fibrillar structure of ACD allowed for the supracolloidal assembly of crystalline arrays of microgels under confinement and reduced mobility. Microgels have range of sizes above 600 nm with inter-particle distances of the same length scale, providing only marginal interaction with incident electromagnetic radiation such UVvis light. As well known, the gap of refractive index between the particles and the dispersant media accounts for the possibility to obtain colloidal crystals with PBG properties. Microgels have a refractive index slightly different from that of the water medium and do not constitute any advance in this respect, although their use helped, as labeled model system rapidly detectable with CSLM, to model a robust approach for crystal preparation without resorting to any functionalization of the particles, covalent binding or specific top-

down approach on inorganic materials. Furthermore, the possibility to upgrade the system substituting polymeric particles with metallic nanoparticles having sizes below 100 nm is of course envisioned and already started in the context of the same study.

5 Theoretical models

5.1 Chapter Rationale

Through experimental data acquired on the mixtures of BSD supramolecular structures and charged microgels was highlighted how the BSD supramolecular tubules are naturally high reactive species with a relevant anisotropy of interaction potential, given by their intrinsic and variegate morphology in terms of supramolecular structure, both as pure systems or catanionic mixtures. So far, the mechanism of such interactions taking place between the BSD self-assembled aggregates and isotropic charged microgels reported in this work was only partially understood. To better analyze the experimental evidences in the following will be provided basic theoretical models and calculations that must be acknowledged as a starting point for further and more complex theoretical analyses.

5.2 Sphere-tubule interaction

Considering the results reported in Chapters 2 and 3, regarding the interaction between supramolecular BSD tubules and polymeric homogeneous or core-shell microgels, several experimental observations can be here summarized.

- Mixtures of catanionic charged tubules and oppositely charged polymeric microgels always interact to a different extent, depending on how the charged tubular surface is able to direct the co-assembly. Actually, it was found that all supramolecular structures described in Chapters 2 and 3 have two binding sites reporting a well-defined priority: the potential happens to be stronger to the tips of the tubules while weakens along the discontinuities on the rolled supramolecular sheet. The potential is negligible on the smooth surface, indicating that the exceeding charge is located in the marginal edges of the supramolecular bilayers. Indeed, the electrostatic interaction, intended as a long range attraction between oppositely charged entities, plays a fundamental role in the co-assembly pathway.
- When both species have charge of the same sign, no interaction is observed. When one or both species are neutral the electrostatic contribution to the overall interaction weakens.

It was proved, in particular, that in mixtures of positively charged mcrogels and large neutral catanionic tubules the interaction weakened and no adsorption of microgels on the tubular

surface took place until $c_{\mu gel}$ reached a concentration threshold. In those conditions, adsorption only to the primary binding site (the tips) was restored.

- As clearly shown in the case of the interaction between M+microgels and HNaphC scrolls the angle between the attached scrolls and their number depend both on the ratio between the cross section radius of the tubular aggregates and the microgel radius.

- Interactions to the tip and on along the tubular surface occur at the same time when the tubules are formed by scrolls of supramolecular sheets with the edges on the external surface of the scrolls. This happens for the ACD/CCD mixed scrolls for which a decoration of the external surface was observed in proper conditions. It cannot happen for the HNaphC tubular structures which are formed by double scrolls with the sheet edges hidden in the interior of the scrolls.

The conclusion is that the morphology of the tubules is a pivotal aspect in the interaction with the microgels.

-It is important to remark that, even though microgels used in this work are charged species, in several experimental conditions reported in Chapter 3 they were found to be actually uncharged (Figure 5.1 right), and still interacting with high specificity. That evidence strengthens the hypothesis of a complex interaction mechanism where van der Waals interaction, hydrophobic effect, counterion release are involved.

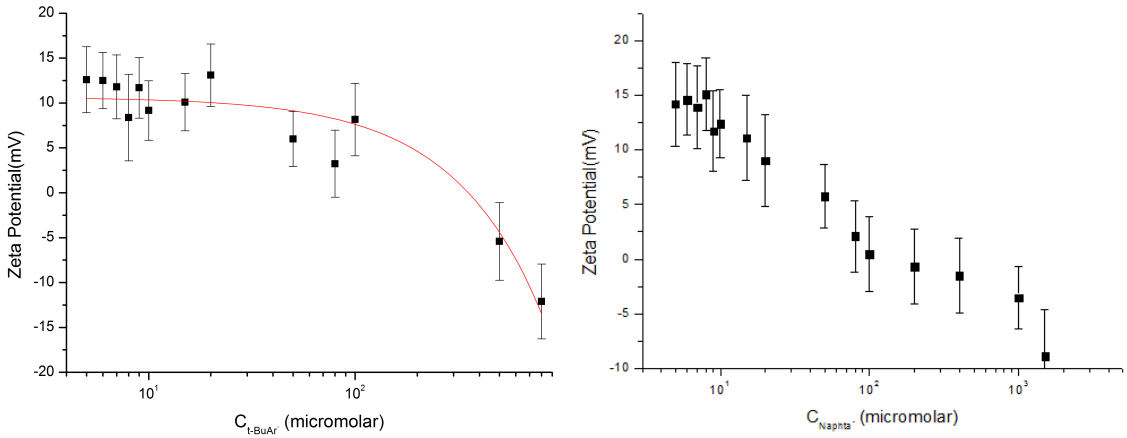

Figure 5.1. Zeta potential measurements of a dispersion of M+ homogeneous positively charged microgel as a function of BSD concentration below *cac* with increasing concentrations of ACD in 30 mM buffer (left, a polynomial fit is represented as a red line to highlight the starting plateau) and with increasing concentrations of HNaphC at pH 11.50 (right). The experiments were planned to measure the surface charge variation of the microgels reproducing the experimental conditions of Chapter 2 (left graph) and Chapter 3 (right graph). The radical change of charge from positive to negative values is due to the gradual formation of negatively charged aggregates as *cmc* and *cac* of the two bile salts are progressively approached.

The complete neutralization of microgels charge due to experimental conditions (high ionic strength) does not represent an issue for the interaction between the microgels and HNaphC tubules, but instead favors the adsorption when the two species have, in theory, same charge.

In facts high charge screening implies, among the other things, the weakening of electrostatic repulsion.

The dispersant of the mixtures reported in Chapter 3 is water at pH 11.50. A high concentration of Na^+ and OH^- ions must be considered together with a solvating effect played by the BSD monomer not involved in supramolecular aggregation. It is known that in pure bile salt solutions the hydrophobic effect helping the supramolecular aggregation is not able to move the equilibrium completely towards the aggregated form, leaving a relatively high concentration of BSD molecules in solution as free monomers, hence able to screen microgels charges.

These conditions were much different from those reported in the experiment cited here at point 2) and reported in Chapter 2 (see Chapter 2, page 41) where no BSD monomer was present in solution due to the high efficiency of supramolecular aggregation in catanionic mixtures near the 1:1 ratio, and to the absence of buffer in solution. In this case the detrimental impact on the interaction was not due to any charge-screening condition but to the low amplitude of the electrostatic potential involved.

Finally, it is possible to roughly rationalize the whole interaction mechanism affirming that where the electrostatic push is not weakened by charge screening, the attraction between oppositely charged poles dictates the interaction. The directionality is based on the geometry following the basic principle that imposes the priorities depending on the number of contact points available on the tubular surface. When electrostatics is only partially involved, due to neutralization of one the species, another driving force must be invoked for the interaction to be justified. The whole mechanism is schematized in the Figure 5.1.

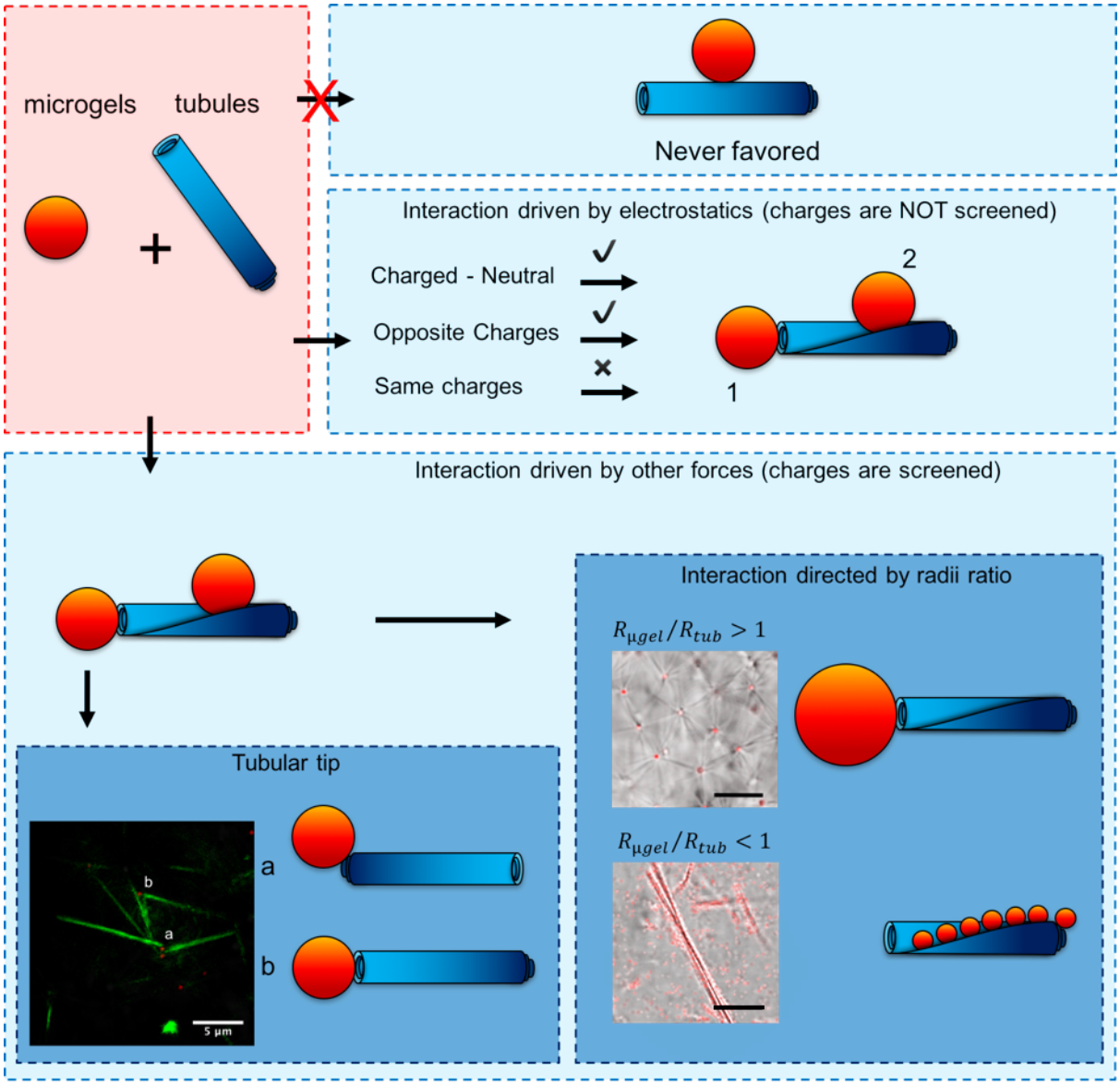

Figure 5.1. Scheme of a basic interpretation of the interaction behavior between self-assembled supramolecular tubules and polymeric microgels based on the experimental data evidences. Scale bar of the CLSM micrographs 5μm. The peculiar supramolecular BSD scroll folding is here schematized as a simple rolled bilayer for the sake of clarity.

5.2.1 Electrostatic interaction potential

The overall interaction mechanism could not be completely understood since experimental evidences revealed how it was related to a different extent to electrostatic driving force, van der Waals interaction and hydrophobic effect, which so far has been only hypothesized. Although hydrophobic effect has for sure a basic importance in the interplay between the polymeric dangling chains and the supramolecular rolled bilayer when electrostatics is not called into action, however, a precise measure of its weight on the mechanism could not yet be investigated

because of its complexity. In the following will be described the interaction from an electrostatic standpoint resorting to a very basic system, represented by a sphere approaching a line or a circle (as represented in the schemes (i) and (ii) of Figure 5.3). In this section we will, in fact, approximate the electrostatic interaction between a tubule and a sphere by assuming that the tubule could be described by (i) a circle and (ii) a line. From this assumption will be investigated if the tip of the tubule or its side is preferential. By assuming a uniform surface-charge distribution, the effective charge of the sphere is $z_s^* = \frac{\sinh(\kappa R_s)}{kR_s} z_s$ where R_s is the radius of the sphere, κ^{-1} is the Debye length, and z_s the valency. The tubule is described by its length h, radius R_t, and charge z_t. The charge-density of the tubule is $\rho_t = \frac{z_t}{(2R_t \pi h)}$.

In (i) will be assumed that the tubule is aligned with the z-axis and the center of the sphere is at $(0, 0, \sqrt{{R_s}^2 - {R_t}^2} + d)$ where d is the distance to contact. Here was assumed $R_s > R_t$. Then the interaction becomes:

$$E_c = l_b \frac{z_s^* \Delta z_t}{\sqrt{{R_s}^2 + 2\sqrt{{R_s}^2 - {R_t}^2}\, d + d^2}} e^{-k\sqrt{{R_s}^2 + 2\sqrt{{R_s}^2 - {R_t}^2}\, d + d^2}} \quad (5.1)$$

where l_b is the Bjerrum length, and $\Delta z_t = 2R_t \pi l \rho_t$ where Δl is the width of the cirle/line segment. In (ii) again was assumed that the tubule is aligned with the z-axis but in this case, the center of the sphere is at $(R_t + R_s + d, 0, 0)$. The interaction then becomes:

$$E_l = \int_{-h}^{h} \frac{e^{-\kappa r}}{r} z_s^* \rho_t \Delta l dh' \quad (5.2)$$

where $r = \sqrt{(R_s + R_t + d)^2 + h'^2}$. By using a Taylor-expansion of the exponential we get:

$$E_l = -l_B z_s^* \rho_t \Delta l \sum_{\kappa=0}^{\infty} {}_2F_1\left(\frac{1}{2}, \frac{1-\kappa}{2}; \frac{3}{2}; \frac{-h^2}{(R_t + R_s + d)^2}\right) \frac{\kappa^k h(-R_t - R_s - d)^{\kappa-1}}{\kappa!} \quad (5.3)$$

Where ${}_2F_1$ is the hypergeometric function.

5.2.2 van der Waals interaction potential

The van der Waals interaction between a sphere and a rod can be expressed as:

$$E_{top} = C_s \int_{-h}^{h} \int_{0}^{2\pi} \frac{-C_t}{r^6} R_t d\theta dh \tag{5.4}$$

where C_t and C_s are two interaction parameters for the rod and the sphere respectively. C_t has the same units as C_s scaled with inverse area. This integral evaluates to

$$E_{top} = -\frac{3\pi C_t C_s}{4R_t^4}\left(\arctan\left(\frac{h-pz}{R_t}\right) + arctan\left(\frac{h+pz}{R_t}\right)\right) -$$

$$-\frac{\pi h}{2}\left(\frac{\left(5R_t^6+12R_t^4h^2+\left(h^2-p_z^2\right)R_t^2\left(R_t^2+11h^2+9p_z^2\right)+3\left(h^2-p_z^2\right)^3\right)}{R_t^3\left(R_t^2+(h+p_z)^2\right)^2\left(R_t^2+(h-p_z)^2\right)^2}\right) \tag{5.5}$$

where we assume that the rod is aligned with the z-axis and that and that the position of the sphere is $(0, 0, p_z)$ where $p_z = h + \sqrt{R_s^2 - R_t^2} + d$. If we assume that the sphere is at the side of the rod, *i.e.* positioned at $(p_r, 0, 0)$ where $p_r = R_t + R_s + d$ then the expression becomes:

$$E_{side} = -\frac{R_t C_t C_s}{4}\int_0^{2\pi}\left(\frac{3\,arctan\left(\frac{h}{\sqrt{\mathbf{z}\cdot\mathbf{r}}}\right)}{(\mathbf{z}\cdot\mathbf{r})^{5/2}} + \frac{h\left(5-\frac{2h^2}{h^2+(\mathbf{z}\cdot\mathbf{r})^2}\right)}{(\mathbf{z}\cdot\mathbf{r})^2(h^2+\mathbf{z}\cdot\mathbf{r})}\right)d\theta \tag{5.6}$$

where $\mathbf{z}\cdot\mathbf{r} = R_t^2 - 2\cos(\theta)R_t p_r + p_r^2$. This expression che then be numerically integrated as to get a final expression.

5.3 Depletion interaction driven by supramolecular self-assembly

The depletion interaction are here calculated considering large hard spheres with radius R_s and much smaller hard spheres with a diameter σ_S under the Derjaguin approximation ($R_L \gg \sigma_S$)[125].

The depletion interaction between two large spheres, which surfaces are separated by distance h reads:

$$U_d = -\frac{\pi}{2} k_B T n_S R_p \sigma_S^2 \left(1 - \frac{h}{\sigma_S}\right)^2 \text{ for } h \leq \sigma_S, \text{ else } 0; \qquad (5.7)$$

where k_B is the Boltzmann constant, T is temperature in Kelvin and n_S is the number density of smaller spheres dispersed in the continuous phase acting as depletants. When considering short rigid rods with a length L_R under the same approximations ($R_L \gg L_R$), a similar expression can be derived:

$$U_d = -\frac{\pi}{6} k_B T n_R R_p L_R^2 \left(1 - \frac{h}{L_R}\right)^3 \text{ for } h \leq L_R, \text{ else } 0; \qquad (5.8)$$

where n_R is the number density of smaller rods dispersed in the continuous phase acting as depletants. The depletant undergoes a transition from spheres to rods (fibrils), that we first model as linear assembly of n touching spheres. It implies that $L_R = n\sigma_S$ and that $n_S = n \cdot n_R$. As the rods are the outcome of the self-assembly process, we therefore have $n_S = 8\varphi/(\pi\sigma_S^3)$, where φ is the depletant volume fraction.

$$\frac{U_d}{K_B T} = -\frac{4n\varphi R_P}{3\sigma_S} \left(1 - \frac{h}{n\sigma_S}\right)^3 \text{ for } h \leq n\sigma_S, \text{ else } 0; \qquad (5.9)$$

In the following was calculated U_d/R_L as a function of L_R defined by n for $\varphi = 0.013$ and $\sigma_S = 20$ nm. The theoretical model can be schematized as represented in Figure 5.2.

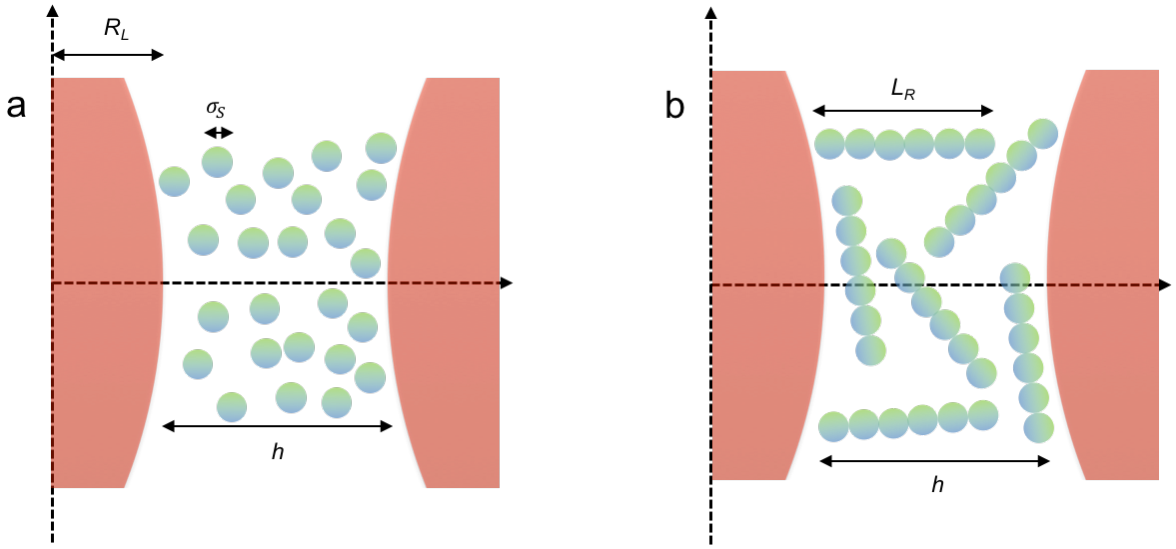

Figure 5.2. Sketches representing the theoretical approach to describe the sphere-to-rod induced depletion mechanism between two large hard spheres with radius R_L. The micelles are approximated as small hard spheres of radius σ_S before the transition (a). After the transition the fibrils are approximated as rods formed by n touching small hard spheres of length L_R (b). Derjaguin approximation is valid in both cases. Note that $n_R = n \cdot n_S$.

5.4 Results

5.4.1 Electrostatic interaction potential calculations

Herein will be reported the calculations following equation (5.1) in the case of big spheres while equation (5.3) will be used for small spheres as the number of terms in the Taylor expansion increases noticeably with R_s, making the calculation demanding. For R_t, R_s, and h experimental values are used while guessed charge values are used for q_s and q_t, namely the spherical surface charge and tubule charge.

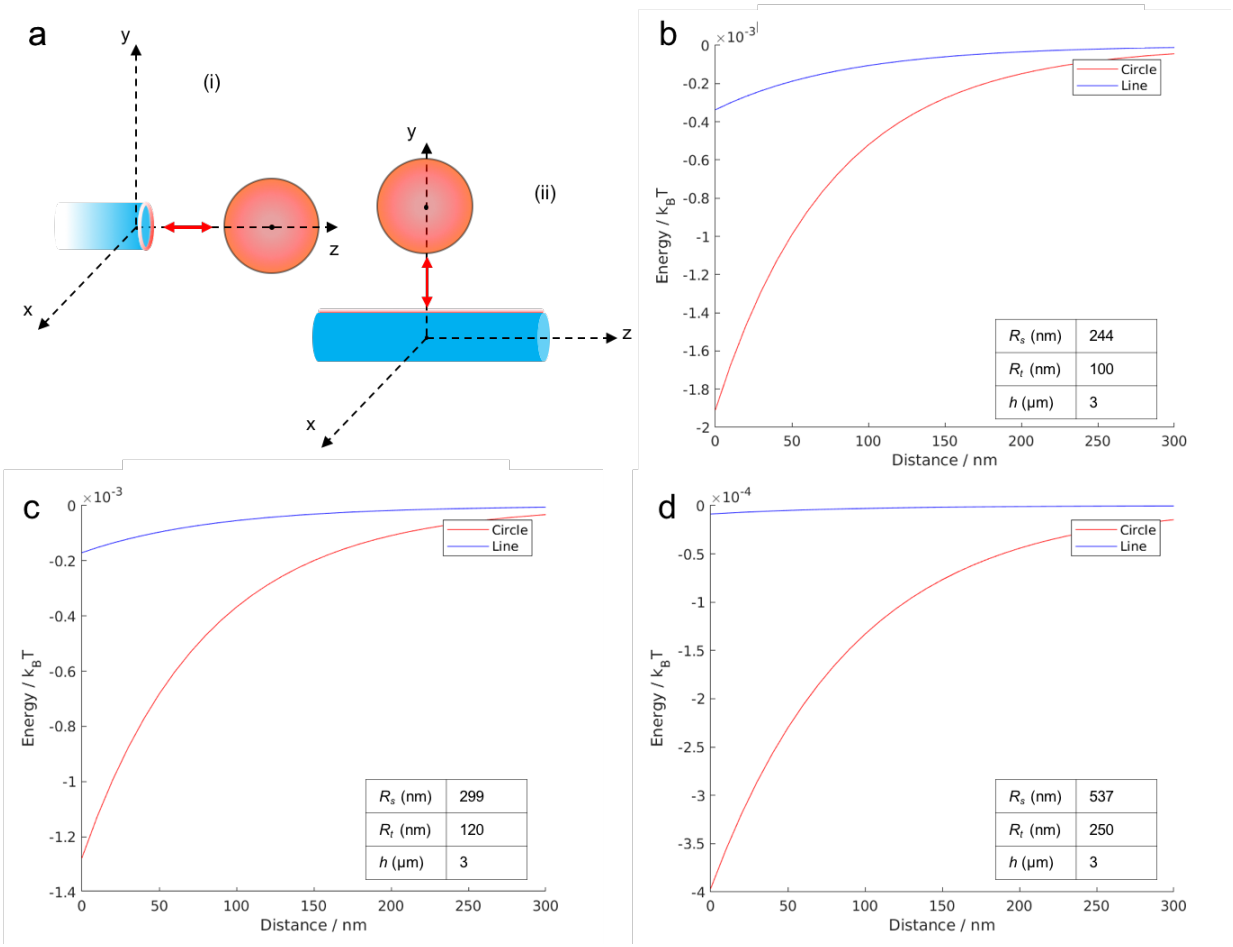

Figure 5.3. Electrostatic interaction potential calculations based on equation 5.1, reproducing the geometrical conditions of some of the experiments reported in Chapters 2 and 3. The calculations were made approximating the system as a sphere approaching a circle (representing the tubular tip) or a line (representing the tubular surface rim) as depicted in the schemes a(i) and a(ii). R_s , R_t and h values are indicated in the figures. The charge used for the spherical surface and the tubule are respectively q_s = 100e and q_t = -1000e while the ionic strength is kept at $1x10^{-5}$ M.

Different values of the ionic strength were tested corresponding to an order of magnitude above and below the value of $1x10^{-5}$ M taken as a general starting value. In Figure 5.3 are reported the first results calculated starting from realistic values of R_s and R_t obtained through experimental analyses. The electrostatic potential seems to be marked at the tips and lower along the line,

confirming a preferential directionality of interaction to the tip binding site. Interestingly, increasing the size of the two species (while decreasing R_s / R_t), the potential modulus decreases.

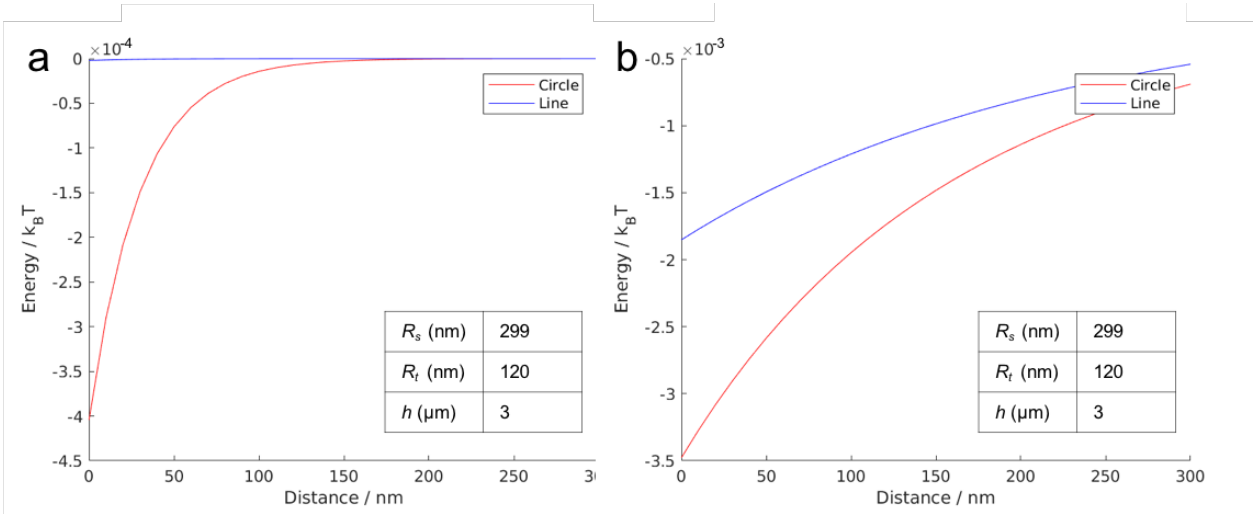

Figure 5.4. Electrostatic interaction potential calculations based on equation 5.1 for a sphere of R_s = 299 nm and a tubule of R_t = 120 nm (see Figure 5.3c) with ionic strength 1x10^{-4} M (a) and 1x10^{-6} M (b).

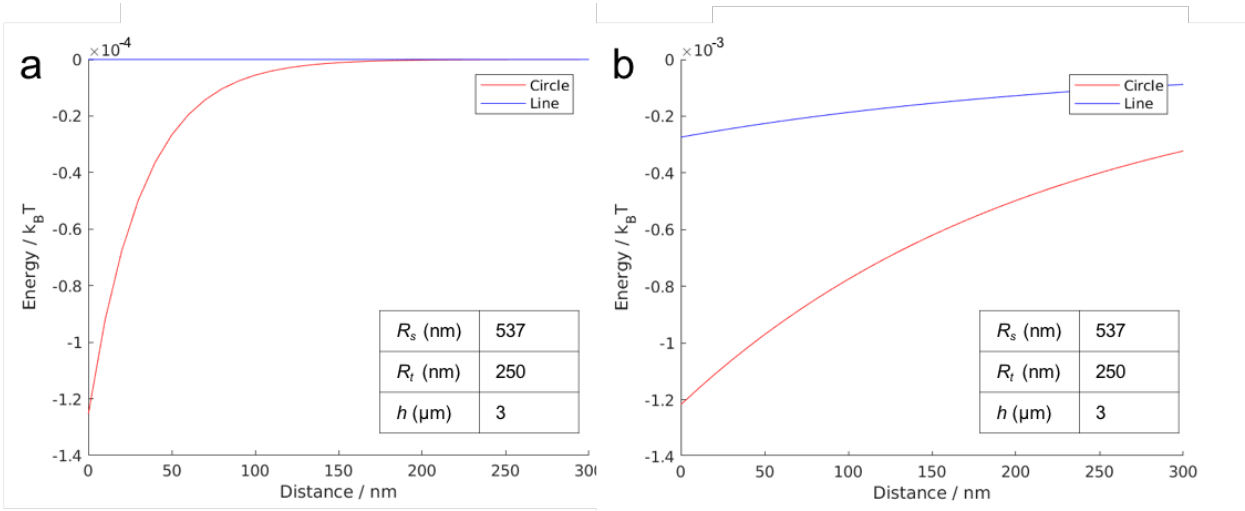

Figure 5.5. Electrostatic interaction potential calculations based on equation 5.1 for a sphere of R_s = 537 nm and a tubule of R_t = 250 nm (see Figure 5.3d) with ionic strength 1x10^{-4} M (a) and 1x10^{-6} M (b).

Results of Figures 5.4 and 5.5 show that, predictably, the decrease of ionic strength alters the charge screening and releases the electrostatic potential around the charged sphere to longer distances. Another set of results were obtained testing the answer of the system when smaller spheres are used, with radii comparable with R_t as schematized in Figure 5.6 (i) and (ii). In this case an increase of the potential amplitude was observed, from which it was again confirmed a pivotal role of the geometric factors implied in the electrostatic interactions mechanism.

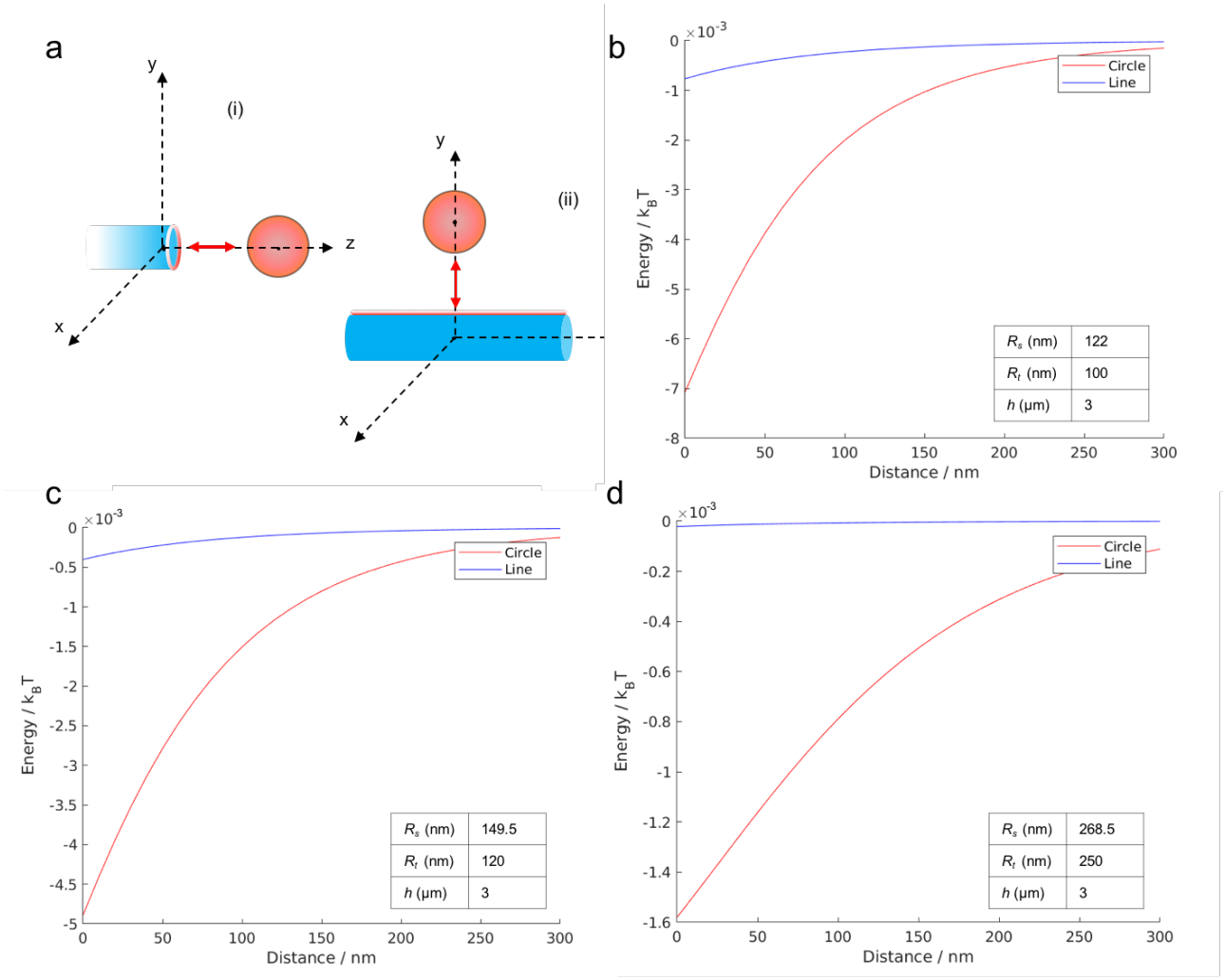

Figure 5.6. Electrostatic interaction-energy calculations based on equation 5.3 for a spheres having R_s / 2 with ionic strength $1x10^{-5}$ M.

5.4.2 van der Waals interactions

Results obtained through calculations, reported in Figure 5.7, show how the van der Waals interaction energy favors the tip binding only when R_s is comparable with R_t. Interestingly was found that at very high R_s, like in the cases where actual sizes of the microgels were taken into account (Figure 5.7a, c, e), the van der Waals interaction is preferential at the sides of the tube. Since at short distances the electrostatics drive the interaction, these result could have implications only at large distances where no particular attention is focused. Diminishing R_s of a ½ of initial value, brings of course to a shortening of the van der Waals potential which is stronger at closer distances but with a fast decay, becoming negligible at medium and large distances.

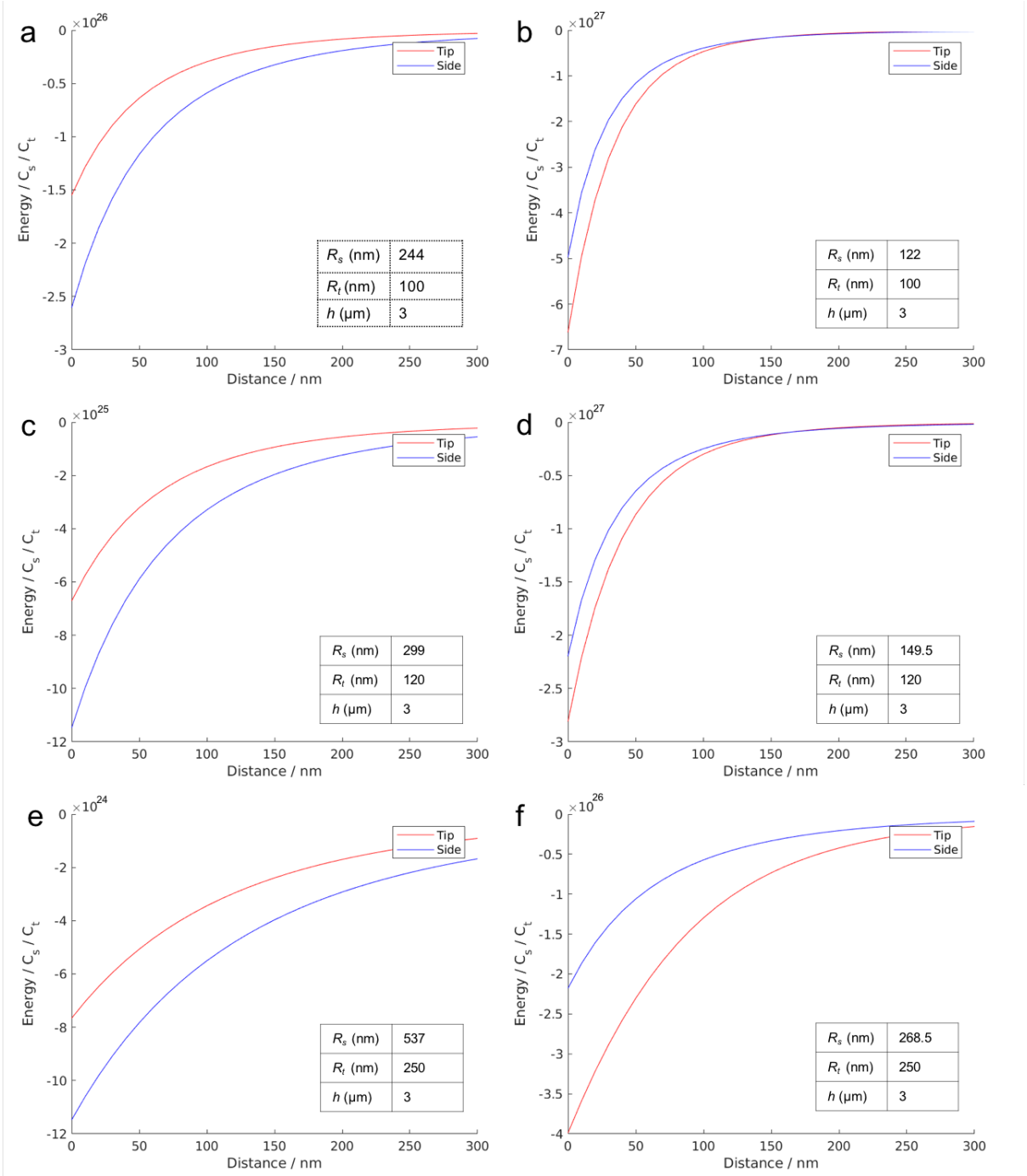

Figure 5.7. van der Waals interaction-energy calculated for a sphere and a tubule with the values reported in the insets.

5.4.3 Depletion interaction calculations

Results of the calculation show that the depletion interaction is strongly influenced by the assembly process in term of range and amplitude. The range is fixed by the length of the rods, whereas the amplitude first decreases for $n = 2$ and then linearly increases for $n > 2$. This can be easily derived by looking to the limit for $h \rightarrow 0$

$$\frac{U_d(h \rightarrow 0)}{k_B T} = -\frac{\pi n n_S R_P \sigma_S^2}{6} = -\frac{4 n \varphi R_P}{3 \sigma_S} \qquad (5.10)$$

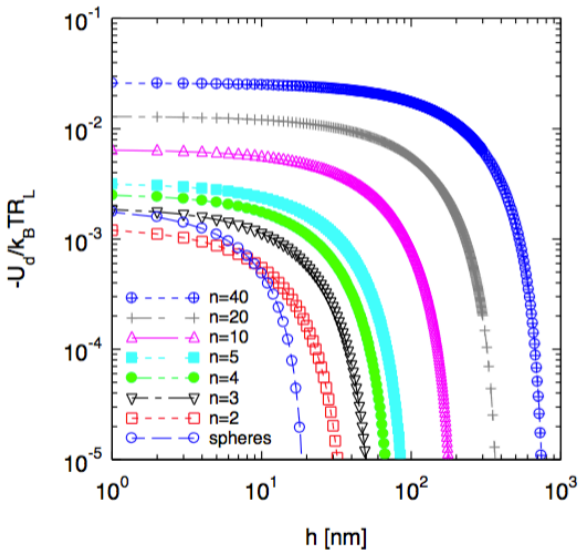

Figure 5.8. Calculation of the depletion potential as a function of the number of spheres linearly assembled for $\varphi = 0.013$ and $\sigma_S = 20$ nm.

When the simulation results are compared with simulations under Derjaguin approximation, there is a rather good agreement with the analytical solution[126] which holds in a quite wide range of h/σ_S values (Figure 5.8). However, sizes smaller than 20 nm should be used for the depletants diameters, since the experimental data suggest that micelles and hence fibrils don't exceed 5 nm in diameter. To better apply the model was decided to approximate the rods with a point-like beads model, using the same values for n, φ, R_S and R_L. The model reveals some weaknesses due to the lesser agreement with the analytical solution when the small spheres size is decreased to point-like. Comparing the simulated Derjaguin approximation developed in Figure 5.9 with simulations involving point-like beads with $n = 10$, 20 and 40 and $\varphi = 0.013$, the agreement is visibly less marked as n is increased (Figure 5.10).

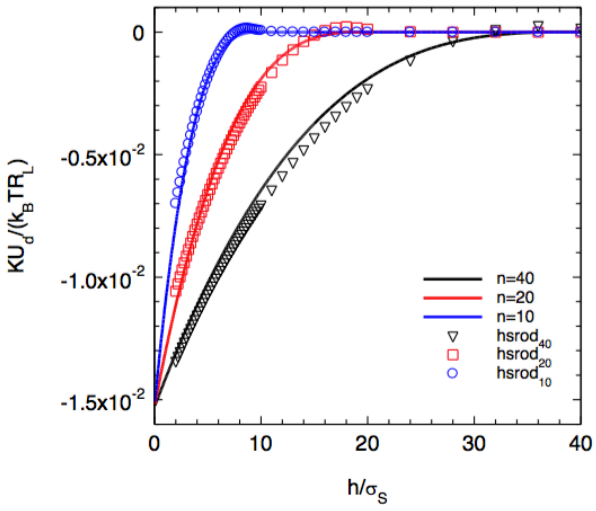

Figure 5.9. Comparison between the Derjaguin approximation and simulations using hard spheres linear assemblies as model for rods for n =10, 20 and 40 (symbols) for $\varphi = 0.013$. The solid lines are the Derjaguin calculations performed for $\varphi = 0.013$ and σ_S = 20 nm, where h has been rescaled by σ_S. The interaction energy was as well rescaled by a factor K for each "rod" to match the experiments.

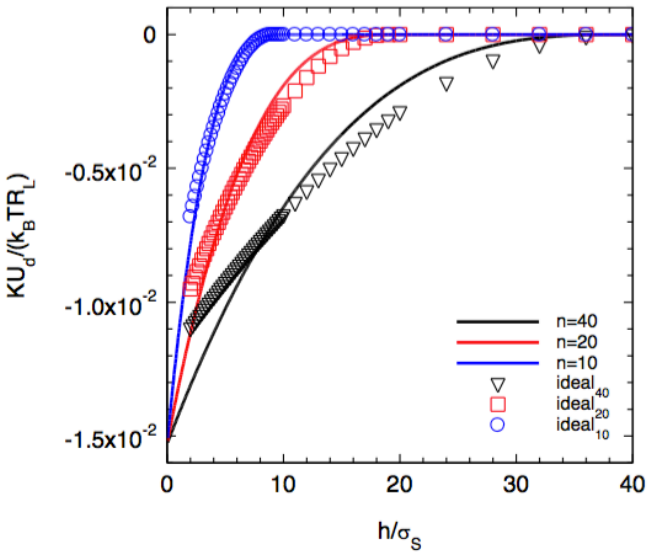

Figure 5.10. Comparison between the Derjaguin approximation and simulations with point-like beads with n= 10, 20 and 40 (symbols) for $\varphi = 0.013$. The solid lines refer to the Derjaguin calculations performed in Figure 5.9.

5.5 Conclusions

Limited by the simplicity of the models with respect to the complexity of the systems studied, the theoretical calculations supported experimental data with acceptable levels of agreement. Regarding the interaction between BSD supramolecular tubules and microgels the electrostatics interaction calculations provided important backup information on the specificity of the

microgels for the tips of the tubules confirming a role of such mechanism in the general interaction. When both the systems are charged, the electrostatics drive the interaction always at the tip of the tubules at the expense of the rim binding site. As hypothesized, a part from the charge, the radii ratio between the microgels and the tubule turns out again to be a fundamental factor. When sphere radius was increased, specificity was still observed but energy of interaction weakened. van der Waals interaction calculations were more difficult to rationalize. The van der Waals interaction-energy resulted from calculations indicated that tip binding site is preferential the more the radii ratio is near 1, instead the more the radius of the sphere is increased, the more the side binding site is highly favored. However, as a general principle smaller species have a potential which develops in smaller range, and consequently the van der Waals interaction-energy decays in the short range, becoming negligible at medium range.

Regarding the depletion interaction calculations, the model utilized, which implied the emulation of a *sphere-to-rod* transition from micelles to fibrils with "small touching-spheres" worked, showing that for n small hard spheres having non-negligible mass, the depletion potential increases as n increases. The theoretical model weakens when point-like beads are used in place of small hard spheres, making of further theoretical studies a mandatory step to a better understanding of the colloidal crystals nucleation.

The work is the result of a fruitful collaboration with Prof. Jérôme J. Crassous and the Physical Chemistry Division of Lund University, Lund, Sweden.

6 References

(1) Biró, L. P.; Vigneron, J. P. Photonic Nanoarchitectures in Butterflies and Beetles: Valuable Sources for Bioinspiration. *Laser Photonics Rev*. **2011**, *5* (1), 27–51.

(2) Birchmeier, W. Cytoskeleton Structure and Function. *Trends Biochem. Sci*. **1984**, *9* (4), 192–195.

(3) Olins, D. E.; Olins, A. L. Chromatin History: Our View from the Bridge. *Nat. Rev. Mol. Cell Biol*. **2003**, *4* (10), 809–814.

(4) Lehn, J. -M. Supramolecular Chemistry—Scope and Perspectives Molecules, Supermolecules, and Molecular Devices (Nobel Lecture). *Angew. Chemie Int. Ed. English* **1988**, *27* (1), 89–112.

(5) Lehn, B. J. Perspectives in Supramolecular Chemistry- From Molecular Recognition towards Molecular Information Processing and Self-Organization. **1990**, *29*, 1304–1319.

(6) Antonietti, M.; Göltner, C. Superstructures of Functional Colloids: Chemistry on the Nanometer Scale. *Angew. Chemie (International Ed. English)* **1997**, *36* (9), 910–928.

(7) Whitesides, G. M.; Kriebel, J. K.; Mayers, B. T. 9. Self-Assembly and Nanostructured Materials. *Nanostructured Mater*. 217–239.

(8) Morphew, D.; Chakrabarti, D. Clusters of Anisotropic Colloidal Particles: From Colloidal Molecules to Supracolloidal Structures. *Curr. Opin. Colloid Interface Sci*. **2017**, *30*, 70–80.

(9) Blaaderen, A. van. Colloidal Molecules and Beyond. *Science (80-.)*. **2003**, *301* (July), 470–471.

(10) De La Cotte, A.; Wu, C.; Trévisan, M.; Repula, A.; Grelet, E. Rod-Like Virus-Based Multiarm Colloidal Molecules. *ACS Nano* **2017**, *11* (10), 10616–10622.

(11) Li, F.; Josephson, D. P.; Stein, A. Colloidal Assembly: The Road from Particles to Colloidal Molecules and Crystals. *Angew. Chemie - Int. Ed*. **2011**, *50* (2), 360–388.

(12) Yuan, Q.; Gu, J.; Zhao, Y. N.; Yao, L.; Guan, Y.; Zhang, Y. Synthesis of a Colloidal Molecule from Soft Microgel Spheres. *ACS Macro Lett*. **2016**, *5* (5), 565–568.

(13) Gregorczyk, K.; Knez, M. Hybrid Nanomaterials through Molecular and Atomic Layer Deposition: Top down, Bottom up, and in-between Approaches to New Materials. *Prog. Mater. Sci*. **2016**, *75*, 1–37.

(14) Leunissen, M. E.; Christova, C. G.; Hynninen, A.-P.; Royall, C. P.; Campbell, A. I.; Imhof, A.; Dijkstra, M.; van Roij, R.; van Blaaderen, A. Ionic Colloidal Crystals of Oppositely Charged Particles. *Nature* **2005**, *437* (7056), 235–240.

(15) Armstrong, E.; O'Dwyer, C. Artificial Opal Photonic Crystals and Inverse Opal Structures-Fundamentals and Applications from Optics to Energy Storage. *J. Mater. Chem. C* **2015**, *3* (24), 6109–6143.

(16) Kalsin, A. M.; Fialkowski, M.; Paszewski, M.; Smoukov, S. K.; Bishop, K. J. M.; Grzybowski, B. A. Electrostatic Self-Assembly of Binary Nanoparticle Crystals with a Diamond-Like Lattice. No. 2 mM.

(17) Liljeström, V.; Seitsonen, J.; Kostiainen, M. A. Electrostatic Self-Assembly of Soft Matter Nanoparticle Cocrystals with Tunable Lattice Parameters. *ACS Nano* **2015**, *9* (11), 11278–11285.

(18) Haque, M. A.; Mito, K.; Kurokawa, T.; Nakajima, T.; Nonoyama, T.; Ilyas, M.; Gong, J. P. Tough and Variable-Band-Gap Photonic Hydrogel Displaying Programmable Angle-Dependent Colors. *ACS Omega* **2018**, *3* (1), 55–62.

(19) Ikkala, O.; ten Brinke, G. Hierarchical Self-Assembly in Polymeric Complexes: Towards Functional Materials. *Chem. Commun*. **2004**, No. 19, 2131.

(20) Elemans, J. A. A. W.; Rowan, A. E.; Nolte, R. J. M. Mastering Molecular Matter. Supramolecular Architectures by Hierarchical Self-Assembly. *J. Mater. Chem*. **2003**, *13*

(11), 2661–2670.
(21) Seeman, N. C.; Belcher, A. M. Nanoscience: Underlying Physical Concepts and Phenomena. Proceedings of the Arthur M. Sackler Colloquium of the National Academy of Sciences. May 18-20, 2001. Washington, DC, USA. *Proc. Natl. Acad. Sci. U. S. A.* **2002**, *99 Suppl 2*, 6451–6517.
(22) Lehn, J.-M. Toward Self-Organization and Complex Matter. *Science (80-.).* **2002**, *295* (5564), 2400–2403.
(23) Nelson, E. C.; Dias, N. L.; Bassett, K. P.; Dunham, S. N.; Verma, V.; Miyake, M.; Wiltzius, P.; Rogers, J. A.; Coleman, J. J.; Li, X.; et al. Epitaxial Growth of Three-Dimensionally Architectured Optoelectronic Devices. *Nat. Mater.* **2011**, *10* (9), 676–681.
(24) Bakker, H. E.; Dussi, S.; Droste, B. L.; Besseling, T. H.; Kennedy, C. L.; Wiegant, E. I.; Liu, B.; Imhof, A.; Dijkstra, M.; van Blaaderen, A. Phase Diagram of Binary Colloidal Rod-Sphere Mixtures from a 3D Real-Space Analysis of Sedimentation–Diffusion Equilibria. *Soft Matter* **2016**, *12* (45), 9238–9245.
(25) Sacanna, S.; Irvine, W. T. M.; Chaikin, P. M.; Pine, D. J. Lock and Key Colloids. *Nature* **2010**, *464* (7288), 575–578.
(26) Hatch, H. W.; Krekelberg, W. P.; Hudson, S. D.; Shen, V. K. Depletion-Driven Crystallization of Cubic Colloids Sedimented on a Surface. *J. Chem. Phys.* **2016**, *144* (19), 9–11.
(27) Qiu, H.; Hudson, Z. M.; Winnik, M. A.; Manners, I. Multidimensional Hierarchical Self-Assembly of Amphiphilic Cylindrical Block Comicelles. *Science (80-.).* **2015**, *347* (6228), 1329–1332.
(28) Pavlopoulos, N. G.; Dubose, J. T.; Pinna, N.; Willinger, M. G.; Char, K.; Pyun, J. Synthesis and Assembly of Dipolar Heterostructured Tetrapods: Colloidal Polymers with "Giant Tert-Butyl" Groups. *Angew. Chemie - Int. Ed.* **2016**, *55* (5), 1787–1791.
(29) Wang, Y.; Wang, Y.; Breed, D. R.; Manoharan, V. N.; Feng, L.; Hollingsworth, A. D.; Weck, M.; Pine, D. J. Colloids with Valence and Specific Directional Bonding. *Nature* **2012**, *491* (7422), 51–55.
(30) Jackson, A. M.; Hu, Y.; Silva, P. J.; Stellacci, F. From Homoligand- to Mixed-Ligand-Monolayer-Protected Metal Nanoparticles: A Scanning Tunneling Microscopy Investigation. *J. Am. Chem. Soc.* **2006**, *128* (34), 11135–11149.
(31) Gröschel, A. H.; Walther, A.; Löbling, T. I.; Schacher, F. H.; Schmalz, H.; Müller, A. H. E. Guided Hierarchical Co-Assembly of Soft Patchy Nanoparticles. *Nature* **2013**, *503* (7475), 247–251.
(32) Mihut, A. M.; Stenqvist, B.; Lund, M.; Schurtenberger, P.; Crassous, J. J. Assembling Oppositely Charged Lock and Key Responsive Colloids: A Mesoscale Analog of Adaptive Chemistry. *Sci. Adv.* **2017**, *3* (9), 1–10.
(33) Petukhov, A. V.; Tuinier, R.; Vroege, G. J. Entropic Patchiness: Effects of Colloid Shape and Depletion. *Curr. Opin. Colloid Interface Sci.* **2017**, *30*, 54–61.
(34) Grzelczak, M.; Vermant, J.; Furst, E. M.; Liz-Marzán, L. M. Directed Self-Assembly of Nanoparticles. *ACS Nano* **2010**, *4* (7), 3591–3605.
(35) Crassous, J. J.; Millard, P.-E.; Mihut, A. M.; Wittemann, A.; Drechsler, M.; Ballauff, M.; Schurtenberger, P. Giant Hollow Fiber Formation through Self-Assembly of Oppositely Charged Polyelectrolyte Brushes and Gold Nanoparticles. *Soft Matter* **2013**, *9* (38), 9111.
(36) Mizeikis, V.; Juodkazis, S.; Marcinkevičius, A.; Matsuo, S.; Misawa, H. Tailoring and Characterization of Photonic Crystals. *J. Photochem. Photobiol. C Photochem. Rev.* **2001**, *2* (1), 35–69.
(37) Kim, S. H.; Lee, S. Y.; Yang, S. M.; Yi, G. R. Self-Assembled Colloidal Structures for Photonics. *NPG Asia Mater.* **2011**, *3* (1), 25–33.

(38) Pendry, J. B.; Holden, A. J.; Robbins, D. J.; -, al; Xiao, S.; Shen, L.; Loiko, V. A.; Miskevich, A. A. Calculating Photonic Band Structure. *J. Phys. Condens. Matter* **1996**, *8*, 1085–1108.
(39) Nagarajan, R.; Ruckenstein, E. Theory of Surfactant Self-Assembly: A Predictive Molecular Thermodynamic Approach. *Langmuir* **1991**, *7* (12), 2934–2969.
(40) Svenson, S. Controlling Surfactant Self-Assembly. *Curr. Opin. Colloid Interface Sci.* **2004**, *9* (3–4), 201–212.
(41) Israelachvili, J. N.; Mitchell, J. D.; Ninham, B. W. Theory of Self-Assembly of Hydrocarbon Amphiphiles into Micelles and Bilayers. *J. Chem. Soc., Faraday Trans. 2 Mol. Chem. Phys.* **1976**, *72*, 1525–1568.
(42) Whitesides, G.; Mathias, J.; Seto, C. Molecular Self-Assembly and Nanochemistry: A Chemical Strategy for the Synthesis of Nanostructures. *Science (80-.).* **1991**, *254* (5036), 1312–1319.
(43) Saha, S. K.; Banerjee, A.; Banerjee, S.; Bose, S. Synthesis of Nanocrystalline Hydroxyapatite Using Surfactant Template Systems: Role of Templates in Controlling Morphology. *Mater. Sci. Eng. C* **2009**, *29* (7), 2294–2301.
(44) Shah, R. N.; Shah, N. A.; Del Rosario Lim, M. M.; Hsieh, C.; Nuber, G.; Stupp, S. I. Supramolecular Design of Self-Assembling Nanofibers for Cartilage Regeneration. *Proc. Natl. Acad. Sci.* **2010**, *107* (8), 3293–3298.
(45) Nga, N. K.; Giang, L. T.; Huy, T. Q.; Viet, P. H.; Migliaresi, C. Surfactant-Assisted Size Control of Hydroxyapatite Nanorods for Bone Tissue Engineering. *Colloids Surfaces B Biointerfaces* **2014**, *116*, 666–673.
(46) Zhang, S. G.; Marini, D. M.; Hwang, W.; Santoso, S. Design of Nanostructured Biological Materials through Self- Assembly of Peptides and Proteins. *Curr. Opin. Chem. Biol.* **2002**, *6* (6), 865–871.
(47) Ganta, S.; Devalapally, H.; Shahiwala, A.; Amiji, M. A Review of Stimuli-Responsive Nanocarriers for Drug and Gene Delivery. *J. Control. Release* **2008**, *126* (3), 187–204.
(48) Panda, J. J.; Mishra, A.; Basu, A.; Chauhan, V. S. Stimuli Responsive Self-Assembled Hydrogel of a Low Molecular Weight Free Dipeptide with Potential for Tunable Drug Delivery. *Biomacromolecules* **2008**, *9* (8), 2244–2250.
(49) Heinz, H.; Pramanik, C.; Heinz, O.; Ding, Y.; Mishra, R. K.; Marchon, D.; Flatt, R. J.; Estrela-Lopis, I.; Llop, J.; Moya, S.; et al. Nanoparticle Decoration with Surfactants: Molecular Interactions, Assembly, and Applications. *Surf. Sci. Rep.* **2017**, *72* (1), 1–58.
(50) Israelachvili, J. N. *Intermolecular and Surface Forces: Third Edition*; 2011.
(51) Holmberg, K. Surfactant-Templated Nanomaterials Synthesis. *J. Colloid Interface Sci.* **2004**, *274* (2), 355–364.
(52) Lim, G. K.; Wang, J.; Ng, S. C.; Gan, L. M. Nanosized Hydroxyapatite Powders from Microemulsions and Emulsions Stabilized by a Biodegradable Surfactant. *J. Mater. Chem.* **1999**, *9* (7), 1635–1639.
(53) Schmitt, C.; Grassl, B.; Lespes, G.; Desbrières, J.; Pellerin, V.; Reynaud, S.; Gigault, J.; Hackley, V. A. Saponins: A Renewable and Biodegradable Surfactant from Its Microwave-Assisted Extraction to the Synthesis of Monodisperse Lattices. *Biomacromolecules* **2014**, *15* (3), 856–862.
(54) Maldonado-Valderrama, J.; Wilde, P.; MacIerzanka, A.; MacKie, A. The Role of Bile Salts in Digestion. *Adv. Colloid Interface Sci.* **2011**, *165* (1), 36–46.
(55) Galantini, L.; di Gregorio, M. C.; Gubitosi, M.; Travaglini, L.; Tato, J. V.; Jover, A.; Meijide, F.; Soto Tellini, V. H.; Pavel, N. V. Bile Salts and Derivatives: Rigid Unconventional Amphiphiles as Dispersants, Carriers and Superstructure Building Blocks. *Curr. Opin. Colloid Interface Sci.* **2015**, *20* (3), 170–182.
(56) Haslewood G.A.D. Bile Salt. *Steroids* **1967**, *10* (2), 186.
(57) Chen, M.; Gratzel, M.; Thomas, J. K. Kinetic Studies in Bile Acid Micelles. *J. Am.*

Chem. Soc. **1975**, *97* (8), 2052–2057.
(58) Vila Verde, A.; Frenkel, D. Kinetics of Formation of Bile Salt Micelles from Coarse-Grained Langevin Dynamics Simulations. *Soft Matter* **2016**, *12* (23), 5172–5179.
(59) Jover, A.; Meijide, F.; Rodrı, E. Aggregation Kinetics of Sodium Deoxycholate in Aqueous Solution. **1998**, *7463* (12), 4359–4363.
(60) Oakenfull, D. G.; Fisher, L. R. The Role of Hydrogen Bonding in the Formation of Bile Salt Micelles. *J. Phys. Chem.* **1977**, *81* (19), 1838–1841.
(61) Madenci, D.; Egelhaaf, S. U. Self-Assembly in Aqueous Bile Salt Solutions. *Curr. Opin. Colloid Interface Sci.* **2010**, *15* (1–2), 109–115.
(62) Fontell, K. Micellar Behaviour in Solutions of Bile-Acid Salts - IV. An X-Ray Study of the Aqueous Solutions. *Kolloid-Zeitschrift Zeitschrift f??r Polym.* **1971**, *246* (2), 710–718.
(63) Esposito G., Giglio E., Pavel N.V., Z. A. Size and Shape of Sodium Deoxycholate Mlcellar Aggregates. **1987**, No. 1, 356–362.
(64) Briganti, G.; D'Archivio, A. A.; Galantini, L.; Giglio, E. Structural Study of the Micellar Aggregates of Sodium Chenodeoxycholate and Sodium Deoxycholate. *Langmuir* **1997**, *13* (22), 5811–5815.
(65) Kawamura, H.; Murata, Y.; Yamaguchi, T.; Igimi, H.; Tanaka, M.; Sugihara, G.; Kratohvil, J. P. Spin-Label Studies of Bile Salt Micelles. *J. Phys. Chem.* **1989**, *93* (8), 3321–3326.
(66) Galantini, L.; Giglio, E.; Leonelli, A.; Pavel, N. V. An Integrated Study of Small-Angle X-Ray Scattering and Dynamic Light Scattering on Cylindrical Micelles of Sodium Glycodeoxycholate. *J. Phys. Chem. B* **2004**, *108* (9), 3078–3085.
(67) Cozzolino, S.; Galantini, L.; Giglio, E.; Hoffmann, S.; Leggio, C.; Pavel, N. V. Structure of Sodium Glycodeoxycholate Micellar Aggregates from Small-Angle X-Ray Scattering and Light-Scattering Techniques. *J. Phys. Chem. B* **2006**, *110* (25), 12351–12359.
(68) Terech, P.; De Geyer, A.; Struth, B.; Talmon, Y. Self-Assembled Monodisperse Steroid Nanotubes in Water. *Adv. Mater.* **2002**, *14* (7), 495–498.
(69) Zhang, X.; Zou, J.; Tamhane, K.; Kobzeff, F. F.; Fang, J. Self-Assembly of PH-Switchable Spiral Tubes: Supramolecular Chemical Springs. *Small* **2010**, *6* (2), 217–220.
(70) di Gregorio, M. C.; Travaglini, L.; Del Giudice, A.; Cautela, J.; Pavel, N. V.; Galantini, L. Bile Salts: Natural Surfactants and Precursors of a Broad Family of Complex Amphiphiles. *Langmuir* **2018**, acs.langmuir.8b02657.
(71) Travaglini, L.; D'Annibale, A.; Di Gregorio, M. C.; Schillén, K.; Olsson, U.; Sennato, S.; Pavel, N. V.; Galantini, L. Between Peptides and Bile Acids: Self-Assembly of Phenylalanine Substituted Cholic Acids. *J. Phys. Chem. B* **2013**, *117* (31), 9248–9257.
(72) Travaglini, L.; D'Annibale, A.; Schillén, K.; Olsson, U.; Sennato, S.; Pavel, N. V.; Galantini, L. Amino Acid-Bile Acid Based Molecules: Extremely Narrow Surfactant Nanotubes Formed by a Phenylalanine-Substituted Cholic Acid. *Chem. Commun.* **2012**, *48* (98), 12011–12013.
(73) Gubitosi, M.; D'Annibale, A.; Schillén, K.; Olsson, U.; Pavel, N. V.; Galantini, L. On the Stability of Lithocholate Derivative Supramolecular Tubules. *RSC Adv.* **2017**, *7* (1), 512–517.
(74) Noponen, V.; Valkonen, A.; Lahtinen, M.; Salo, H.; Sievänen, E. Self-Assembly Properties of Bile Acid Derivatives of l-Cysteine, l-Valine and l-Serine Alkyl Esters. *Supramol. Chem.* **2013**, *25* (3), 133–145.
(75) Noponen, V.; Toikkanen, K.; Kalenius, E.; Kuosmanen, R.; Salo, H.; Sievänen, E. Stimuli-Responsive Bile Acid-Based Metallogels Forming in Aqueous Media. *Steroids* **2015**, *97*, 54–61.
(76) Kuosmanen, R.; Puttreddy, R.; Willman, R. M.; Äijäläinen, I.; Galandáková, A.;

Ulrichová, J.; Salo, H.; Rissanen, K.; Sievänen, E. Biocompatible Hydrogelators Based on Bile Acid Ethyl Amides. *Steroids* **2016**, *108*, 7–16.
(77) Di Gregorio, M. C.; Pavel, N. V.; Miragaya, J.; Jover, A.; Meijide, F.; Vázquez Tato, J.; Soto Tellini, V. H.; Galantini, L. Catanionic Gels Based on Cholic Acid Derivatives. *Langmuir* **2013**, *29* (40), 12342–12351.
(78) Di Gregorio, M. C.; Varenik, M.; Gubitosi, M.; Travaglini, L.; Pavel, N. V.; Jover, A.; Meijide, F.; Regev, O.; Galantini, L. Multi Stimuli Response of a Single Surfactant Presenting a Rich Self-Assembly Behavior. *RSC Adv.* **2015**, *5* (47), 37800–37806.
(79) Tellini, V. H. S.; Jover, A.; Meijide, F.; Tato, J. V.; Galantini, L.; Pavel, N. V. Supramolecular Structures Generated by a P-Tert-Butylphenylamide Derivative of Cholic Acid: From Vesicles to Molecular Tubes. *Adv. Mater.* **2007**, *19* (13), 1752–1756.
(80) Manghisi, N.; Leggio, C.; Jover, A.; Meijide, F.; Pavel, N. V.; Tellini, V. H. S.; Tato, J. V.; Agostino, R. G.; Galantini, L. Catanionic Tubules with Tunable Charge. *Angew. Chemie - Int. Ed.* **2010**, *49* (37), 6604–6607.
(81) di Gregorio, M. C.; Severoni, E.; Travaglini, L.; Gubitosi, M.; Sennato, S.; Mura, F.; Redondo-Gómez, C.; Jover, A.; Pavel, N. V.; Galantini, L. Bile Acid Derivative-Based Catanionic Mixtures: Versatile Tools for Superficial Charge Modulation of Supramolecular Lamellae and Nanotubes. *Phys. Chem. Chem. Phys.* **2018**.
(82) Zhang, P.; Qian, X.; Zhang, Z.; Li, C.; Xie, C.; Wu, W.; Jiang, X. Supramolecular Amphiphilic Polymer-Based Micelles with Seven-Armed Polyoxazoline Coating for Drug Delivery. *ACS Appl. Mater. Interfaces* **2017**, *9* (7), 5768–5777.
(83) Vybornyi, M.; Vyborna, Y.; Häner, R. Silica Mineralization of DNA-Inspired 1D and 2D Supramolecular Polymers. *ChemistryOpen* **2017**, 488–491.
(84) Mokari, T.; Rothenberg, E.; Popov, I.; Costi, R.; Banin, U. Selective Growth of Metal Tips onto Semiconductor Quantum Rods and Tetrapods. *Science (80-.).* **2004**, *304* (5678), 1787–1790.
(85) Li, R.; Li, Z.; Dong, Z.; Khor, K. A Review of Transmission Electron Microscopy of Quasicrystals—How Are Atoms Arranged? *Crystals* **2016**, *6* (9), 105.
(86) Gauvin, R. Review of Transmission Electron Microscopy for the Characterization of Materials. **1997**, *10291* (Cr 69), 102910C.
(87) Microscopy, T. E. *Transmission Electron Microscopy*; 2016.
(88) Bellare, J. R.; Davis, H. T.; Scriven, L. E.; Talmon, Y. Controlled Environment Vitrification System: An Improved Sample Preparation Technique. *J. Electron Microsc. Tech.* **1988**, *10* (1), 87–111.
(89) Cheng, Z. Fluids, Colloids, Soft Materials, and an Introduction to Soft Matter Physics. **2016**, No. 1898.
(90) Berne J., B., P. R. *Dynamic Light Scattering: With Application to Chemistry, Biology, and Physics*; Dover Publications, 2000.
(91) Schätzel, K. Correlation Techniques in Dynamic Light Scattering. *Appl. Phys. B Photophysics Laser Chem.* **1987**, *42* (4), 193–213.
(92) Geisbrecht, B. V.; Hamaoka, B. Y.; Perman, B.; Zemla, A.; Leahy, D. J. The Crystal Structures of EAP Domains from Staphylococcus Aureus Reveal an Unexpected Homology to Bacterial Superantigens. *J. Biol. Chem.* **2005**, *280* (17), 17243–17250.
(93) Scheffold, F. Charactrisation of Particle Assemblies by 3D Cross Correlation Light Scattering and Diffusing Wave Spectroscopy. **2014**, *9232* (Opc), 923203.
(94) Barone, G.; Gennaro, G.; Giuliani, A. M.; Giustini, M. Interaction of Cd(II) and Ni(II) Terpyridine Complexes with Model Polynucleotides: A Multidisciplinary Approach. *RSC Adv.* **2016**, *6* (6), 4936–4945.
(95) Meijide, F.; Trillo, J. V.; De Frutos, S.; Galantini, L.; Pavel, N. V.; Soto, V. H.; Jover, A.; Vázquez Tato, J. Formation of Tubules by P-Tert-Butylphenylamide Derivatives of Chenodeoxycholic and Ursodeoxycholic Acids in Aqueous Solution. *Steroids* **2012**, *77*

(12), 1205–1211.
(96) Galantini, L.; Leggio, C.; Jover, A.; Meijide, F.; Pavel, N. V.; Soto Tellini, V. H.; Tato, J. V.; Di Leonardo, R.; Ruocco, G. Kinetics of Formation of Supramolecular Tubules of a Sodium Cholate Derivative. *Soft Matter* **2009**, *5* (16), 3018–3025.
(97) Di Gregorio, M. C.; Pavel, N. V.; Jover, A.; Meijide, F.; Vázquez Tato, J.; Soto Tellini, V. H.; Alfaro Vargas, A.; Regev, O.; Kasavi, Y.; Schillén, K.; et al. PH Sensitive Tubules of a Bile Acid Derivative: A Tubule Opening by Release of Wall Leaves. *Phys. Chem. Chem. Phys.* **2013**, *15* (20), 7560–7566.
(98) Cautela, J.; Lattanzi, V.; Månsson, L. K.; Galantini, L.; Crassous, J. J. Sphere - Tubule Superstructures through Supramolecular and Supracolloidal Assembly Pathways. *Small* **2018**, *1803215*, 1803215.
(99) Azari, A.; Crassous, J. J.; Mihut, A. M.; Bialik, E.; Schurtenberger, P.; Stenhammar, J.; Linse, P. Directed Self-Assembly of Polarizable Ellipsoids in an External Electric Field. *Langmuir* **2017**, *33* (48), 13834–13840.
(100) Petekidis, G.; Galloway, L. A.; Egelhaaf, S. U.; Cates, M. E.; Poon, W. C. K. Mixtures of Colloids and Wormlike Micelles: Phase Behavior and Kinetics. *Langmuir* **2002**, *18* (11), 4248–4257.
(101) Feenstra; Stroscio; Tersoff; Fein. Atom-Selective Imaging of the GaAs(110) Surface. *Phys. Rev. Lett.* **1987**, *58* (12), 1192–1195.
(102) Vliegenthart G.A., Lekkerkerker H., N., W. Phase Behavior of Colloidal Rod-Sphere Mixtures. *J. Chem. Phys.* **1999**, *111* (9), 4153–4157.
(103) Månsson, L. K.; Immink, J. N.; Mihut, A. M.; Schurtenberger, P.; Crassous, J. J. A New Route towards Colloidal Molecules with Externally Tunable Interaction Sites. *Faraday Discuss.* **2015**, *181*, 49–69.
(104) Rohacova, J.; Marín, M. L.; Martinez-Romero, A.; Diaz, L.; O'Connor, J. E.; Gomez-Lechon, M. J.; Donato, M. T.; Castell, J. V.; Miranda, M. A. Fluorescent Benzofurazan-Cholic Acid Conjugates for in Vitro Assessment of Bile Acid Uptake and Its Modulation by Drugs. *ChemMedChem* **2009**, *4* (3), 466–472.
(105) Májer, F.; Salomon, J. J.; Sharma, R.; Etzbach, S. V.; Najib, M. N. M.; Keaveny, R.; Long, A.; Wang, J.; Ehrhardt, C.; Gilmer, J. F. New Fluorescent Bile Acids: Synthesis, Chemical Characterization, and Disastereoselective Uptake by Caco-2 Cells of 3-Deoxy 3-NBD-Amino Deoxycholic and Ursodeoxycholic Acid. *Bioorganic Med. Chem.* **2012**, *20* (5), 1767–1768.
(106) Gomez-Mendoza, M.; Marin, M. L.; Miranda, M. A. Photoactive Bile Salts with Critical Micellar Concentration in the Micromolar Range. *Phys. Chem. Chem. Phys.* **2016**, *18* (18), 12976–12982.
(107) Schneider, S.; Schramm, U.; Schreyer, a; Buscher, H. P.; Gerok, W.; Kurz, G. Fluorescent Derivatives of Bile Salts. I. Synthesis and Properties of NBD-Amino Derivatives of Bile Salts. *J. Lipid Res.* **1991**, *32* (11), 1755–1767.
(108) Cuquerella, M. C.; Rohacova, J.; Marin, M. L.; Miranda, M. A. Stereodifferentiation in Fluorescence Quenching within Cholic Acid Aggregates. *Chem. Commun.* **2010**, *46* (27), 4965–4967.
(109) Gouin, S.; Zhu, J. X. X. Synthesis of 3α- and 3β-Dimers from Selected Bile Acids. *Steroids* **1996**, *61* (11), 664–669.
(110) Travaglini, L.; Gubitosi, M.; di Gregorio, M. C.; Pavel, N. V.; D'Annibale, A.; Giustini, M.; Soto Tellini, V. H.; Vázquez Tato, J.; Obiols-Rabasa, M.; Bayati, S.; et al. On the Self-Assembly of a Tryptophan Labeled Deoxycholic Acid. *Phys. Chem. Chem. Phys.* **2014**, *16* (36), 19492–19504.
(111) Zhuang, Y.-D.; Chiang, P.-Y.; Wang, C.-W.; Tan, K.-T. Environment-Sensitive Fluorescent Turn-On Probes Targeting Hydrophobic Ligand-Binding Domains for Selective Protein Detection. *Angew. Chemie* **2013**, *125* (31), 8282–8286.

(112) Yablonovitch, E. Inhibited Spontaneous Emission in Solid-State Physics and Electronics. *Phys. Rev. Lett.* **1987**, *58* (20), 2059–2062.
(113) John, S. Strong Localization of Photons in Certain Disordered Dielectric Superlattices. *Phys. Rev. Lett.* **1987**, *58* (23), 2486–2489.
(114) Ursell, T. Cahn-Hilliard Kinetics and Spinodal Decomposition in a Diffuse System. *October* **2007**, 1–6.
(115) Ni, R.; Belli, S.; Van Roij, R.; Dijkstra, M. Glassy Dynamics, Spinodal Fluctuations, and the Kinetic Limit of Nucleation in Suspensions of Colloidal Hard Rods. *Phys. Rev. Lett.* **2010**, *105* (8), 7–10.
(116) Paloli, D.; Mohanty, P. S.; Crassous, J. J.; Zaccarelli, E.; Schurtenberger, P. Fluid-Solid Transitions in Soft-Repulsive Colloids. *Soft Matter* **2013**, *9* (11), 3000–3004.
(117) Monovoukas, Y.; Gast, A. P. The Experimental Phase Diagram of Charged Colloidal Suspensions. *J. Colloid Interface Sci.* **1989**, *128* (2), 533–548.
(118) Sirota, E. B.; Ou-Yang, H. D.; Sinha, S. K.; Chaikin, P. M.; Axe, J. D.; Fujii, Y. Complete Phase Diagram of a Charged Colloidal System: A Synchro- Tron x-Ray Scattering Study. *Phys. Rev. Lett.* **1989**, *62* (13), 1524–1527.
(119) Gasser, U.; Fernandez-Nieves, A. Crystal Structure of Highly Concentrated, Ionic Microgel Suspensions Studied by Small-Angle x-Ray Scattering. *Phys. Rev. E - Stat. Nonlinear, Soft Matter Phys.* **2010**, *81* (5), 1–6.
(120) P`mies, J. C.; Cacciuto, A.; Frenkel, D. Phase Diagram of Hertzian Spheres. *J. Chem. Phys.* **2009**, *131* (4).
(121) Romeo, G.; Ciamarra, M. P. Elasticity of Compressed Microgel Suspensions. *Soft Matter* **2013**, *9* (22), 5401–5406.
(122) Stieger, M.; Richtering, W.; Pedersen, J. S.; Lindner, P. Small-Angle Neutron Scattering Study of Structural Changes in Temperature Sensitive Microgel Colloids. *J. Chem. Phys.* **2004**, *120* (13), 6197–6206.
(123) Plamper, F. A.; Richtering, W. Functional Microgels and Microgel Systems. *Acc. Chem. Res.* **2017**, *50* (2), 131–140.
(124) Mourran, A.; Wu, Y.; Gumerov, R. A.; Rudov, A. A.; Potemkin, I. I.; Pich, A.; Möller, M. When Colloidal Particles Become Polymer Coils. *Langmuir* **2016**, *32* (3), 723–730.
(125) Bhattacharjee, S.; Elimelech, M.; Borkovec, M. DLVO Interaction between Colloidal Particles : Beyond Derjaguin ' s Approximation. **1998**, *71* (4), 5–8.
(126) Lekkerkerker H., N., W., *Colloids and the Depletion Interaction*, Springer Netherlands, **2011.**